TECHNISCHE UNIVERSITÄT MÜNCHEN

Professur für Hydromechanik

Numerical investigation of mass transfer at non-miscible interfaces including Marangoni force

Tianshi Sun

Vollständiger Abdruck der an der Ingenieurfakultät Bau Geo Umwelt der Technischen Universität München zur Erlangung des akademischen Grades eines

Doktor-Ingenieurs

genehmigten Dissertation.

Vorsitzender:	Prof. Dr.-Ing. habil. F. Duddeck
Prüfer der Dissertation:	
	1. Prof. Dr.-Ing. M. Manhart
	2. Prof. Dr. J.G.M. Kuerten

Die Dissertation wurde am 31. 08. 2018 bei der Technischen Universität München eingereicht und durch die Ingenieurfakultät Bau Geo Umwelt am 11. 12. 2018 angenommen.

Zusammenfassung

Diese Studie untersucht den mehrphasigen Stofftransport einer nicht-wässrigen flüssigkeit ("Non-aqueous phase liquid", NAPL) im Porenmaßstab, einschließlich der Auswirkungen von Oberflächenspannungs und Marangoni-Kräften. Für die Mehrphasenströmung wurde die Methode "Conservative Level Set" (CLS) implementiert, um die Grenzfläche zu verfolgen, während die Oberflächenspannungskraft mit der Methode "Sharp Surface Tension Force" (SSF) simuliert wird. Zur Messung des Kontaktwinkels zwischen der Oberfläche der Flüssigkeit und der Kontur der Kontaktfläche wird ein auf der CLS-Methode basierendes Kontaktlinienmodell verwendet; das "Continuum Surface Force" (CSF)-Modell wird zur Modellierung des durch einen Konzentrationsgradienten induzierten Marangoni-Effekts verwendet; ein neues Stofftransfermodell, das einen Quellterm in der Konvektions-Diffusionsgleichungen verwendet, wird zur Untersuchung des Stoffübergangs verwendet.

Ein zweidimensionales Hohlraummodell, das den Marangoni-Effekt vernachlässigt, wird mit veriierendem Strömungsbedingungen (z.B. unterschiedliche Weberzahlen, Reynoldszahlen und Beschleunigungszeitskalenverhältnisse) implementiert, um die Massentransferrate und das Verhalten der Grenzfläche zu untersuchen. Aufgrund der geringen Löslichkeit der NAPL wird nur der konvektive Stoffaustausch berücksichtigt. Die Ergebnisse zeigen, dass die Weber-Zahl und das Zeitskalenverhältnis die wichtigsten Faktoren sind, die das Verhalten der Grenzfläche bzw. der Stoffübergangsrate beeinflussen.

Ein zweidimensionales Stofftransfermodell, das den Marangoni-Effekt berücksichtigt, wird qualitativ untersucht. Der Marangoni-Effekt beeinflusst das lokale Geschwindigkeitsfeld in der Nähe der Grenzfläche und erzeugt damit ein Zirkulationsmuster. Damit erhöht der Marangoni-Effekt auch die lokale Stoffübergangsrate, was in guter qualitativer Übereinstimmung mit der theoretischen Analyse und Experimenten steht.

Abstract

This study investigates pore-scale multiphase mass transport, including the effects of surface tension forces and Marangoni forces of a Non-Aqueous Phase Liquid (NAPL) into water. For the multiphase flow, the Conservative Level Set (CLS) method has been implemented to track the interface, while the surface tension force is simulated by the Sharp Surface tension Force (SSF) method. A contact line model based on the CLS method is used to measure the contact angle between the surface of the liquid and the outline of the contact surface; the Continuum Surface Force (CSF) model is applied to model the Marangoni effect induced by a concentration gradient; a new mass transfer model, adding a source term in the convection-diffusion equations, is employed to investigate the mass transfer rate.

A two-dimensional cavity model that neglects the Marangoni effect is implemented with various flow conditions (such as different Weber numbers, Reynolds numbers and acceleration time scale ratios) to examine the mass transfer rate and the behavior of the interface. Due to the low solubility of the NAPL, only the convective mass transfer will be taken into account. The results show that the Weber number and the time scale ratio are the most significant factors affecting the behavior of the interface and mass transfer rate, respectively.

A two-dimensional mass transfer model, influenced by the Marangoni effect, is qualitatively investigated. As a circulation pattern appears close to the interface, the Marangoni effect begins to impact the local velocity field near the interface. Furthermore, the Marangoni effect also promotes the local mass transfer rate, which is in good agreement with the theoretical analysis and previous simulations.

Acknowledgements

I would like to express my deepest gratitude to my supervisor Prof. Dr.-Ing. habil. Michael Manhart, for his constant encouragement, support and guidance. I have greatly benefited from his broad knowledge and instruction.

I gratefully thank Prof. Dr. J.G.M. Kuerten, not only for being my project mentor, but also for being my dissertation reviewer. Additionally, I thank you for giving me the opportunity to work in TU/e for three-month to experience the different academic atmosphere.

I thank my project team leader Dr.-Ing. Daniel Quosdorf. I am also grateful to my colleague Dr.-Ing. Alexander McCluskey for proofreading a draft of this dissertation. I thank all my colleagues at the Chair of Hydromechanics.

I thank the International Graduate School of Science and Engineering (IGSSE) at Technische Universität München, which funded my project 9.03, Mass transfer at interfaces to non-aqueous phases (Marangoni). I also thank Carina Wismeth and PD Dr. Thomas Baumann for the interesting discussions.

Finally, I would especially like to thank my parents and family for their continuous support and encouragement.

Contents

List of Tables

List of Figures

Nomenclature

Abbreviations

Ca	Capillary number
CFD	Computational Fluid Dynamics
CFL	Counrant Friedrich Lewy
CLS	Conservative Level Set method
CLSVOF	Coupled Level Set and Volume Of Fluid
CSF	Continuous Surface Force
DNS	Direct Numerical Simulation
FVM	Finite Volume Method
GFM	Ghost Fluid Method
ILU	Incomplete Lower-Upper decomposition
La	Laplace number
LES	Large Eddy Simulation
Ma	Marangoni number
NAPL	Non-Aqueous Phase Liquids
PDE	Partial Differential Equation
Re	Reynolds number
Ri	Richardson number
RK	Runge-Kutta method
RMS	Root Mean Square
Sc	Schmidt number
Sh	Sherwood number
SSF	Sharp Surface tension Force method
VOF	Volume Of Fluid
We	Weber number

Greek Letters

α	Parameter	[/s]
α_1	Parameter	[/m]

α_2	Parameter	[/s]
δ	Delta function	[−]
ϵ	Artificial diffusion number	[−]
γ_{LG}	Liquid-vapor interfacial energy	[N/m]
γ_{SG}	Solid-vapor interfacial energy	[N/m]
γ_{SL}	Solid-liquid interfacial energy	[N/m]
γ	Constant	[−]
κ	Surface curvature	[−]
λ	Wavelength	[m]
μ	Dynamic viscosity of fluid	[Ns/m^2]
μ_1	Dynamic viscosity of fluid 1	[Ns/m^2]
μ_2	Dynamic viscosity of fluid 2	[Ns/m^2]
ν	Kinematic Viscosity of fluid	[m^2/s]
ν_1	Kinematic Viscosity of fluid 1	[m^2/s]
ν_2	Kinematic Viscosity of fluid 2	[m^2/s]
ω_0	Inviscid oscillation frequency	[s]
Φ	Potential	[N/m]
ϕ	Distance function	[−]
ρ	Density of fluid	[kg/m^3]
ρ_1	Density of fluid 1	[kg/m^3]
ρ_2	Density of fluid 2	[kg/m^3]
σ	Surface tension	[N/m]
τ	Time scale ratio	[−]
τ_0	Time scale	[s]
τ_p	Dimensionless time step	[−]
τ_{LS}	Pseudo time step	[s]
θ_C	Contact angle	[−]
θ_D	Macroscopic dynamic contact angle	[−]
θ_s	Static contact angle	[−]
φ	Level set function	[−]

Mathematical Operators

$\cdot$	Scalar multiplication
Δ	Difference

$\langle\rangle$	Jump condition	
∇	Gradient	
∂	Partial differential	

Roman Letters

$\mathbf{F_d}$	Driving force	[N]
$\mathbf{F_{su}}$	Surface tension force	[N]
$\mathbf{g}$	Gravity	[m/s^2]
$\mathbf{n}$	Normal vector	[$-$]
$\mathbf{t}$	Tangential vector	[$-$]
$\dot{m}$	Mass flow rate	[N]
A_0	Initial wave amplitude	[m]
C	Color function	[$-$]
c	Concentration	[$kmol$/m^3]
c_G	Concentration of the gas	[$kmol$/m^3]
c_L	Concentration of the liquid	[$kmol$/m^3]
D	Diffusion coefficient	[m^2/s]
d	Constant	[$-$]
D_d	Diameter of a drop	[m]
D_G	Diffusion coefficient of the gas	[m^2/s]
D_L	Diffusion coefficient of the liquid	[m^2/s]
F_i	Body force	[N]
f_{LG}	Error function	[$kmol$]
h	Grid space	[m]
H_D	Distribution coefficient	[$-$]
K	Convective mass transfer coefficient	[m/s]
k_{od}	Mass transfer coefficient	[m/s]
L	Characteristic length	[m]
p	Pressure	[N/m^2]
r	Radius	[m]
S	Surface area	[m^2]
s	Time	[s]
T	Temperature	[K]
u, v, w	Velocity vector components in $x-$, $y-$ and $z-$ direction	[m/s]

V	Volume	$[\mathrm{m}^3]$
x, y, z	Coordinates	$[\mathrm{m}]$
Y	Mass fraction	$[-]$

1 Introduction

1.1 Background

Transport on pore-scale is significant in many environmental applications. Mass transfer rates across the interface in porous media impact natural systems, especially underground water. Due to the pore topology, diffusion and transverse dispersion dominates the dissolution process of non-aqueous phase liquids (NAPL) (Eberhardt & Grathwohl, 2002). The mass transfer process of contaminants from NAPL pools into groundwater involves the properties of the fluid and the interface in between, transport in the water phase and the diffusion transport in the non-aqueous phase (Wehrer *et al.*, 2011). Therefore, the diffusion is often the main constraint for the mass transfer rate. Additionally, mass transfer with the least kinetics controls the overall release rate (Ortiz *et al.*, 1999). This behavior is taken into account in numerical models of mass transport and rely on the interface stability.

However, when a gradient of surface tension exists along the interface between two phases, mass transport can be impacted by the Marangoni effect (Levich & Krylov, 1969). In this case, diffusion is not sufficient to precisely predict the mass transfer rate. Moreover, the surface tension gradient can be caused by the variance of the concentration field and temperature field along the interface. The application of the Marangoni effect are apparent in various fields. The Marangoni effect can influence crystal growth, enhance oil recovery (Khosravi *et al.* (2014) and Cheng *et al.* (2012)), control flow in micro-fluidic devices (Darhuber & Troian, 2005) and promote mixing. However, little attention has been paid to the Marangoni effect in the field of contaminant transport in undergroundwater.

1.2 Motivation

NAPLs such as gasoline and various petroleum products, for instance octanol, may enter the subsurface from a leaking underground pipe (Fetter, 1993). Due to their low solubility in water, it may take several decades for them to disperse by nature dissolution. Residual NAPLs will be trapped in soil and constitute a long-term threat to drinking water supplies. For this reason, a variety of techniques have been developed to remediate the NAPLs contaminated land.

The most widely used method is pump-and-treat, which extracts the contaminated groundwater from the subsurface by pumping. Then, the contaminated groundwater is treated before it can be discharged (Mackay & Cherry, 1989). However, this system takes a very long period to meet the cleanup requirements; the 'rebound ' phenomenon (i.e. pumping reduces the ground water level, leaving residuals on the soil. After the groundwater returns to normal, the contaminants on the soil dissolve) may also arise. The other treatment is In-situ remediation, which injects chemical or biological materials to subsurfaces in order to enhance the solubility of the contaminant (Pennell *et al.* (1993), Augustijn *et al.* (1994)) or increase the liquidity of the trapped NAPL (Brandes & Farley, 1993). This method is limited by the inability to meet the purifying requirements.

There is no perfect method thus far due to the complexity of mass transfers. It is necessary to fundamentally understand the properties and the influencing factors of mass transfer to solve the current contaminate problem. We can assume that the local mass transfer rates across the interface are influenced by the Marangoni effect, since the Marangoni convection impacts the mixing in the aqueous phase at low Peclet numbers.

In a combined experimental and numerical study, our objective is to concentrate on the Marangoni effect of the mass transfer. We conduct a series of numerical simulations to test the contributions of individual physical effects, such as the Gibbs-Marangoni effect. Additionally, we investigate the purging of non-aqueous phase liquids from a two-dimensional cavity model. In this application, different flow conditions are employed to test the influences on the mass transfer rate and the behavior of the interface.

1.3 Outline

The structure of this work is:

Chapter 2 presents the basic conceptions and equations of the incompressible flow and mass transportation. This is followed by the introductions of theory and characteristics of multiphase flows, surface tension force, the contact angle model and mass transfer model. Moreover, the numerical measurements of the above models are described.

Chapter 3 contains the code basis and state of the present work at the beginning. First, the code MGLET which is used to simulate the turbulent flows using the Finite Volume Method (FVM) and the staggered grid is introduced in section (3.1). Then, the conservative level set method that was implemented in MGLET (Andre, 2012) is presented in section (3.2). This method is employed to track the interface due to its good mass conservation and simplicity. In this section, at first the reinitialization equation used to maintain conservation is presented; afterwards, the Fast Marching Method (FMM), applied to compute the normal vector using a distance function, is analysed; then, the method to calculate the interface curvature using the normal vector is presented; finally, the surface tension force is simulated using the Sharp Surface tension Force (SSF) method at the end of this chapter.

Current implementations are presented in chapter 4. In section (4.1), a contact line model for the conservative level set method is described. The Marangoni effect, induced by the concentration gradient, is implemented using the Continuum Surface Force (CSF) model in section (4.2). The mass transfer model across the interface in multiphase flows is described in section (4.3). Finally, in section (4.4), the time step size limited by different effects is examined.

Four test cases are presented in chapter 5 to validate different numerical models: the first test case is applied to test the accuracy of the surface tension force; the second one is applied to validate the interaction between the viscous force and surface tension force; the third one validates the contact line model based on the CLS method; and the fourth one is implemented to validate the mass transfer model.

In chapter 6, we present the results of the mass transfer from a two-dimensional cavity model. Section (6.1) introduces the cavity model. The numerical configuration of the cavity model is shown in section (6.2). Afterwards, the two-dimensional and three-dimensional results are compared in section (6.3) to investigate whether additional effects exist. The behavior of the interface, influenced by various Weber numbers, is examined in section (6.4). The results of the mass transfer rate, influenced by different flow conditions (e.g., the Weber number, the Reynolds number and time scale ratio), are presented in section (6.5).

In chapter 7, the results of the mass transfer rate impacted by the Marangoni effect are presented. The objective and the numerical model are introduced in section (7.1) and section (7.2), respectively. Section (7.3) examines the velocity field influenced by the different parameters. The mass transfer rate, influenced by the Marangoni effect, is presented in section (7.4).

The conclusions and outlook for future study are provided in chapter 8.

2 Theory

In this chapter, we introduce the theoretical foundation and numerical models of the present work. Single-phase flows are described by the governing equations: the three-dimensional Navier-Stokes equations in section (2.1). Afterwards, in section (2.2) the numerical methods which are used to track the interfaces for multiphase flows are discussed. Next, some additional effects due to the multiphase flows, such as the surface tension force, the contact line model and the Marangoni effect, are presented in section (2.3), (2.4) and (2.5). Finally, we conclude with the description of the numerical model of mass transfer.

2.1 Single-phase flows

We solve the Navier-Stokes equations for incompressible flows of a Newtonian fluid with external forces. The equations of the conservation laws of mass and momentum are indicated by

$$\frac{\partial u_i}{\partial x_i} = 0, \tag{2.1}$$

$$\frac{\partial u_i}{\partial t} + u_j \frac{\partial u_i}{\partial x_j} = -\frac{1}{\rho}\frac{\partial p}{\partial x_i} + \frac{\partial}{\partial x_j}\left[\nu\left(\frac{\partial u_i}{\partial x_j} + \frac{\partial u_j}{\partial x_i}\right)\right] + F_i, \tag{2.2}$$

where u_i refers to the instantaneous velocities, ρ indicates the density, p is the pressure, ν denotes the kinematic viscosity, and F_i represents the body forces, including the gravitational force, surface tension force and Marangoni force (see section (4.2)).

The convection-diffusion equation is used to solve the scalar transportation,

$$\frac{\partial \Phi}{\partial t} + u_i \frac{\partial \Phi}{\partial x_i} = D\frac{\partial^2 \Phi}{\partial x_i^2}, \tag{2.3}$$

where Φ is the scalar field (i.e. level set, temperature) and D is the diffusivity.

2.2 Multiphase flows

In some special cases when liquid and gas occur simultaneously, a two-phase flow model can solve them. The relatively simple relationships between variables of a single-phase flow model cannot satisfy the analysis of two-phase flows or multiphase flows. By definition, a multiphase flow is an interactive flow of two or more different phases with common interfaces. Each of the phases is regarded as having a separately defined volume fraction (or mass fraction) and has its own properties, temperature, and velocity.

Multiphase flows can be divided into two categories:

- Materials with different states or phases (e.g. water-steam mixture and a liquid-solid system).
- Materials with different chemical properties but in the same state or phase (i.e. liquid-liquid systems, such as oil droplets in water).

Multiphase flows in industry have a large variety of applications. For example, in aerospace and marine engineering, some research are related to atomization and free surface flow. In the chemical and process industries, the design of separation systems and mixers requires multiphase flow analyses. In power engineering, the multiphase flow models need to be employed to interpret certain phenomena, e.g. cavitation and combustion.

2.2.1 Characteristics of multiphase flows

All multiphase flow problems have features which differ from those existing in single-phase flows.

- Multiphase flows contain a variety of immiscible phases, each with a set of flow variables, even if the two-phase flow can be divided into gas-liquid, gas-solid, liquid-liquid, and liquid-solid. Therefore, more parameters describe the multiphase flow than those for the single-phase flow.
- The behavior of the interface is an important factor affecting the multiphase flow, which also poses a challenge for research. For example, when cavitation occurs in the pump, as the fluid moves from the low pressure zone to the high pressure zone, the shape of the interface between the cavitation bubble and the environmental liquid may change. Furthermore, there are many forms of instability in multiphase flows.
- The spatial distribution of the various phases in the flow field strongly influences flow behavior.
- When the densities of different phases vary greatly, the effect of gravity on the multiphase flow is significantly more important than the single-phase flow.

Regardless of the experimental studies or the numerical simulations, the treatment of multiphase flow problems is much more complicated than the single-phase flow, and even contains some issues that cannot be solved using current state of the art.

2.2.2 Numerical methods of multiphase flows

The numerical simulation of multiphase flows is a vast and complicated topic. Current experimental methods are insufficient for visualizing phenomena appearing on scales of space and time. In such cases, numerical simulations for fluid-fluid and gas-fluid systems may be a useful tool to validate or explain the concept of the physicist, engineer, or mathematician.

There have been several methods to simulate the interface of multiphase flows numerically, including the volume of fluid (VOF) (Hirt & Nichols (1981), Tryggvason *et al.* (2011) and Rider & Kothe (1998)), level set method (Sussman *et al.* (1994), Sethian (1999) and Osher & Fedkiw (2002)), and front tracking method (Unverdi & Tryggvason (1992*b*) and (Popinet & Zaleski, 1999)).

The VOF method is a surface-tracking technique implemented into a Eulerian coordinate system, where Navier-Stokes equations which indicate the motion of the flow have to be solved separately. In this manner, the interface is represented implicitly by a volume fraction or color function C which is discontinuous and varies between the constant value 1 in full cells to 0 in empty cells, while the intermediate value of C in the transition region defines the location of the interface. The interface reconstruction has to be carried out in each cell using a stair-stepped (Hirt & Nichols, 1981), piecewise linear (Rider & Kothe, 1998) or other approaches at each advection step. The VOF method is known to maintain good mass conservation properties and to allow for topology changes, such as those occurring during reconnection or breakup, which are implicit in the algorithm. Moreover, it is straightforward to extend to three-dimensional space and simple to implement. However, since the geometric information of the interface is not stored directly, the interface reconstruction and the surface tension forces have to be taken good care of to ensure that simulations are physically accurate. Also, due to the discontinuity of the color function, the higher order methods cannot be applied, resulting in inaccurate results (Olsson & Kreiss, 2005).

The level set method is a numerical technique used for tracking interfaces and modeling shapes. In this method, the interface is defined as an iso-contour of a smooth scalar function. The advantage of the level set method is that the evolving curves and surfaces can be numerically calculated on a fixed Cartesian grid (Osher & Sethian, 1988). It is not necessary to parameterize these objects. Another advantage of the level set method is that it is convenient to track the topological changes of an object, such as when the shape of the object is divided into two. All of these make the level set method a powerful tool for modeling. However, some problems can arise when using this technique to simulate multiphase flows. As the function is advected by the flow field, it may lose smoothness (Sussman *et al.*, 1994). In terms of mass conservation, many deficiencies also exist. Several attempts have been made to improve mass conservation by adding a reinitialization constraint (Sussman *et al.* (1998), Sussman & Fatemi (1999), Olsson & Kreiss (2005) and Olsson *et al.* (2007)).

In the method of Sussman *et al.* (1998) and Sussman & Fatemi (1999), a distance function is defined as the level set function to track the interface. The distance function is determined by solving a particular form of the Hamilton-Jacobi partial differential equation known as the Eikonal equation. In this case, after reinitialization, the level set function becomes the distance function without changing its zero level set, where the interface is located.

Olsson & Kreiss (2005) and Olsson *et al.* (2007) use an alternative smeared out Heaviside function as the level set function, i.e. a function being zero in one fluid and one in the other. The value varies smoothly from zero to one over the interface. The advection of the level set function is performed using a conservative scheme with a reinitialization step that maintains the thickness of the interface. The reinitialization step is achieved by solving a reinitialization equation, which contains both advection and diffusion terms that can be discretized conservatively using the finite volume method (FVM). These two terms can prevent the transition region from smearing out and maintain the smoothness of the interface, respectively. Furthermore, as opposed to the discontinuous color function, the smoothness of the level set function makes our method easy to extend to a higher order (Olsson & Kreiss, 2005).

2.3 Surface tension

Physically, the definition of surface tension, in the narrow sense, refers to the tendency of liquids to attempt to obtain the minimum surface potential energy; broadly speaking, all the tension at the interface between two different phases is called surface tension. The dimension of surface tension is force per unit length or energy per unit area.

The most common example of surface tension occurs at the interface between a liquid and some other media. For example, the surface tension of water comes from the cohesion caused by van der Waals forces. When solids, such as water striders, run on the water, the surface tension will be as flat as possible to maintain the water surface in order to achieve the least surface potential energy. If the water strider remains its weight limits, there will be only a few hollows on the surface, which is why water striders can move on water.

2.3.1 Physics

Surface tension can be defined in terms of force or energy:

In terms of force, the cohesive forces among liquid molecules are responsible for the phenomenon of surface tension. Inside the liquid, each molecule is pulled in every direction equally by neighboring molecules, so that the net force of the molecules inside the liquid is zero. However, the liquid molecules on the surface between the liquid and a gas are unbalanced, causing the molecules in the surface layer to be pulled inwards. Therefore, the liquid will have a tendency to reduce the surface area, and this behavior is surface tension phenomenon.

In terms of energy, the interior molecules have as many neighbors as possible, so they are at a lower state of potential energy. However, the molecules in the surface layer have higher potential energy. In order for the low energy part to achieve a stable state, the molecules in the surface layer tend to move toward the interior of the liquid, resulting in a decrease in the

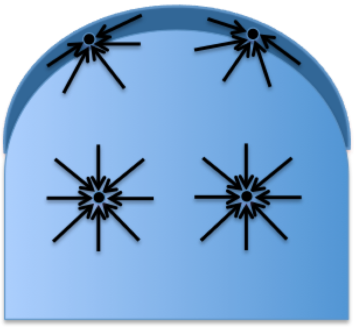

Figure 2.1: Diagram of the forces on molecules of a liquid

number of molecules in the surface layer and a reduction in the liquid surface area (White, 1948).

2.3.2 Numerical modeling

The interface is defined by two different phases, and the treatment of discontinuities must be taken into account for density, viscosity and pressure fields. Thus, a special strategy is needed to numerically describe the jump conditions. Two different methods can be used to achieve this: the continuous surface force (CSF) model (Brackbill *et al.*, 1992) and the ghost fluid method (GFM) (Fedkiw *et al.*, 1999), which is a continuous interface fashion and a sharp interface fashion, respectively. The CSF method is widely used to model the surface tension force of two-phase flows in the VOF method (Gueyffier *et al.* (1999), Gao *et al.* (2003) and Tang *et al.* (2004)), the level set method (Chang *et al.* (1996) and Wang *et al.* (2008)) and the diffuse-interface method (Badalassi *et al.* (2003) and Kim (2005)). In the CSF model, the surface tension is converted into a type of body force rather than as a boundary condition, and the resulting force is proportional to the product of the interface gradient and the interface curvature. Interface curvature can be calculated using standard finite differences on the level set function which varies smoothly around the interface. Modeling surface tension can lead to the occurrence of parasitic currents. Discretizing the pressure and surface tension forces with the same stencil is used to significantly reduce parasitic currents (Renardy & Renardy (2002) and Tryggvason *et al.* (2011)). However, two essential problems still exist. Smoothing the Heaviside function introduces an interface thickness, which depends on the mesh size, and thus an uncertainty regarding the exact location of the interface (Mammoli & Brebbia, 2005).

The GFM extended to incompressible two-phase flows by Kang *et al.* (2000), avoids the interface thickness and, in contrast to the CSF method, respects jump discontinuous across the interface. It is necessary to know the location of the interface, as well as its curvature, so the ghost cells can be defined on both sides of the interface. Then, the jump conditions can be extrapolated on the ghost nodes on each side of the interface. Following the jump conditions, the discontinued functions are extended continuously, and then derivatives are estimated (Mammoli & Brebbia, 2005). In this way, the discretization of discontinuous vari-

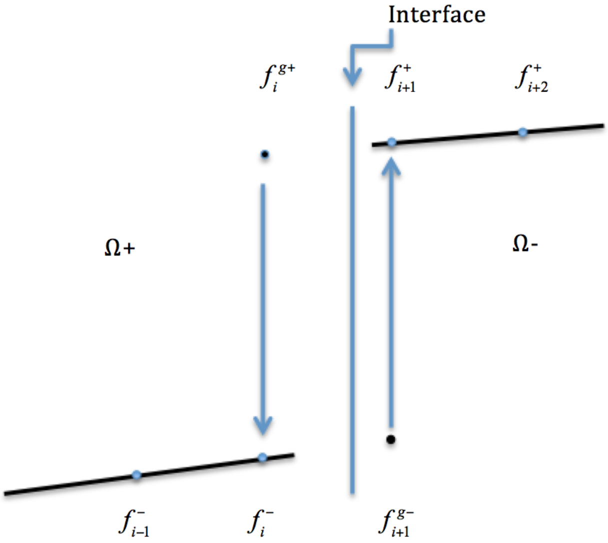

Figure 2.2: Numerical scheme of GFM

ables is more accurate, and the velocity field has much smaller spurious currents than when using the CSF method.

2.4 Contact angle models

The contact angle θ is the angle between the surface of the liquid and the outline of the contact surface, when an interface exists between a liquid and a solid. This angle measures the wettability of a solid surface by a liquid. The contact angle is not limited to the liquid-gas interface; it is also available for liquid-liquid or vapor-vapor interfaces. For a given system, at a given temperature and pressure, the contact angle is uniform. However, the contact angle hysteresis exists in practice.

2.4.1 Mechanisms

The contact angle at steady state can be calculated using the Young equation, playing a role of a boundary condition.

$$\frac{\gamma_{SG} - \gamma_{SL}}{\gamma_{LG}} = \cos\theta_C, \tag{2.4}$$

where θ_C is the contact angle, γ_{SG} indicates the solid-vapor interfacial energy, γ_{SL} denotes the solid-liquid interfacial energy, and γ_{LG} refers to the liquid-vapor interfacial energy (i.e. the surface tension).

The prerequisite of the Young equation is that the surface is perfectly flat. Even with such a smooth surface, hysteresis in the contact angle still exists. In this case, the contact angle ranges from the so-called advancing (maximal) contact angle θ_{max} to the receding (minimal) contact angle θ_{min}. The contact angle hysteresis is defined as $\theta_{max} - \theta_{min}$. The equilibrium contact angle is within these two values and can be calculated from them ((Tadmor, 2004), (Chibowski & Terpilowski, 2008)):

$$\theta_C = \arccos\left(\frac{r_A \cos\theta_{max} + r_B \cos\theta_{min}}{r_A + r_B}\right), \tag{2.5}$$

where

$$r_A = \left(\frac{\sin^3\theta_{max}}{2 - 3\cos\theta_{max} + \cos^3\theta_{max}}\right)^{1/3} \tag{2.6}$$

and

$$r_B = \left(\frac{\sin^3\theta_{min}}{2 - 3\cos\theta_{min} + \cos^3\theta_{min}}\right)^{1/3}. \tag{2.7}$$

The real solid surface is either rough or has a non-uniform chemical composition, which makes the contact angle not as unique as the Young equation predicts. The roughness has a substantial effect on the contact angle and the wettability of a surface. If the surface is wetted homogeneously, the droplet is in the Wenzel state (Wenzel (1936)), while if the surface is wetted heterogeneously, the droplet is in the Cassie-Baxter state (Cassie & Baxter (1944)). The contact angles computed using both the Wenzel and Cassie-Baxter equations have been found to agree well with contact angles with real surfaces (Marmur (2009)). In our work, the surfaces in all the simulations are assumed to be sufficiently smooth.

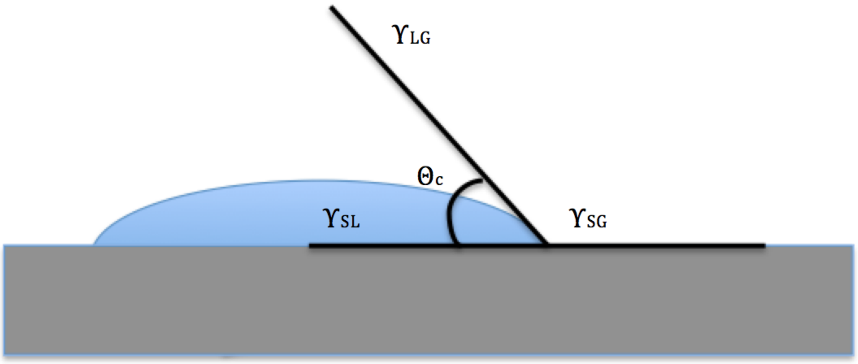

Figure 2.3: Schematic of a liquid drop showing the quantities in the Young equation.

2.4.2 Numerical models for the contact angle

Zahedi *et al.* (2009) developed an algorithm for CLS method. However, this method is only available for two-dimensional computation. Furthermore, it also requires two additional numerical parameters, which are obtained by numerical experiments and test-case dependent. Sato & Ničeno (2012) developed a new method suitable for both two- and three-dimensional computations. Their method modifies the reinitialization step from the original CLS, without adding parameters. The layer of cells adjacent to the wall is referred as to the wall layer and treated separately from other layers. In this layer, the level set function is only sharpened in the tangential direction of the wall. Meanwhile, the conservation is satisfied. This model has been implemented in MGLET in present work, as discussed in detail in section (4.1).

Many studies have been carried out on the contact line model in the context of some other conservative methods, such as VOF and CLSVOF. Bussmann *et al.* (1999) and Bussmann *et al.* (2000) first calculated the drop impact phenomena using a three-dimensional VOF code. Meanwhile, in Afkhami & Bussmann (2009), a height function was used in the VOF method to simulate the contact line model. This method enables the contact line phenomena to be simulated in both static and dynamic conditions. A contact line model for CLSVOF, developed by Sussman (2001) and Sussman (2005), incorporates an embedded boundary approach (Colella *et al.*, 1999) in which a solid-body shape can be displayed within a Cartesian grid. With the help of the contact line model, contact line dynamics problems can be resolved: for instance, free surface flow around a solid body (Yang & Stern, 2009), free surface deformation due to a wall adhesion force without gravity (Himeno & Watanabe, 2005), and drop impact phenomena (Yokoi, 2011).

2.5 Marangoni effect

The Marangoni effect occurs when a surface tension gradient exists along the interface between two phases. In most cases, this two-phase interface is a liquid-gas interface. As the solute concentration, surfactant concentration, and temperature change along the interface, a surface tension gradient is usually generated.

2.5.1 Relevance

The applications of the Marangoni effect have been observed in various fields. This effect has to be considered during the welding process, since it influences the stresses within the material as well as deformation. Forces that generated from the Marangoni effect can also affect crystal growth, leading to defects within the structure, which can inhibit the material's semiconducting capabilities. During the electron beam melting process, the Marangoni effect can be caused in the melting process by large thermal gradients. These forces have a negative impact on the quality of the material.

There are various ways to define a Marangoni number, a dimensionless number quantifying the influence of the Marangoni effect. One possibility is:

$$Ma = -\frac{L\Delta\sigma}{\mu D}, \tag{2.8}$$

where L is the characteristic length, μ is the dynamic viscosity and σ is the surface tension.

2.5.2 Mechanisms

When two liquids are in contact with each other, the liquid with stronger surface tension pulls more strongly on the surrounding liquid than one with lower surface tension, so that the liquid flows away from regions of low surface tension.

Tears of wine is a typical phenomenon caused by Marangoni effect. Its mechanism is visualized in figure (2.4). It forms at the three-phase junction of glass walls, wine, and air. At this junction, the fluid remains on the surface of the glass. Since the vapor pressure of alcohol is higher than that of water, the alcohol in the wine continues to evaporate from the surface, evaporating faster than water. The alcohol concentration in the thin film drops quickly, because of their small volume and relatively large surface area. This establishes a concentration difference between the thin film and the flat contact surface, between the wine and the air, which in turn causes a surface tension gradient that moves the thin film up the wall of the glass.

As alcohol is further volatilized, a greater surface tension gradient is created. More wine is drawn to the glass wall until droplets form. At this point gravity will pull the tears of wine along the glass wall back to the main body of the wine.

There are two special cases of the Marangoni effect: (1) In the case where the change in surface tension is driven by concentration, the Marangoni effect is referred to as the solutocapillary effect:

$$d\sigma = \frac{\partial\sigma}{\partial c}dc, \tag{2.9}$$

where c is the concentration. (2) In the case where the surface tension varies due to the temperature, the Marangoni effect is referred to as the thermo-capillary effect (Levich & Krylov, 1969):

$$d\sigma = \frac{\partial\sigma}{\partial T}dT, \tag{2.10}$$

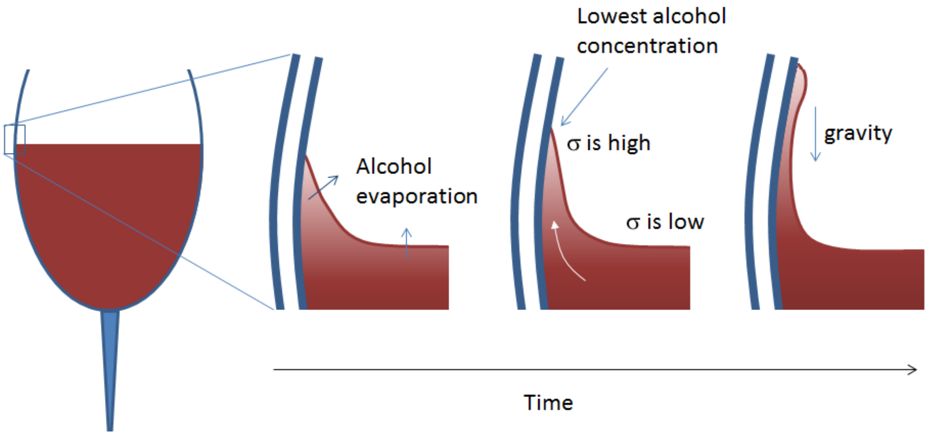

Figure 2.4: The phenomenon of tears of wine (Source: COMSOL INC.).

where T is the temperature. Both (1) and (2) can take place simultaneously, such that,

$$d\sigma = \frac{\partial \sigma}{\partial T} dT + \frac{\partial \sigma}{\partial c} dc. \tag{2.11}$$

2.5.3 Numerical models

Numerical simulation of the Marangoni convection can be performed in several ways. The critical point of these numerical methods is to specify the location of the interface. The methods for tracking the interface for two-phase flows are discussed in section (2.2). The Marangoni convection together with mass transfer and heat transfer has been studied extensively with different CFD models. Many numerical simulations of the Marangoni effect have been documented.

As the Marangoni force is the tangential component of surface tension force, the numerical treatment of the Marangoni effect is similar to the surface tension effect. Two approaches can be used to deal with the Marangoni effect: one is the continuum surface tension method and the other is the ghost fluid method (see section (2.3)). Based on the continuum surface fluid method, the Marangoni force is transformed to a volume force in the region near the interface in the momentum equations, rather than as boundary conditions. The CSF method is directly applicable to the level set method (Sussman *et al.*, 1994) and reported to be quite robust. However, as mentioned above, the CSF method generates spurious currents near the interface when surface tension force are dominant. These spurious currents are caused by the inaccuracy in curvature estimations and the imbalance of the surface tension and pressure gradient forces (Francois *et al.*, 2006).

The ghost fluid method is used to deal with the jump conditions of physical quantities. In GFM, with the properly defined ghost cells, the boundary conditions are implemented in the form of discontinuity in the solution variable, in the gradient of the variable and in the properties of two-fluid across the interface (Shaikha *et al.*, 2015). As a result, the sharp interface is maintained without smearing. The discontinuous variables are discretized more accurately in GFM, thus the spurious currents are much lower as compared to the CSF method. However, the GFM is not a conservative method because it solves two single fluid problems rather than the two-phase problem. Therefore, the numerical flux is calculated twice at the interface (Liu *et al.*, 2011).

The Marangoni effect is widely used in many fields. Davis (1987) examined the instabilities leading to the Marangoni effect. The impact of the Marangoni effect on crystal growth was considered by Okano *et al.* (1991), Kobayashi *et al.* (1997), Galazka & Wilke (2000), and Kawaji *et al.* (2003). The thermo-capillary effect of a droplet in a non-uniform temperature field was studied in Bassano (2003). The impacts of the Marangoni convection on binary mixture, in which the surface tension depends on both the temperature and the solute concentration was investigated in a series of papers ((Bergeron *et al.*, 1994), (Bergeron *et al.*, 1998) and (Bahloul *et al.*, 2003)). The Marangoni convection can be also used in absorption processes (Kim *et al.*, 2004). The numerical simulation of the Marangoni effect induced by interphase mass transfer to/from drops, especially for mass transfer to/from a deformable drop were conducted in Mao & Chen (2004) and Wang *et al.* (2008).

2.6 Mass transfer over interfaces

Mass transfer describes the passing of mass from one point to another and is the central issue in transport phenomena. In multi-physics systems, mass transfer can take place in a single phase as well as over phase boundaries. Although mass transfer also exists between solid-phase materials, in most engineering problems mass transfer involves at least one fluid phase (gas or liquid).

In many cases, mass transfer of a substance occurs in conjunction with chemical reactions. This means that the flux of a chemical substance within a volume element does not have to be conserved, because the chemical substances can be generated and consumed in this volume element. The chemical reaction is the source or sink of this flux balance.

The mass transfer theory allows for the computation of the mass flux, and the temporal and spatial distribution of different substances in a system (including in the presence of chemical reactions). The purpose of such calculations is to understand, design or control such systems. Explaining the mechanisms of mass transfer is essential, not only for the design of mass transfer equipment, but also for reactor design, especially if it relates to reactions that are controlled by mass transfer. In addition, mass transfer plays an important role in environmental engineering, space technology, and biomedical engineering.

Mass transfer results from the effect of the chemical potential caused by concentration, temperature and pressure gradients. The driving force F_d can be written as:

$$\mathbf{F_d} = -\nabla\Phi, \tag{2.12}$$

where Φ is the potential in the system.

The dimensionless number which is used to measure the ratio of the convective mass transfer to the rate of diffusive mass transport is given by the Sherwood number (Sh):

$$Sh = \frac{K}{D/L}, \tag{2.13}$$

where L is the characteristic length, K is the convective mass transfer coefficient and D is the mass diffusivity. Once the Sherwood number is calculated, then the mass transfer coefficient can be obtained. Furthermore, the Sherwood number can also be defined as a function of the Reynolds number (Re) and the Schmidt number (Sc):

$$Sh = f(Re, Sc). \tag{2.14}$$

Depending on different model configurations and different flow conditions, the relationship between the Sherwood number, the Reynolds number and the Schmidt number is various. The Reynolds number is the ratio of inertial forces to viscous forces in the fluid:

$$Re = \frac{\rho u L}{\mu} = \frac{uL}{\nu}, \tag{2.15}$$

where μ is the dynamic viscosity of the fluid.

The Schmidt number is a dimensionless number defined as the ratio of momentum diffusivity (kinematic viscosity) and mass diffusivity:

$$Sc = \frac{\nu}{D} = \frac{\mu}{\rho D}. \tag{2.16}$$

The primary challenge of mass transfer is to determine the concentration distribution and mass transfer rate. Many studies have been discussed on the mass transfer rate under different numerical and experimental conditions.

2.6.1 Mass transfer due to the temperature gradient (phase change)

Evaporation is a common form of mass transfer caused by temperature gradients. From the microscopic perspective, evaporation is the process of liquid molecules leaving the liquid surface. Molecules in a liquid move constantly and irregularly, with their average kinetic energy dependent on the temperature of the liquid. Due to the random movement and collision of molecules there are always some molecules that have higher kinetic energy than the average instantaneous kinetic energy. Molecules with sufficient kinetic energy to overcome the forces between the molecules of the liquid, such as those near the surface of the liquid, will 'escape' and enter the surrounding air in gaseous phase.

As the molecules with higher kinetic energy escape from the liquid, the energy removed from the vaporized liquid reduces the average kinetic energy and the temperature of the liquid, resulting in evaporative cooling.

For different flow conditions and different model configurations, the mass transfer rate can be defined in various ways, as discussed below:

Mass transfer by evaporation at a flat interface

If we consider a liquid at a given temperature T_L, and the constant partial vapor pressure (lower than the saturated pressure p_{sat}) at a certain distance H from the interface (see figure (2.5)), we are able to calculate the mass transfer rate of the evaporation at steady state (Borghi & Anselmet, 2014):

$$\dot{m} = \frac{\rho D_v}{H} ln \left(\frac{1 - Y_{V,H}}{1 - Y_{Vsat}(T_L)} \right), \tag{2.17}$$

where $\dot{m}$ is the mass transfer rate, D_v is the diffusion coefficient of the vapor in the air, $Y_{V,H}$ is the mass fraction of vapor at H, Y_{Vsat} is the mass fraction of the vapor at interface. H should be sufficiently small to ensure that the pressure between the point H and the interface linearly and monotonously depends on the distance H.

The evaporation process contains three phenomena (Borghi & Anselmet, 2014): Firstly, the movement of vapor molecules in the gas phase due to the gradient of the partial pressure, which is molecular diffusion. Secondly, the transformation of the liquid-vapor at the surface maintains the equilibrium between the liquid and the vapor, which is influenced by the behavior of the molecular diffusion. Thirdly, the motion of the interface, in which the liquid moves towards the interface and the vapor moves away from the interface.

If the gas mixture is a perfect mixture, then

$$p_V = p \frac{M_{mix}}{M_V} Y_V, \tag{2.18}$$

where p_V is the partial pressure, p is the total pressure in the gas and can be assumed to be known, M_{mix} is the molar mass of the mixture and M_V is the molar mass of the vapor.

Stefan's equation expresses the relationship between the partial pressure and the mass frac-

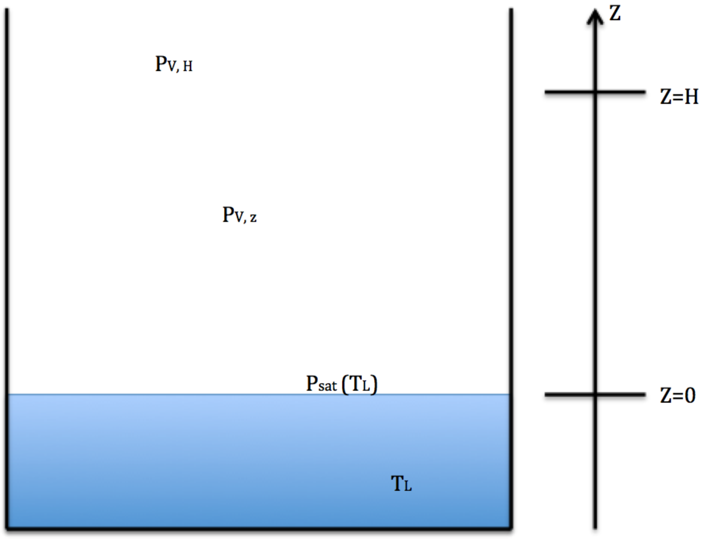

Figure 2.5: Model for the study of the evaporation of a liquid

tion:

$$\dot{m} = \frac{\rho D_v}{H} ln \left(\frac{p - p_{V,H}}{p - p_{sat}(T_L)} \right). \tag{2.19}$$

If we assume that the total pressure is higher than $p_{V,H}$ and p_{sat}, and the temperatures of the liquid and the gas are lower than $30°C$, we have: $\frac{P-P_{V0}}{P-Psat} \approx 1$. In this case, Stefan's equation simplifies to Dalton's equation:

$$\dot{m} = \frac{\rho D_v}{H} ln \left(p_{sat}(T_L) - p_{V,H} \right). \tag{2.20}$$

Although Dalton's and Stefan's equations are only applicable to simple one-dimensional problems of water evaporation in a tube (Borghi & Anselmet, 2014), they clearly show how the mass transfer rate depends on water temperature, and that the evaporation rate increases when the partial vapor pressure in H is low. We can also observe that the equation is reversible: if the partial vapor pressure of H is higher than the saturation pressure at the temperature of the liquid, then there is condensation rather than vaporization at the interface. Therefore, this equation is not only related to the evaporation, but also an equilibrium of vaporization-condensation.

Evaporation of a drop

Another case of the local evaporation rate is the vaporization of a drop in a gas phase. This case has been studied both theoretically and experimentally (Sirignano, 1999).

The drop is assumed to be isolated and spherical in shape without gravity, so that the profiles of the velocity and temperature fields remain spherical. Then the mass flow rate of the vaporization from the drop can be obtained similarly to the case of the flat interface:

$$\dot{m} = 4\pi r_d \rho_g D_v ln \left(\frac{1 - Y_{V\infty}}{1 - Y_{Vsat}(T_s)} \right), \tag{2.21}$$

where r_g is the radius of the drop, ρ_g is the density of the gas, $D_v = const.$ is the mass diffusivity of the vapor. T_s is the temperature at the surface. Then the mass flow rate per surface unit is:

$$\dot{m} = \frac{\rho_g D_v}{r_d} ln \left(\frac{1 - Y_{V\infty}}{1 - Y_{Vsat}(T_s)} \right). \tag{2.22}$$

In recent years, new methods have been developed to compute phase change, with the help of interface tracking techniques, which have been discussed in section (2.2). Juric & Tryggvason (1998) showed a front tracking approach to simulate the boiling flow. In this case, the single field formulation is applied to describe the entire flow field. Welch & Wilson (2000) introduced a volume of fluid method for phase change. A coupled level set and volume of fluid method was used in Tomar *et al.* (2005) to calculate the film boiling. In Tanguy *et al.* (2007) a combination of the level set method and the ghost fluid method was implemented to handle the two-dimensional vaporizing issues.

2.6.2 Mass transfer due to the concentration gradient

Mass transfer driven by the concentration gradient without considering the temperature field is discussed in this section. It is widely used in chemical engineering, especially liquid-liquid reactions and solvent extraction. Many of these industrial processes are related to the mass transfer of moving drops or bubbles (rising or falling). The main challenge in the numerical simulation of mass transfer to/from a buoyancy driven drop is that the motion of a deformed drop with simultaneous mass transfer must be solved with the un-determined topology of a surface (Petera & Weatherley, 2001). Key to this challenge is understanding the mass transfer mechanism by considering the drop deformation and the mass transfer process itself. Due to the complexity of the mass transfer, many empirical and theoretical equations for mass transfer coefficients for various drop and bubble conditions can be looked up (Clift *et al.*, 1978).

In addition to experiments, a number of numerical simulations have been performed recently. Mao *et al.* (2001) concentrated grid points near the bubble by using a body-fitted coordinate system. Davidson & Rudman (2002) and Gupta *et al.* (2010) simulated mass transfer with a volume of fluid method. Unverdi & Tryggvason (1992*a*) and Aboulhasanzadeh *et al.* (2012) computed the bubble motion with mass transfer using the front tracking method. The latter approach applies a multi-scale computation technique to significantly reduce the overall grid resolutions. Wang *et al.* (2008), Ganguli & Kenig (2011a), Ganguli & Kenig (2011b) and Hayashi & Tomiyama (2011) implemented the level set method tracking the interface to measure the mass transfer rate and, to observe the behavior of bubbles. Especially for Ganguli & Kenig (2011a) and Ganguli & Kenig (2011b), the conservative version of the level set method was applied by adding two source terms in the momentum equations. However, in most of these studies, the volume of the bubbles was assumed to remain constant. Only Hayashi & Tomiyama (2011) considered the shrinkage of the bubbles as gas diffused to the liquid.

The overall liquid mass transfer coefficient k_{od} influenced by the concentration gradient can be estimated by

$$V\frac{\partial c_L}{\partial t} = Sk_{od}\left(c_L - \frac{c_G}{H_D}\right), \tag{2.23}$$

where k_{od} is the mass transfer coefficient, V is the volume of the liquid, S is the surface area of the liquid, H_D is the dimensionless distribution coefficient, c_L and c_G are the concentrations in the liquid phase and gas phase, respectively. c_G/H_D means the concentration in equilibrium in the liquid phase due to the Henry's law. The Henry's law and H_D will be discussed in detail in section (4.3).

If the time interval is sufficiently small, integrating equation (2.23) gives:

$$k_{od} = -\frac{V}{S}\frac{1}{t_2 - t_1} ln\left(\frac{c_G/H_D - \bar{c}_{L,t1}}{c_G/H_D - \bar{c}_{L,t2}}\right), \tag{2.24}$$

where t_1 and t_2 are the two measurement times and $\bar{c}_L$ is the average concentration of the drop at any time.

The difference between the mass transfer coefficient k_{od} and the mass flux $\dot{m}$ is a factor ρ (i.e., $k_{od} = \dot{m}/\rho$). Here, the concentration term is taken into account, rather than the mass fraction term or the pressure term in the formula of evaporation rate.

Additionally, two interfacial boundary conditions need to be considered in this case:

- flux continuity at the interface

- interfacial dissolution equilibrium

The method used to implement these two interfacial boundary conditions will be discussed in section (4.3).

3 Code basis and state at the beginning

In this chapter, the code MGLET is introduced in detail, which is used to solve the governing equations of turbulent flows. Furthermore, the conservative version of the level set method (CLS), already implemented into MGLET as part of a master's thesis (Andre, 2012) will be discussed.

3.1 MGLET

The main objective of MGLET is to predict turbulent flows in and along complex geometries with Direct Numerical Simulation (DNS) and Large Eddy Simulation (LES). This code is based on the finite volume method in the Cartesian coordinate system. It has been parallelized and tested on a high-performance computer (more than 10^9 grid cells). Recently, several research groups (e.g., NTNU Trondheim, DLR Institute of atmosphere physics) have been adopting this code to various applications, such as bluff body flow and wake vortices.

Recent developments to this code include:

- Conservative Immersed Boundary method for arbitrary geometries in a Cartesian grid.
- Zonal grid refinement and hierarchical grids for high Schmidt number scalar fields.
- Particle dynamics and fiber suspension.
- Fourth-order Finite Volume schemes.
- Multiphase flows.

MGLET is implemented on a Cartesian grid with the staggered variable arrangement of computations (Manhart & Friedrich (2002), Manhart (2004)). Convective and diffusive fluxes at cell faces are discretized with central space approximations (second and fourth order). Time integration is achieved by a third-order Runge-Kutta (RK) method. The pressure in the Poisson equation is solved by an Incomplete Lower-Upper (ILU) decomposition of second order accuracy.

3.1.1 Finite volume method

The finite volume method is a numerical algorithm to solve partial differential equations (PDE) which is widely used in computational fluid dynamics (CFD). This method is based on conservation of the integral form rather than the differential form. In the finite volume method, volume integrals in a partial differential equation can be handled by calculating the values of variables averaged across the volume in conservation form. If volume integrals contain a divergence term, they can be converted to surface integrals using the divergence theorem (Gauss theorem). These terms may then be treated as fluxes at the surfaces of each control volume.

The advantages of finite volume method are:

- Consistent with the law of conservation (Because the flux entering a given volume is identical to that leaving the adjacent volume).
- Highly adaptable to the unstructured meshes.

3.1.2 Staggered grid

For a staggered grid, scalar variables (i.e. pressure, density, viscous, level set, etc.) are stored at the center of each control volume cell, and the velocities are allocated at the center of the surface of each cell. This is in contrast to a collocated grid arrangement, in which all the variables are stored in the same positions in the center of the control volume for each cell.

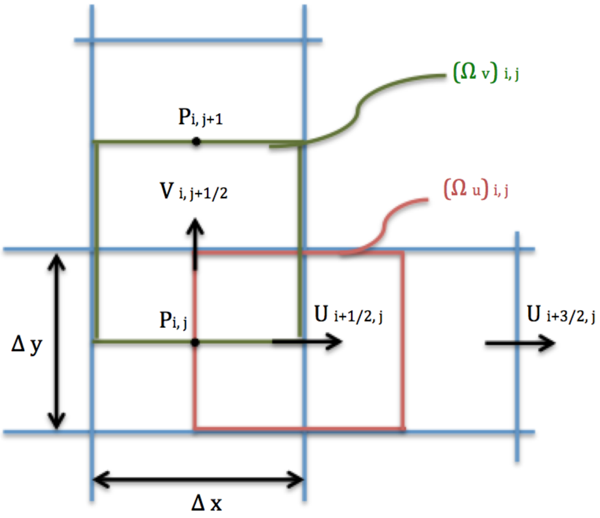

Figure 3.1: Control volumes for the spatial discretization of the momentum equations

Figure (3.1) shows the variable arrangements for a staggered grid. The main advantage of the staggered grid over the collocated grid is that the staggered grid can avoid odd-even decoupling between the pressure and velocity fields. Odd-even decoupling, which occurs in the collocated grid can lead to checkerboard patterns in the pressure field in numerical simulation. However, these kind of arrangements make it difficult to deal with different control volumes for different variables. As a result, extra care should be made when taking into account different variables in the post-processing phase.

3.2 Conservative level set method

The CLS method has been chosen as the numerical method to track the interface, due to its ability to conserve mass and simplicity. It was first implemented in the MGLET within a master thesis (Andre, 2012). The CLS method has been reprogrammed from its initial form to comply with recent updates to MGLET. To validate the implementation, some test cases were computed (see Chapter 5). In the following, the current implementation will be detailed.

3.2.1 Level set advection

The level set φ is advected by equation (3.1):

$$\frac{\partial \varphi}{\partial t} + \mathbf{u} \cdot \nabla \varphi = 0. \tag{3.1}$$

For a divergence free velocity field, this can be re-written as

$$\frac{\partial \varphi}{\partial t} + \nabla \cdot (\varphi \mathbf{u}) = 0. \tag{3.2}$$

Equation (3.2) has a number of benefits: It is effective in keeping the scalar φ conservative, ensuring that volumes of each fluid approach constant values as the level set function converges to a step function. The advection equation is discretized using the finite volume method.

In MGLET, a preprocessing step is implemented to improve resolution properties of low order numerical schemes (Schwertfirm *et al.*, 2008). This method is employed to calculate the level set function to improve the accuracy during the advection step.

3.2.2 Level set reinitialization

In order to deal with the inconsistency with the mass conservation of the level set method, Olsson & Kreiss (2005) introduced an alternative reinitialization equation which was further refined by Olsson *et al.* (2007). The reinitialization equation is given by

$$\frac{\partial \varphi}{\partial \tau} + \nabla \cdot (\varphi(1-\varphi)\mathbf{n}) = \epsilon \nabla \cdot ((\nabla \varphi \cdot \mathbf{n})\mathbf{n}), \tag{3.3}$$

where τ is the pseudo time step, ϵ is the artificial diffusion number and $\mathbf{n}$ is the interface normal vector.

To comprehend the reinitialization equation, each term in equation (3.3) has been examined separately. The second term on the left side of equation (3.3) is referred to as the compression term which is used to sharpen the definition of the interface profile. The term on the right side is referred to as the diffusion term, which is used to prevent the interface from being too sharp, maintaining the smoothness of the interface.

The steady state solution of equation (3.3) discussed by Olsson *et al.* (2007) is given by:

$$\varphi = \frac{1}{2}\left(tanh\left(\frac{\phi}{2\epsilon}\right)\right). \tag{3.4}$$

Increasing ϵ tends to smear out the interface profile while decreasing ϵ tends to sharpen the interface profile. Olsson & Kreiss (2005) suggested to define the artificial diffusion term ϵ and the pseudo time step size τ as follows:

$$\epsilon = \frac{h^{1-d}}{2} \tag{3.5}$$

and

$$\Delta\tau = \frac{h^{1+d}}{2}, \tag{3.6}$$

where is $d = 0.1$, and h is the grid spacing. In this case, as opposed to others, it is not only sufficient to obtain convergence, but also maintain a sharp interface.

In Olsson & Kreiss (2005), the level set function is advected with a total variation diminishing (TVD) method. The equation used to calculate the interface normal vector is:

$$\mathbf{n} = \frac{\nabla\varphi}{|\nabla\varphi|}. \tag{3.7}$$

The non-TVD advection schemes cannot avoid all oscillations occurring in the level set field. These oscillations lead to rapid fluctuation of the normal vector $\mathbf{n}$ near the interface. Desjardins *et al.* (2008) used a distance function ϕ free of oscillations to compute the normal vector $\mathbf{n}$,

$$\mathbf{n} = \frac{\nabla\phi}{|\nabla\phi|} \tag{3.8}$$

is to make the level set method more robust.

The distance function in the CLS is in fact the level set function in the original level set method, while the level set function in the CLS is defined using a hyperbolic tangent profile rather than the signed distance function in the original version of the level set method. The method used to determine the distance function is discussed in section (3.2.3).

When solving the Navier-Stokes equations, density and viscosity fields need to be clarified. While these two fields are assumed to be constant within each fluid, jump conditions around the interface lead to density and viscosity not being constant. The density and viscosity fields are defined using the level set function as followed (Olsson & Kreiss, 2005):

$$\rho = \rho_1 + (\rho_1 - \rho_2)\varphi \tag{3.9}$$

and

$$\mu = \mu_1 + (\mu_1 - \mu_2)\varphi. \tag{3.10}$$

3.2.3 Distance function and normal vector

The Fast Marching Method (FMM) used to compute the distance function is a numerical algorithm for solving boundary value problems of the Eikonal equation (Sethian, 1999):

$$|\nabla\phi| = 1 \quad \text{for} \quad \phi \in \Omega \tag{3.11a}$$

$$\phi = 0 \quad \text{for} \quad \phi \in \partial\Omega. \tag{3.11b}$$

The general principle of equation (3.11) is to find a path with the shortest travel time from a point in the modeling domain to the boundary. In other words, the direction of the steepest descent needs to be specified.

Using the multi-dimensional approximation from Osher & Sethian (1988), the discrete form of equation (3.11) is given by

$$\begin{aligned} |\nabla\phi|^2 \approx\ & max(D^{-x}\phi_{i,j,k}, 0)^2 + min(D^{+x}\phi_{i,j,k}, 0)^2 \\ & + max(D^{-y}\phi_{i,j,k}, 0)^2 + min(D^{+y}\phi_{i,j,k}, 0)^2 \\ & + max(D^{-z}\phi_{i,j,k}, 0)^2 + min(D^{+z}\phi_{i,j,k}, 0)^2 \\ =\ & 1. \end{aligned} \tag{3.12}$$

The version of the first order forward and backward operators, take x-direction as an example, can be defined as,

$$D^{+x}\phi_{i,j,k} = \frac{\phi_{i+1,j,k} - \phi_{i,j,k}}{\Delta x} \tag{3.13}$$

and

$$D^{-x}\phi_{i,j,k} = \frac{\phi_{i,j,k} - \phi_{i-1,j,k}}{\Delta x}. \tag{3.14}$$

However, the first order version is not sufficient to obtain the accurate values. Therefore, a second order discretization of the above equations is employed, in the x-direction:

$$D^{+x}\phi_{i,j,k} = \frac{\phi_{i+1,j,k} - \phi_{i,j,k}}{\Delta x} + S^{+}\frac{\Delta x}{2}\frac{\phi_{i+2,j,k} - 2\phi_{i+1,j,k} + \phi_{i,j,k}}{\Delta x^2} \tag{3.15}$$

and

$$D^{-x}\phi_{i,j,k} = \frac{\phi_{i,j,k} - \phi_{i-1,j,k}}{\Delta x} + S^{-}\frac{\Delta x}{2}\frac{\phi_{i,j,k} - 2\phi_{i-1,j,k} + \phi_{i-2,j,k}}{\Delta x^2}. \tag{3.16}$$

The operators of S^+ and S^- are defined as followed,

$$S^{+x}(\phi_{i,j,k}) = \begin{cases} 1 & \text{if } \phi_{i+1,j,k} \text{ and } \phi_{i+2,j,k} \text{ are known, and } \phi_{i+2,j,k} \leq \phi_{i+1,j,k} \\ 0 & \text{else} \end{cases}$$

for the forward derivative in the x-direction, and

$$S^{-x}(\phi_{i,j,k}) = \begin{cases} 1 & \text{if } \phi_{i-1,j,k} \text{ and } \phi_{i-2,j,k} \text{ are known, and } \phi_{i-2,j,k} \leq \phi_{i-1,j,k} \\ 0 & \text{else} \end{cases}$$

for the backward derivative in the x-direction. Equations for y-direction and z-direction follow similarly.

A more practical formulation is noted by Sethian (1999):

$$\begin{aligned} |\nabla\phi|^2 \approx\, & max(D^{-x}\phi_{i,j,k}, -D^{+x}\phi_{i,j,k}, 0)^2 \\ & + max(D^{-y}\phi_{i,j,k}, -D^{+y}\phi_{i,j,k}, 0)^2 \\ & + max(D^{-z}\phi_{i,j,k}, -D^{+z}\phi_{i,j,k}, 0)^2 \\ = 1. & \end{aligned} \tag{3.17}$$

With this approach, the distance function ϕ is approximately second order accurate. Since they are calculated from the gradient of ϕ (see equation (3.8)), the normal vectors are expected to be first order accurate.

In the level set method, the distance function has a positive sign on the side of the interface with $\varphi \geq 0$, while on the opposite side the distance function has a negative sign. In order to initialize the distance values around the interface, the inverse to equation (3.4) is applied, as given by

$$\phi = \epsilon ln \left(\frac{\varphi}{1-\varphi} \right). \tag{3.18}$$

The points in the domain can be categorized into three groups: known, trial and unknown. All the nodes are marked as unknown at first. Then the grid points closest to the interface are initialized by equation (3.18). These grid points are identified as having known solution values. The neighbors of the known nodes without known values are marked as trials. The remaining grid points are marked as unknown. The calculation of the gradient of a node is achieved only if the node has known neighbors. The resulting minimum distance is stored as a trial value. If at a later time a previously unknown neighbor becomes known, this minimum needs to be recalculated and compared to the previous minimum distance. Repeating this process, until the minimum distance of a given point is determined. Thereafter, this point can be marked as known, and used to compute the distance for its trial neighbors. Finally, the results can be determined until a specified distance value becomes known or all nodes are marked as known in the domain.

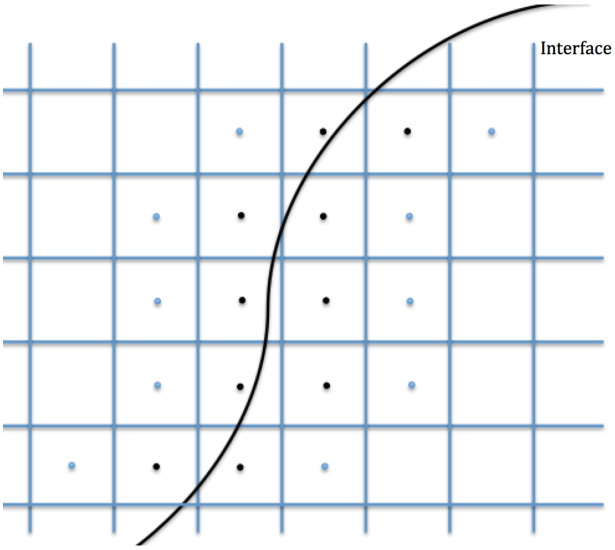

Figure 3.2: FMM initialization. Cells are marked as known (black circle), trial (blue circle) or unknown (empty).

3.2.4 Interface curvature

The accuracy of curvature is a critical factor that effects the accuracy of surface tension force calculations. The interface curvature can be calculated with a finite difference method (Sethian, 1999), a least squares method (Marchandise *et al.*, 2007) and a convolution method. Due to the second order accuracy of the distance function, the curvature calculated using finite difference method did not result in convergence (Desjardins *et al.*, 2008). For the convolution method, which has been already used to calculate the derivative of the color function in VOF (Cummins *et al.*, 2005), the curvature can be determined by computing the divergence of the normal vectors:

$$\kappa = -\nabla \cdot \mathbf{n}, \tag{3.19}$$

where κ is the curvature.

The advantage of this approach is that the additional computational cost of equation (3.19) is small. However, the disadvantage is that the curvature stencil size is larger, which may result in lower accuracy.

3.2.5 Surface tension

The surface tension force is included in the momentum equations (2.2) as a volumetric force (Brackbill *et al.*, 1992):

$$\mathbf{F}_{su} = \kappa\sigma\mathbf{n}\delta(x - x_s), \tag{3.20}$$

where σ is the constant surface tension coefficient, x_s is the point on the interface and δ is a delta function defined as:

$$\delta(x) = \begin{cases} +\infty & \text{if } x = 0 \\ 0 & \text{if } x \neq 0 \end{cases}$$

and

$$\int_{-\infty}^{+\infty} \delta(x) = 1.$$

The role of the delta function is to transform the surface tension force from a volume integral to a surface integral over the domain of the interface. In the CSF method, $\mathbf{n}\delta(x - x_s)$ can be replaced with the gradient of the level set function $\nabla\varphi$ (Olsson & Kreiss, 2005):

$$\mathbf{F}_{su}^{CSF} = \kappa\sigma\nabla\varphi. \tag{3.21}$$

The surface tension force is not zero if the gradient of the level set function $\nabla\varphi$ is not zero. However, as mentioned in section (2.3), the interface curvature calculated by CSF model may lead to less accurate results. An alternative method, similar to the sharp surface tension force (SSF) method (Brackbill *et al.*, 1992) is used to compute the surface tension force:

$$\mathbf{F}_{su}^{SSF} = \kappa\sigma\frac{1}{\Delta x}, \tag{3.22}$$

which is still treated as the volume integral, rather than the surface integral in the momentum equations. It also results in a jump condition in the Poisson equation similar to the GFM (Liu *et al.*, 2000). In this case, the surface tension force only exists at interfaces at which the distance function ϕ changes sign. For example, if the interface is located between the cell (i,j) and $(i+1,j)$, the surface tension force applied in x-direction can be defined as:

$$\mathbf{F}_{i+1/2,j,k} = sign(\phi_{i+1,j,k} - \phi_{i,j,k})\frac{\sigma\kappa}{\Delta x}, \tag{3.23}$$

and, in the y-direction,

$$\mathbf{F}_{i,j+1/2,k} = sign(\phi_{i,j+1,k} - \phi_{i,j,k})\frac{\sigma\kappa}{\Delta x}. \tag{3.24}$$

The curvature at the interface can be calculated from values at neighboring cells, through an interpolation process, using the distance function

$$\kappa = \frac{|\phi_{i+1,j,k}|\kappa_{i,j,k} + |\phi_{i,j,k}|\kappa_{i+1,j,k}}{|\phi_{i+1,j,k}| + |\phi_{i,j,k}|}. \tag{3.25}$$

The advantage of this method is that the points used to calculate the curvature of the interface are close to the interface, while the CSF method spreads the surface tension over the entire transition region of the level set function.

4 Current implementations

In the framework of this dissertation, models for the contact angle, the Marangoni force and mass transfer over a fluid-fluid interface have been implemented in MGLET. In section (4.1), a new contact line model for the conservative level set method is described. Then, the Marangoni model is implemented in MGLET by adding a volume force in the momentum equations shown in section (4.2). Section (4.3) introduces the mass transfer model due to the concentration gradient. Finally, in section (4.4) the time step restrictions for advancing the flow variables are presented.

4.1 A contact line treatment for the CLS method

A contact line model for the CLS method is discussed in this part. As mentioned above, many studies of the contact line model are based on the volume of fluid and sharp level set method. However, not many studies are related to the conservative level set method. Recently, only two models have focused on the CLS, Zahedi *et al.* (2009) and Sato & Ničeno (2012). In Zahedi *et al.* (2009), two additional parameters which are test-case dependent are introduced to be implemented in the reinitialization step. However, this method is limited to two-dimensional cases. Sato & Ničeno (2012) modify the reinitialization step from the original CLS, and this method enables the model to solve both two- and three-dimensional problems. In present study, the latter one is implemented.

In section (4.1.1), the revised reinitialization step based on the original CLS is described. Then the boundary conditions for the contact line model of Sato & Ničeno (2012) are introduced in section (4.1.2). This model is validated in section (5.3).

4.1.1 The reinitialization function for CLS

The reinitialization function proposed by Olsson *et al.* (2007) has been introduced in section 3.2. Therein, equation (3.3) the diffusion term on the right side is limited to the normal direction only. This avoids diffusion in tangential direction. Since the flux in the direction tangential to the interface will not be balanced by any compression effects, the tangential diffusion might move the interface which is suppressed by the reinitialization function, equation (3.3). However, in the new contact line model, the tangential diffusion effects of the level set function in the reinitialization step are also significant for the movement of the interface at the wall layer; thus, the original reinitialization function is needed (Olsson &

Kreiss, 2005):

$$\frac{\partial \varphi}{\partial \tau} + \nabla \cdot (\varphi(1-\varphi)\mathbf{n}) = \epsilon \nabla \cdot (\nabla \varphi). \tag{4.1}$$

The discretized form of the reinitialization function, using the finite volume method, is written as (Sato & Ničeno, 2012):

$$V\frac{\partial \varphi}{\partial \tau} + \sum((\varphi(1-\varphi)\mathbf{n}) \cdot \mathbf{S}) = \sum \epsilon(\nabla \varphi) \cdot \mathbf{S}, \tag{4.2}$$

where V is the volume of the cell, and $\mathbf{S}$ is the area vector of the cell faces. In our study, the level set function and the normal vectors are stored at the cell centers.

4.1.2 Boundary conditions

In the following sections, we will introduce how to deal with the boundary conditions with respect to the level set function and the normal vector.

Level set function

Since the velocity at the wall surface is zero (no-slip boundary condition is applied), the fluxes of the level set function at the wall surface should also be zero. Therefore, a special treatment is needed in which the fluxes of the compression term and the diffusion term in the normal direction of the wall are forced to be zero at a wall layer. These boundary conditions are written as:

$$(\varphi(1-\varphi)\mathbf{n}) \cdot \mathbf{S}_{wall} = 0 \tag{4.3}$$

and

$$(\nabla \varphi) \cdot \mathbf{S}_{wall} = 0, \tag{4.4}$$

respectively, where $\mathbf{S}_{wall}$ is the area vector of the wall.

The layer of cells adjacent to the wall is treated differently from the other layers. Therefore, this layer is denoted as the wall layer as shown in figure (4.1). In this wall layer, fluxes of the level set function are only in the tangential direction of the wall (i.e., no fluxes in the normal direction of the wall), rather than in all directions in other layers. Therefore, the governing equation of the reinitialization equation of the wall-layer can be re-written as:

$$V\frac{\partial\varphi}{\partial\tau}+\sum((\varphi(1-\varphi)\mathbf{n})_{||}\cdot\mathbf{S})=\sum((\epsilon(\nabla\varphi)_{||})\cdot\mathbf{S}), \tag{4.5}$$

where the subscript || means the tangential component. For example, the tangential component of the vector $\mathbf{a}$ is defined as:

$$(\mathbf{a})_{||}=\mathbf{a}-(\mathbf{a}\cdot\mathbf{n}_{wall})\mathbf{n}_{wall}=0, \tag{4.6}$$

where $\mathbf{n}_w$ is the normal vector of the wall.

Thus, the fluxes of the diffusion term and the compression term in equation (4.5) on the wall boundary are written as:

$$(\varphi(1-\varphi)(\mathbf{n})_{||})\cdot\mathbf{S}_{wall}=0 \tag{4.7}$$

and

$$(\epsilon(\nabla\varphi)_{||})\cdot\mathbf{S}_{wall}=0, \tag{4.8}$$

respectively.

Since $((\mathbf{n})_{||})\cdot\mathbf{S}_{wall}=(\nabla\varphi)_{||}\cdot\mathbf{S}_{wall}=0$, these two equations also fulfill the wall boundary conditions given in equation (4.3) and equation (4.4).

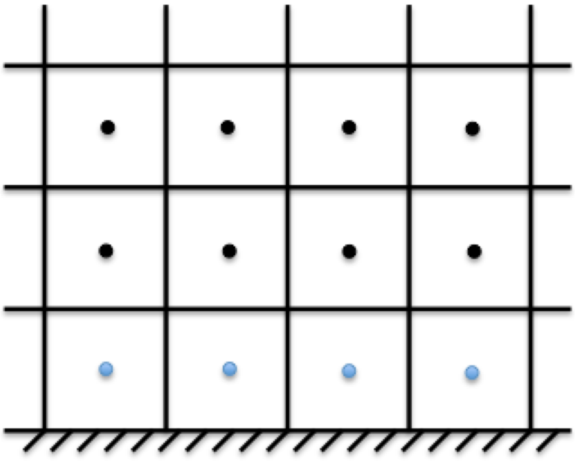

Figure 4.1: Schematic of the wall-layer (blue cells: wall-layer cells; black cells: others)

Due to equation (4.3) and equation (4.4), the fluxes of the diffusion term and the compression term shown in figure (4.2) are set to zero for a Cartesian grid system. The interface sharpening algorithm does not work between the wall-layer and other parts in the domain, since the fluxes between them are forced to be zero. Therefore, the level set function of the wall-layer smears out in the normal direction of the wall. However, the smearing out only happens in the wall layer (i.e., only one cell layer).

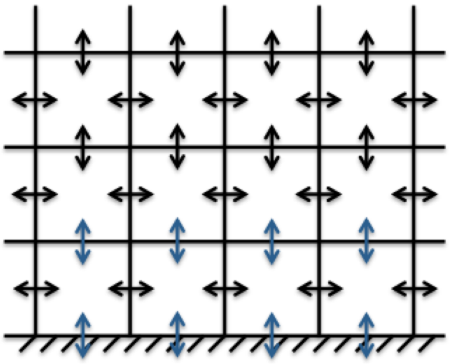

Figure 4.2: Wall-boundary treatment of the flux calculation (blue arrows: flux enforced to be zero; black arrows: flux calculated normally).

Normal vector

Since the staggered grid is implemented in MGLET, the normal vectors are stored in the center of the cells shown in figure (4.3). For a known static contact angle which is physically located on the wall boundary as a boundary condition, the normal vector $\mathbf{n}_c$ of this point is available. Then a ghost normal vector outside of the domain needs to be taken into account as follows:

$$\mathbf{n}_{i,j-1} = 2\mathbf{n}_c - \mathbf{n}_{i,j}. \tag{4.9}$$

As a result, the normal vector on the wall is fixed by its two neighbors which are located on two sides of the wall. Moreover, $\mathbf{n}_c$ can be dynamically predicted by Cox's law (see section (5.3)).

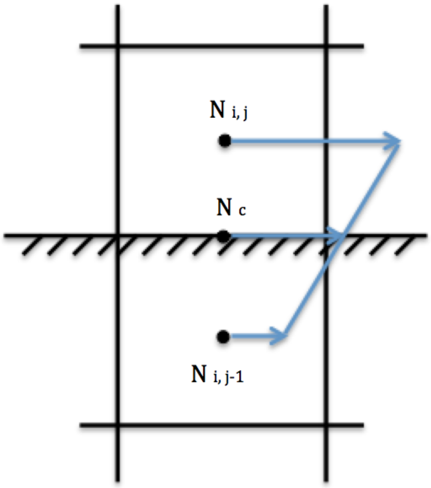

Figure 4.3: Treatment of normal vectors at boundary.

4.2 Marangoni effect

The Marangoni effect induced by the spatial variations in the surface tension coefficient can be caused by temperature or concentration gradients, or a combination of both effects. Understanding these phenomena is significant since they are related to various applications. Numerical methods for studying the Marangoni effect were discussed in section (2.2). The conservative level set method is efficient and robust for tracking the interface. And due to its continuous characteristics, the CSF method which interprets surface tension as a continuous effect across an interface, rather than as a boundary condition on the interface, is implemented to simulate the surface tension force in a direction tangential to the interface.

Stress boundary conditions are generated due to the presence of the interface, see figure (4.4). The stress boundary condition in the normal direction at the interface defines the stress jump (Landau & Lifshitz, 1987):

$$\langle \mathbf{n} \cdot \mathbf{T} \cdot \mathbf{n} \rangle = \sigma(\mathbf{x})\kappa, \tag{4.10}$$

where $\langle\rangle$ defines the jump condition across the interface (i.e., the difference on both sides of the interface) and $\mathbf{T}$ is the total stress tensor,

$$\mathbf{T} = p\mathbf{I} + \mu(\nabla \mathbf{u} + \nabla \mathbf{u}^T). \tag{4.11}$$

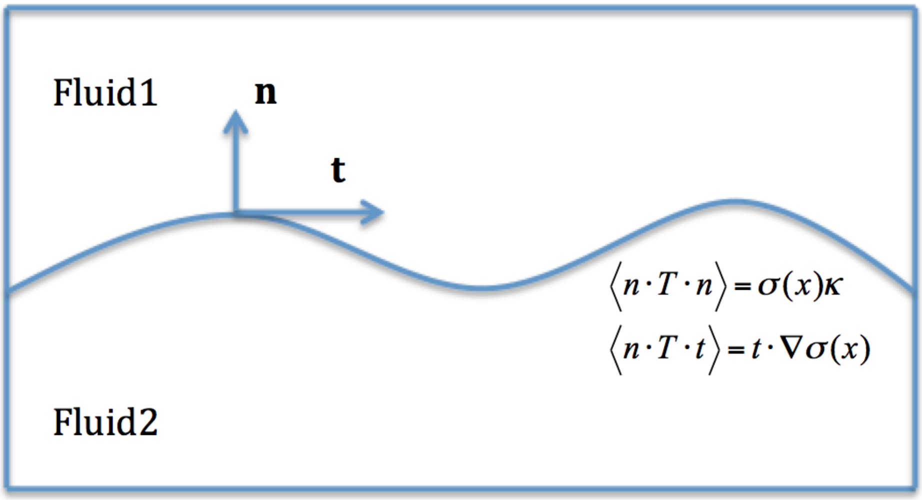

Figure 4.4: The schematic of two immiscible fluids and the corresponding stress boundary conditions

The variation of the surface tension coefficient leads to the tangential stress gradient at the interface:

$$\langle \mathbf{n}\cdot\mathbf{T}\cdot\mathbf{t}\rangle=\mathbf{t}\cdot\nabla\sigma(\mathbf{x}), \tag{4.12}$$

which drives the flow from a low surface tension part to a high surface tension tension part. $\mathbf{t}$ is the unit tangent vector of the interface.

In the CSF model, the volume force $\mathbf{F}_i$ induced by the surface tension and the Marangoni effect can be defined as:

$$\mathbf{F}_i(x)=\mathbf{f}_s(x)\delta(x-x_s), \tag{4.13}$$

where $\mathbf{f}_s$ is the surface tension force per unit interfacial area, δ is the Dirac delta function and x_s indicates the point on the interface. $\mathbf{f}_s$ is expressed as

$$\mathbf{f}_s=\kappa\sigma\mathbf{n}+\nabla_s\sigma. \tag{4.14}$$

Here ∇_s is the gradient operator along the interface and can be represented by

$$\nabla_s=\nabla-\mathbf{n}\frac{\partial}{\partial\mathbf{n}}. \tag{4.15}$$

The surface tension σ may depend on the temperature and concentration. If the surface tension is only influenced by the concentration, the following linear model can be assumed:

$$\sigma = \sigma_0(1 + \gamma c), \tag{4.16}$$

where σ_0 is the surface tension of a pure system, and γ is a negative constant value in most cases. Then equation (4.11) can be rewritten as:

$$\mathbf{f}_s = \kappa\sigma\mathbf{n} + \frac{\partial\sigma}{\partial c}(\mathbf{I} - \mathbf{nn}) \cdot \nabla c. \tag{4.17}$$

The body force $\mathbf{F}_i$ in the momentum equations (2.2) can now be written as:

$$\mathbf{F}_i(x) = \left(\kappa\sigma\mathbf{n} + \frac{\partial\sigma}{\partial c}(\mathbf{I} - \mathbf{nn}) \cdot \nabla c\right) \delta(x - x_s). \tag{4.18}$$

4.3 Mass transfer

In this section, the mass transfer due to the concentration gradient is examined. This mass transfer model was first developed by Ganguli & Kenig (2011a). To implement this method, some prerequisites are needed for the fluid-fluid system:

- Newtonian incompressible fluids.
- No chemical reaction.
- Isothermal system.
- Laminar flow.
- No surface active contaminants.

The governing mass transport equation for the incompressible fluid flow is as follows:

$$\frac{\partial c}{\partial t} + \mathbf{u} \cdot \nabla c = \nabla \cdot (D\nabla c). \tag{4.19}$$

Here, c is the concentration. Next, let us consider a two-phase flow system comprising a gas bubble (denoted as G) and a liquid phase (denoted as L). Then the mass transport equation can be re-written as:

$$\frac{\partial c_G}{\partial t} + \mathbf{u} \cdot \nabla c_G = \nabla \cdot (D_G\nabla c_G) \tag{4.20}$$

and

$$\frac{\partial c_L}{\partial t} + \mathbf{u} \cdot \nabla c_L = \nabla \cdot (D_L\nabla c_L), \tag{4.21}$$

where D_G and D_L are the mass diffusion coefficients for the gas phase and liquid phase, respectively. For the mass transport equation, two interfacial boundary conditions need to be fulfilled. First, the interfacial dissolution equilibrium is defined by the thermodynamic equilibrium assumption:

$$c_G = H_D c_L. \tag{4.22}$$

Here, H_D is the distribution coefficient that is used to measure the interfacial concentration jump. In the gas-liquid system, the amount of dissolved gas is proportional to its partial pressure in the gas phase. H_D is the proportional factor. In the liquid-liquid system, H_D is defined as a partition constant by the liquid-liquid solubility and varies from the values of solubility (Ramachandran, 2018). Second, the interfacial fluxes obey the continuity condition:

$$D_L \frac{\partial c_L}{\partial n} = D_G \frac{\partial c_G}{\partial n}. \tag{4.23}$$

The main idea of the mass transfer model is to combine the two interfacial boundary conditions (e.g., equation (4.22) and equation (4.23)) with the governing mass transfer equations for two-phase flow (e.g., equation (4.20) and equation (4.21). The interfacial boundary conditions are fulfilled only in the region very close to the interface, while outside this region the original mass transfer equations are applied.

In this way, the interfacial boundary conditions are directly implemented in the mass transfer equations as source terms and the following extended equations are obtained (Ganguli & Kenig, 2011a):

$$\frac{\partial c_G}{\partial t} + \mathbf{u} \cdot \nabla c_G = \nabla \cdot (D_G \nabla c_G) + \alpha_1 \left(D_L \frac{\partial c_L}{\partial n} - D_G \frac{\partial c_G}{\partial n} \right) \tag{4.24}$$

and

$$\frac{\partial c_L}{\partial t} + \mathbf{u} \cdot \nabla c_L = \nabla \cdot (D_L \nabla c_L) + \alpha_2 \left(c_L - \frac{c_G}{H_D} \right). \tag{4.25}$$

Here, α_1 and α_2 are two coefficients. In order to make sure the boundary conditions are only fulfilled at the interface, the values of α_1 and α_2 are set sufficiently high here (e.g., 10^5) and zero in the rest of the computational domain. The limitation of this strategy created by Ganguli & Kenig (2011a) is that, with regards to convergence, the values of α_1 and α_2 can be changed from 10^3 to 10^5, and the values of H_D can be set from 20 to 40.

These two extended mass transfer equations should run iteratively like reinitialization function for the conservative level set method. The iterations are terminated when the iterative error is smaller than the tolerance error. Here, the first boundary condition (equation (4.23)) has the function of mass transfer. The second one can be regarded as a convergence criterion. For each iterative step, equation (4.23) is used to control how much mass can be transferred from one side of the interface to the other; equation (4.22) is a stop criterion to determine when to move to the next time step, until this condition is fulfilled.

This method is available for any fluid-fluid system, and not limited to binary mass transfer. It can also be extended to multicomponent systems (Ganguli & Kenig, 2011a).

In Ganguli & Kenig (2011a), the mass transfer model is implemented using the Finite Element Method (FEM) in an interface-conforming grid. In order to adapt the mass transfer model to MGLET, which is applied with FVM, several modifications are employed. Implementing these two interfacial boundary conditions in MGLET is a great challenge: (1) How to maintain the mass conservation in the FVM after applying equation (4.23), (2) how to implement equation (4.22) on the arbitrary interface in the Cartesian coordinate system defined by the level set function. In the following, an alternative strategy to implement the mass transfer model will be discussed in detail.

4.3.1 Interfacial fluxes conservation

In the FVM, in order to maintain mass conservation, the flux entering a given volume is identical to that leaving the adjacent volume. Therefore, after initializing the interface located between cell centers i and $i+1$, one needs to determine on which side of the interface is the surface shared by points i and $i+1$ located (see figure (4.5)).

We consider the mass transfer from the gas phase to the liquid phase in the x-direction. First, the case of the liquid phase on the left side of the interface is examined. If the surface is on the side of the liquid phase shown in figure (4.5) a), a linear extrapolation is done to compute the concentration on the interface c_G^g from the gas phase,

$$c_G^g = \frac{3}{2}c_{i+1,j,k} - \frac{1}{2}c_{i+2,j,k}. \tag{4.26}$$

Here, $c_{i+1,j,k}$ and $c_{i+2,j,k}$ are the concentrations in the gas phase. Moreover, equation (4.21) can be rewritten as:

$$D_L \frac{c_L - c_{i,j,k}}{\Delta x/2} n_{i,j,k} = D_G \frac{c_{i+1,j,k} - c_G^g}{\Delta x/2} n_{i+1,j,k}, \tag{4.27}$$

where c_L is the real concentration on the surface in the liquid phase. Substituting equa-

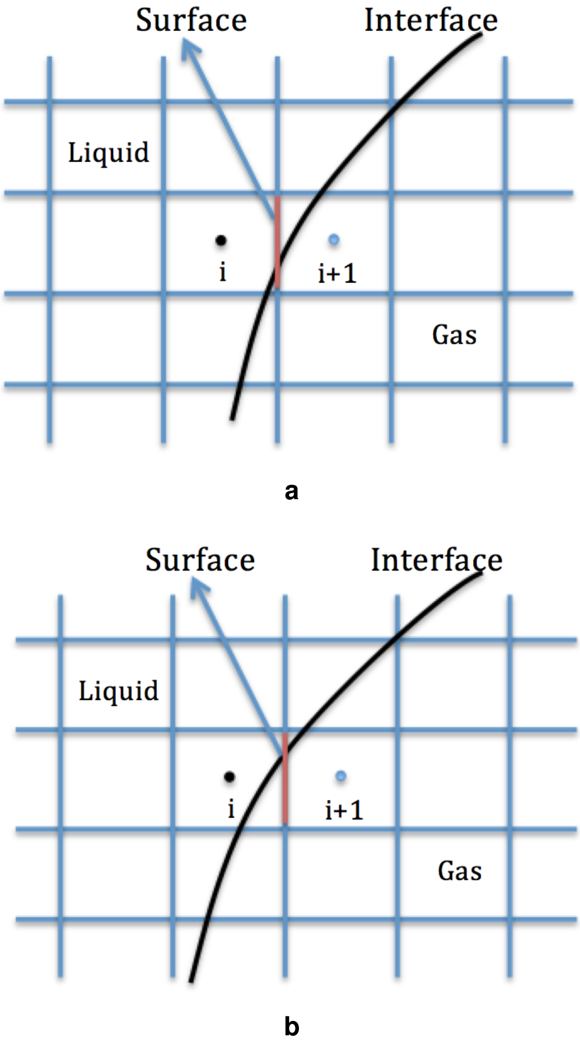

Figure 4.5: Liquid on the left side of the interface: (a) The surface is on the side of the liquid phase, (b) The surface is on the side of the gas phase

tion (4.26) into equation (4.27), we obtain:

$$c_L = \frac{D_G}{D_L}\frac{1}{2}(c_{i+2,j,k} - c_{i+1,j,k})(\frac{n_{i+1,j,k}}{n_{i,j,k}}) + c_{i,j,k}. \tag{4.28}$$

If the surface is on the side of the gas phase (see figure (4.5) b)), then

$$c_G = \frac{D_L}{D_G}\frac{1}{2}(c_{i-1,j,k} - c_{i,j,k})(\frac{n_{i,j,k}}{n_{i+1,j,k}}) + c_{i+1,j,k}. \tag{4.29}$$

Here c_G is the real concentration on the surface in the gas phase. The extension to the case that the liquid phase is on the right side of the interface is straightforward.

4.3.2 Interfacial dissolution equilibrium

The schematic of the concentration jump for the interfacial mass transfer at the interface is depicted in figure (4.6). Although the concentration varies in both phases, the interfacial concentration jump is defined by thermodynamic conditions (Ramachandran, 2018). $c_{L,interface}$ and $c_{G,interface}$ are the concentrations on the interface based on the Henry's law.

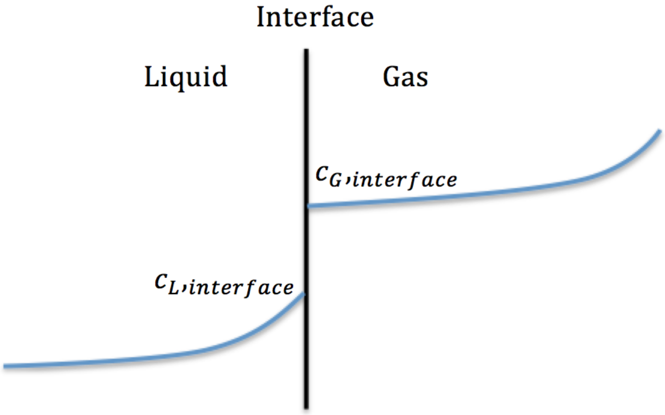

Figure 4.6: The schematic of the concentration jump at an interface

However, in our case, Henry's law is modified to be fulfilled on the surface of two control volumes, since FVM is implemented in MGLET.

Therefore, when the liquid phase is on the left side of the interface, equation (4.20) can be rewritten as:

$$c_L = \frac{c_G^g}{H_D} = \frac{1}{H_D}(\frac{3}{2}c_{i+1,j,k} - \frac{1}{2}c_{i+2,j,k}) \tag{4.30}$$

for the surface on the side of the liquid phase, and

$$c_L = \frac{1}{H_D}(\frac{D_L}{D_G}\frac{1}{2}(c_{i-1,j,k} - c_{i,j,k})(\frac{n_{i,j,k}}{n_{i+1,j,k}}) + c_{i+1,j,k}) \tag{4.31}$$

for the surface on the side of the gas phase.

The interfacial dissolution equilibrium can be treated as an objective function. The interfacial flux conservative condition needs to be fulfilled for each iterative time step until the objective function is reached, such that both interfacial boundary conditions are obeyed. Therefore, if the liquid is on the left side of the interface, the errors f^x_{LG1} and f^x_{LG2} between these two interfacial boundary conditions equation (4.28) and equation (4.30) in the x-direction can be obtained:

$$f^x_{LG1} = \frac{1}{H_D}(\frac{3}{2}c_{i+1,j,k} - \frac{1}{2}c_{i+2,j,k}) - \frac{D_G}{D_L}\frac{1}{2}(c_{i+2,j,k} - c_{i+1,j,k})(\frac{n_{i+1,j,k}}{n_{i,j,k}}) - c_{i,j,k} \tag{4.32}$$

and

$$f^x_{LG2} = \frac{1}{H_D}(\frac{D_L}{D_G}\frac{1}{2}(c_{i,j,k} - c_{i-1,j,k})(\frac{n_{i,j,k}}{n_{i+1,j,k}}) - c_{i+1,j,k}) + (\frac{3}{2}c_{i,j,k} - \frac{1}{2}c_{i-1,j,k}) \tag{4.33}$$

for the surface in the liquid phase and gas phase, respectively. For other locations and directions of the interface, the condition can be written accordingly.

Thus, the extended mass transfer equations (4.24) and (4.25) can be re-written as:

$$\frac{\partial c}{\partial t} + \mathbf{u} \cdot \nabla c = \nabla \cdot (D \nabla c) + \alpha f_{LG}, \tag{4.34}$$

where α is a coefficient that is set sufficiently high close to the interface and zero in the rest of the computational domain. Since the two interfacial boundary conditions are combined, in this case, we only need to apply the combined boundary condition once on either side of the interface.

A validation of this method will be given in section (5.4).

4.4 Time integration

A third order RK method is applied to the Navier-Stokes equations, level set advection and the transient mass transfer equation, while a second order RK method is applied to the reinitialization steps and the contact angle model. Because of these explicit algorithms, the time step size Δt must fulfill the Counrant-Friedrich-Lewy (CFL) conditions and also the restrictions due to gravity, viscous terms, surface tension, and diffusivity to stabilize the numerical simulations.

The convective time step is defined as

$$\Delta t_{conv} = \frac{h}{|\mathbf{u}|}. \tag{4.35}$$

The diffusive time step is defined as

$$\Delta t_{diff} = \frac{\rho h^2}{4\mu}. \tag{4.36}$$

The capillary time step is defined as (Brackbill *et al.*, 1992)

$$\Delta t_{cap} = \sqrt{\frac{(\rho_1 + \rho_2)h^3}{4\pi\sigma}}. \tag{4.37}$$

The gravity time step is defined as

$$\Delta t_{gra} = \sqrt{\frac{h}{g}}. \tag{4.38}$$

The mass diffusivity time step is defined as

$$\Delta t_{diffm} = \frac{h^2}{4D}. \tag{4.39}$$

When selecting a time step size, a regulation is given as

$$\Delta t \leq min(\Delta t_{conv}, \Delta t_{diff}, \Delta t_{cap}, \Delta t_{gra}, \Delta t_{diffm}). \tag{4.40}$$

The main steps of the algorithm are as follows:

1. Initialize all the parameters (density ρ, viscosity μ, surface tension σ, diffusivity D, concentration c, level set function φ, velocity field $\mathbf{u}$ and some coefficients) in each phase.

2. Construct the distance function ϕ from the level set function φ near the interface using FMM.

3. Calculate new density field ρ, viscosity field μ and concentration field c from the level set function φ, and curvature from the distance function ϕ.

4. Advance the flow variables, like velocity, pressure p and level set function, in time for one Runge-Kutta sub-step.

5. Compute the concentration iteratively, until the tolerance error is larger than the numerical one at the interface.

6. Repeat steps from 2 to 5 for each Runge-Kutta sub-step to obtain the new values for velocities, pressure, level set and concentration.

7. Reinitialize the level set φ iterativly with pseudo time step size $\Delta\tau$ and artificial diffusion number ϵ, which is similar to the concentration field in step 3, to maintain conservation.

5 Validation

Four test cases will be introduced in this chapter: in the first test case, a static pressure drop is used to test the accuracy of the surface tension force. These results are compared to previous studies to validate the current code. In the second test case, the capillary wave amplitude is discussed. The results of this test case can be used to predict capillary waves on an interface between two immiscible fluids with a density ratio of 1 and 1000. These results are also compared to previous studies to show the accuracy of the current implementation. The above two test cases are applied in Andre (2012) to validate the implementation of the CLS method. In the third test case, the case of a two-dimensional droplet on a wall without gravity is presented. The purpose of this test case is to show the improvements in the accuracy of the new contact line treatment for the CLS method. Finally, the result of the mass transfer with negligible external resistance is presented to validate the mass transfer model based on the CLS method (see section (4.3)).

5.1 Static drop

A method similar to the SSF model is used to model the surface tension force. In order to check the accuracy of this method, a static drop is simulated to investigate the strength of the parasitic currents. In numerical simulations, parasitic currents and pressure fluctuations tend to occur due to the inaccuracies in the curvature calculation.

The drop at diameter $D_d = 0.4$ is placed in the center of a unit domain. The velocity field is defined as zero in the whole domain. The analytical solution is zero and a pressure difference of $\Delta p = 5$ across the interface for the velocity field and pressure field, respectively. The Laplace number is used to characterize the static drop problem and defined as:

$$La = \frac{\sigma \rho_2 D_d}{\mu_2^2}. \tag{5.1}$$

The surface tension coefficient is defined as a constant $\sigma = 1$, the viscosity for both fluids is set to $\mu = 0.1$, and the value of the capillary time step size of $\frac{1}{2}\Delta t_{cap}$ (see section (4.4)) is used. The density ratio and viscosity ratio are both set to unity. The dimensionless capillary number is defined with the maximum magnitude of the velocity:

$$Ca = \frac{|U_{max}|\mu_2}{\sigma}, \tag{5.2}$$

and the time is indicated in the dimensionless form as below:

$$t_{sd} = \frac{t\sigma}{\mu_2 D_d}. \tag{5.3}$$

The dimensionless time is set to $t\sigma/\mu_2 D_d = 250$ for all test cases.

Table (5.1) shows the results for a 40 x 40 mesh with different Laplace numbers. These outcomes are similar to those reported by Desjardins *et al.* (2008), and indicate that the parasitic currents seem to be independent of the Laplace number.

La	120	12000	2000000
Ca	9.46 x 10^{-6}	2.12 x 10^{-5}	1.37 x 10^{-5}

Table 5.1: Dependence of the magnitude of parasitic currents on the Laplace number with a 40 x 40 mesh

Mesh	40x40	80x80	160x160
Ca	1.37 x 10^{-5}	8.79 x 10^{-6}	1.15 x 10^{-5}

Table 5.2: Dependence of the magnitude of parasitic currents on mesh spacing with La = 2x10^6

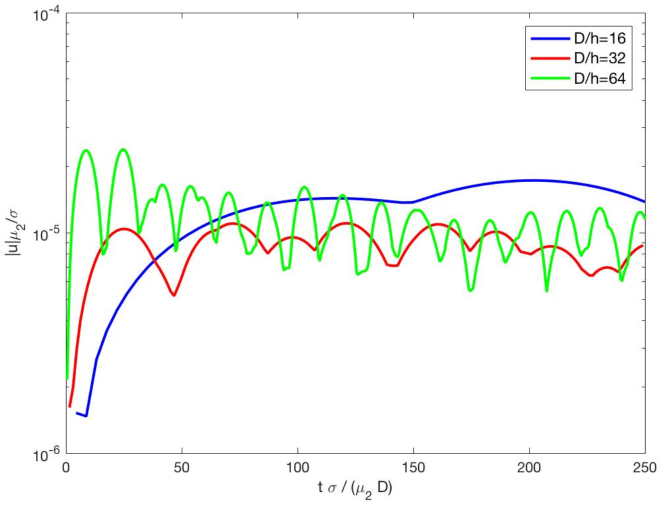

Figure 5.1: Parasitic currents time evolution

In order to investigate the mesh convergence of the parasitic currents, the Laplace number is fixed to La = 2x10^6, while mesh spacing is varied. In contrast to Desjardins *et al.* (2008) who concluded that the parasitic currents are first order convergence, results shown in Table (5.2) are observed to increase with refined grids. Moreover, no first order behavior can be detected, which can be explained by figure (5.1), indicating that this observation is a coincidence of this oscillatory mode. The results of various grid spacings depend on the time of measurement.

Next, the pressure is taken into account with $La = 2\text{x}10^6$, unit density and viscosity ratios. Figures (5.2) and (5.3) show that results are in good agreement with the analytical solution in all cases. Surprisingly, the errors in pressure for $D_d/H = 64$ are larger than those for $D_d/H = 32$, which can be explained by the lack of convergence of the parasitic currents. As seen in figure (5.1), the errors in parasitic currents are time dependent. These conclusions are dependent on the time at which observations are made.

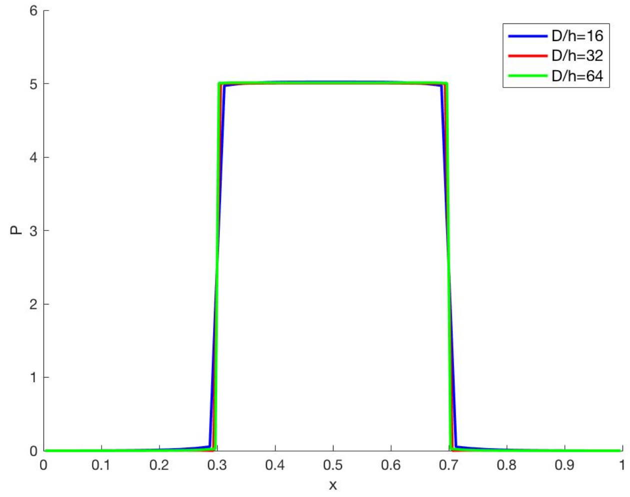

Figure 5.2: Numerical pressures for different meshes

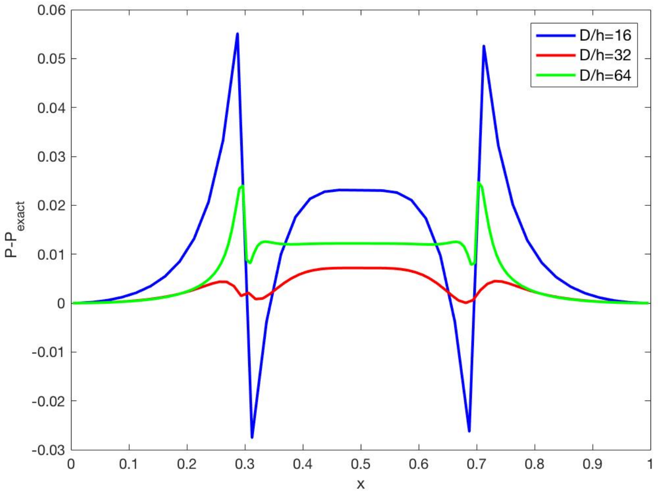

Figure 5.3: Error in Pressure

5.2 Capillary waves

Next, the viscous damping of a surface wave is discussed. This test case will help to assess the accuracy of numerical simulations and solve the problem of the interaction between viscous and surface tension forces. An interface is initialized in a $[0, 2\pi]$ x $[0, 2\pi]$ domain defined by the distance function:

$$\phi_0(x, y) = y - x + A_0 cos(x), \tag{5.4}$$

where $A_0 = 0.01\lambda$ is the initial wave amplitude and $\lambda = 2\pi$ is the wavelength of the perturbation. In this case, both fluids have the same kinematic viscosity ν. This was first investigated by Prosperetti (1981), who developed an analytical solution of the wave amplitude with time:

$$\begin{aligned} A_0(t) =& \frac{4(1-4\beta)\nu^2 k^4}{8(1-4\beta)\nu^2 k^4 + \omega_0^2} A_0 erfc(\nu k^2 t)^{\frac{1}{2}} \\ &+ \sum_{i=1}^{4} \frac{z_i}{Z_i} \left(\frac{\omega_0^2 A_0}{z_i^2 - \nu k^2} - u_0 \right) exp[(z_i^2 - \nu k^2)t] erfc(z_i t^{\frac{1}{2}}), \end{aligned} \tag{5.5}$$

where $\omega_0 = \sqrt{\frac{\sigma}{\rho_1+\rho_2} k^3}$ is the inviscid oscillation frequency, $k = 1$ is the wave number, $u_0 = 0$ is the initial velocity and $\beta = \frac{\rho_1 \rho_2}{(\rho_1+\rho_2)^2}$ is the dimensionless parameter. The z_i are the roots of the equation

$$z^4 - 4\beta(k^2\nu)^{\frac{1}{2}} z^3 + 2(1-6\beta)k^2\nu z^2 + 4(1-3\beta)(k^2\nu)^{\frac{3}{2}} z + (1-4\beta)\nu^2 k^4 + \omega_0^2 = 0 \tag{5.6}$$

and

$$Z_i = \prod_{j=1, j\neq i}^{4} (z_j - z_i). \tag{5.7}$$

Two test cases are investigated: the first case with unity density ratio and the second one with a density ratio of 1000. For both cases, four different grid spaces have been evaluated, a 16 x 16 mesh, a 32 x 32 mesh, a 64 x 64 mesh and a 128 x 128 mesh. A fixed surface tension coefficient $\sigma = 2$ is used in both cases.

In the first test case, the kinematic viscosity for both fluids is set to $\nu = 0.064720863$, and the density for both fluids is set to $\rho = 1$. A fixed time step size $\Delta t = 0.003$ is applied. This case is performed up to a time of $\omega_0 t = 24$. The time evolution of the normalized capillary wave amplitude for the different meshes as well as the analytical solution are shown in figure (5.4); the time evolution of the amplitude errors is depicted in figure (5.5). The Root Mean Square (RMS) errors between the theoretical solution and the numerical results are shown in table (5.3) using the same time period.

In figures (5.4) and (5.5), the result of the 16 x 16 mesh has a slightly larger oscillation than the other meshes. After the grid has been refined, an expected improvement in the results is observed. The rate of convergence observed in table (5.3), according to Herrmann (2008) and Desjardins *et al.* (2008) is approximately second order. The order of Herrmann (2008) decreases to first order on finer grids. The results obtained by Desjardins *et al.* (2008) has a strong agreement with the analytical solution even with a coarse 16 x 16 mesh. With the current implementation, the rate of convergence remains first order approximately, but does not reach the second order. The results in Andre (2012) which are implemented with fourth order preprocessing, differ slightly from the current study, using second order implementation.

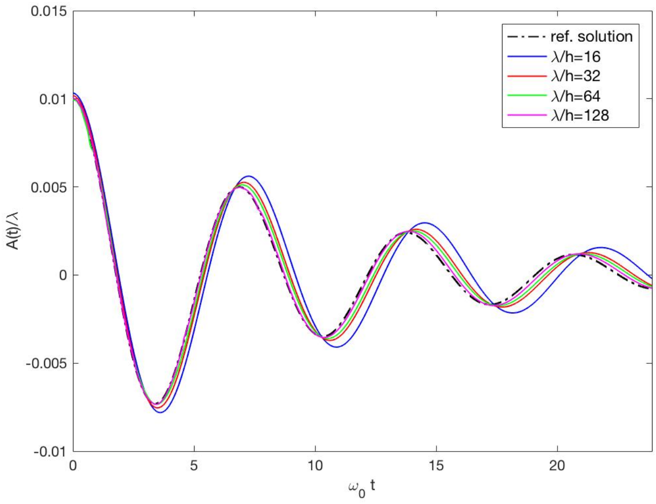

Figure 5.4: Time evolution of the capillary wave amplitude for $\rho_2/\rho_1 = 1$

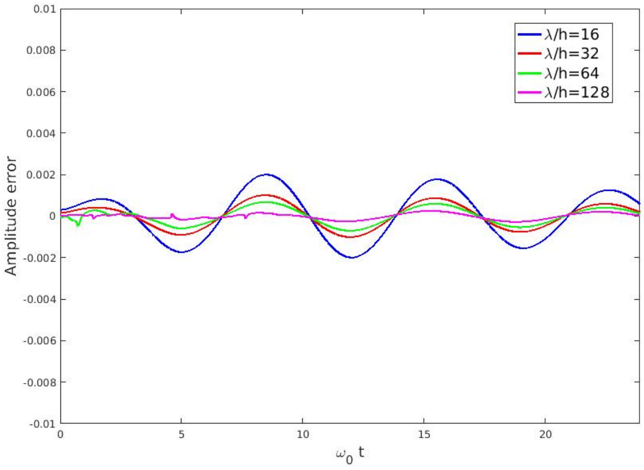

Figure 5.5: Time evolution of the amplitude errors for $\rho_2/\rho_1 = 1$

λ/h	8	16	32	64	128
E_{RMS}		0.1176	0.0586	0.0390	0.0143
E_{RMS}, Andre (2012)		0.1601	0.0717	0.0403	0.0170
E_{RMS}, Herrmann (2008)		0.1116	0.0295	0.0114	0.0067
E_{RMS}, Desjardins *et al.* (2008) ($\omega_0 t < 24$)	0.1997	0.0395	0.0104		

Table 5.3: Capillary wave RMS error for $\rho_2/\rho_1 = 1$ ($\omega_0 t < 24$)

In the second test case, the densities are set to $\rho_1 = 1$ and $\rho_2 = 1000$. The kinematic viscosity is the same as the first test case $\nu_1 = \nu_2 = 0.0064720863$, a time step size of $\Delta t = 0.06$ is chosen, and the results are simulated for $\omega_0 t < 20$.

In figures (5.6) and (5.7) we can observe that the result with a 16 x 16 mesh is much better than with a 32 x 32 mesh. All the results have good agreement with the theoretical solution, and the results of Andre (2012) are similar to the current implementation. Moreover, the result of Desjardins *et al.* (2008) shows better accuracy, as shown in table (5.4). The current implementation still performs as first order except for the 16 x 16 mesh, while the results of Herrmann (2008) does not maintain convergence at finer grids.

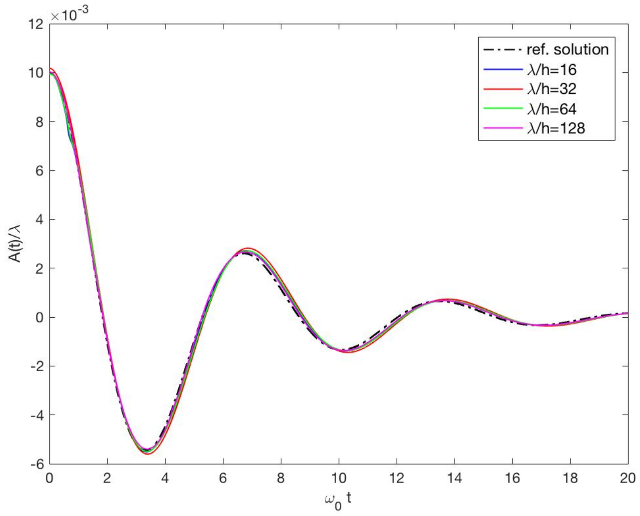

Figure 5.6: Time evolution of the capillary wave amplitude for $\rho_2/\rho_1 = 1000$

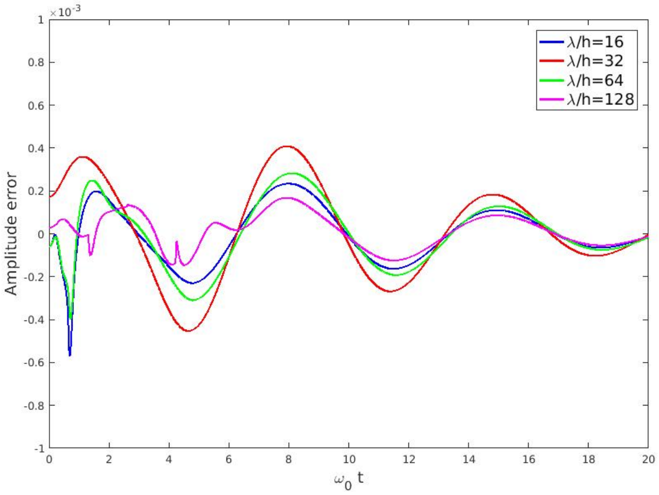

Figure 5.7: Time evolution of the amplitude errors for $\rho_2/\rho_1 = 1000$

λ/h	8	16	32	64	128
E_{RMS}		0.0131	0.0224	0.0153	0.0081
E_{RMS}, Andre (2012)		0.0666	0.0271	0.0153	0.0085
E_{RMS}, Herrmann (2008)		0.0482	0.0208	0.0127	0.0118
E_{RMS}, Desjardins *et al.* (2008) ($\omega_0 t < 20$)	0.0892	0.0204	0.0097		

Table 5.4: Capillary wave RMS error for $\rho_2/\rho_1 = 1000$ ($\omega_0 t < 20$)

5.3 Two-dimensional droplet on a wall under zero-gravity conditions

The simulation of a two-dimensional droplet melting on a flat plate was discussed in Zahedi *et al.* (2009) and Sato & Ničeno (2012). In order to compare the accuracy of the present method for estimating the contact angle and the wetting velocity, this case has been re-computed. The drop sits on a solid surface surrounded by another liquid with the identical density and viscosity. The static contact angle is $\theta_s = 25°$. Gravity is neglected meaning that capillary effects dominate.

In experiments performed by Hoffman (1975) with viscosity ratio ranges between 10^{-5} and 10^{-8}, the results showed that the contact angle is a function of the capillary number Ca^*. Later, a more general analysis of the dynamics of wetting was presented by Cox (1986), which is regarded as an analytical solution.

5.3.1 Cox' theory

For a given system of two immiscible fluids with viscosity ratio λ, Cox's theory assumes that

$$g(\theta_D,\lambda) - g(\theta_s,\lambda) = Ca^* ln(\delta_c^{-1}), \tag{5.8}$$

where θ_D is the macroscopic dynamic contact angle, δ_c is a constant term, θ_s is the static angle and the function $g(\theta,\lambda)$ is defined as

$$g(\theta_D,\lambda) = \int_0^\theta \frac{d\theta}{f(\theta,\lambda)}, \tag{5.9}$$

where

$$f(\theta,\lambda) = \frac{2\sin\theta(\lambda^2(\theta^2-\sin^2\theta)+2\lambda(\theta\pi-\theta)+\sin^2\theta)+(\pi-\theta)^2-\sin^2\theta}{\lambda(\theta^2-\sin^2\theta)((\pi-\theta)+\sin\theta\cos\theta)+((\pi-\theta)^2-\sin^2\theta)(\theta-\sin\theta\cos\theta)}. \tag{5.10}$$

Therefore, Cox's theory is used to predict the macroscopic dynamic contact angle for two immiscible fluids. When the system reaches the steady state, the contact line speed Ca^* is zero. Thus, the macroscopic dynamic contact angle θ_D becomes the static contact angle θ_s as expected.

Results from Hoffman's profile for all values of the dynamic contact angle (except those very close to 180°) have good agreement with the formula obtained from Tornberg & Engquist (2000). Zahedi *et al.* (2009) confirmed that a value of $\delta \approx 10^{-4}$ minimizes the relative difference between the contact-line speeds Ca^* obtained from Hoffman's experiments using silicone fluid with $\lambda = 0$ and $\theta_s = 0$ and those obtained from Cox's theory. In the following part, $\delta = 10^{-4}$ will be applied.

5.3.2 Results

The interface of the droplet is initialized in a $[-2,2]$ x $[0,2]$ domain. The location of the droplet is around $x = 0$ with radius $L_x/r = 8$. At initial time, the contact angle between the drop and the solid wall is applied with 156°. The Reynolds number and the Capillary number are defined as

$$Re = \frac{\rho u l}{\mu} = 1, \tag{5.11}$$

where l is the diameter of the droplet. And the dimensionless contact-line speed is expressed as:

$$Ca^* = \frac{2\sqrt{2}\mu u}{3\sigma} = 1. \tag{5.12}$$

A time step size is according to the capillary limitation (see section (4.4)). If the static contact angle is $\theta_s = 25°$ at the wall, we obtain

$$tan(90° - \theta_s) = tan 65° = |\frac{n_y}{n_x}|, \tag{5.13}$$

since the vector is normalized, thus

$$n_y^2 + n_x^2 = 1. \tag{5.14}$$

Therefore, the boundary condition for the normal vector field discussed in section (4.1) is set as:

$$\mathbf{n}_{wall} = (n_x, n_y) = (-sign(x)0.4226, -0.9063). \tag{5.15}$$

The Neumann boundary conditions are implemented for the other boundaries.

The dynamic contact angle is calculated between the tangential line from the inflexion point and the wall as shown in figure (5.8). The inflexion point is a point on a continuously differentiable curve at which the curve changes from concave to convex, or vice versa. Thus, the inflexion point can be obtained by calculating the local minimum or maximum tangent. The wetting speed is measured by the position of the intersection point on the wall at different time steps.

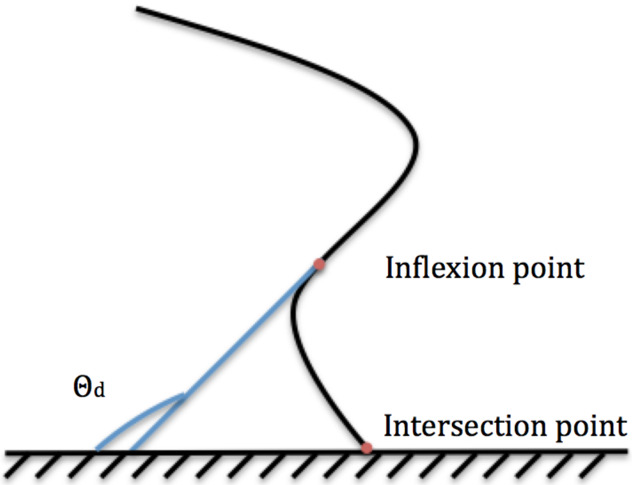

Figure 5.8: The measurement of the contact angle and the wetting speed.

The profiles of the droplet wetting on the solid wall are illustrated for different time steps in figure (5.10). A foot formed at the initial time due to the boundary conditions of the normal vector field at the wall. The curvature is a driving force to move the droplet to wet the surface. The movement of the contact line is fast at the initial steps, however slows down when the contact angle approaches equilibrium. The results of the contact angle are in agreement with the studies of Zahedi *et al.* (2009) and Sato & Ničeno (2012) as seen in table (5.5).

The contact angle at $300s$ is relatively larger than the expected 25°. The reason is that the contact angle is defined as 25° at the wall boundary. However, due to the characteristics of the staggered grid, the normal vector and the level set function are stored in the center of the cells. Therefore, we can only measure the contact angle at the center of the cells, rather than at the wall boundary.

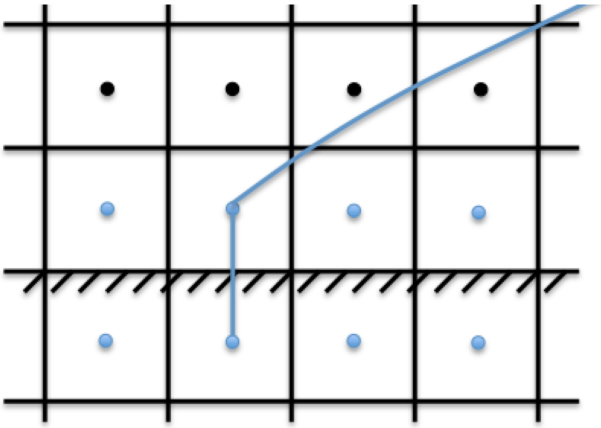

Figure 5.9: The interface based on the FVM and staggered grid.

Time	0.0	0.1	1.0	25.0	300
Presentstudy	156	144	123	60	28
Zahedi *et al.* (2009)	156	147	126	55	28
Sato & Ničeno (2012)	156	149	120	–	27

Table 5.5: Comparison of the contact angle of a liquid droplet on a solid surface.

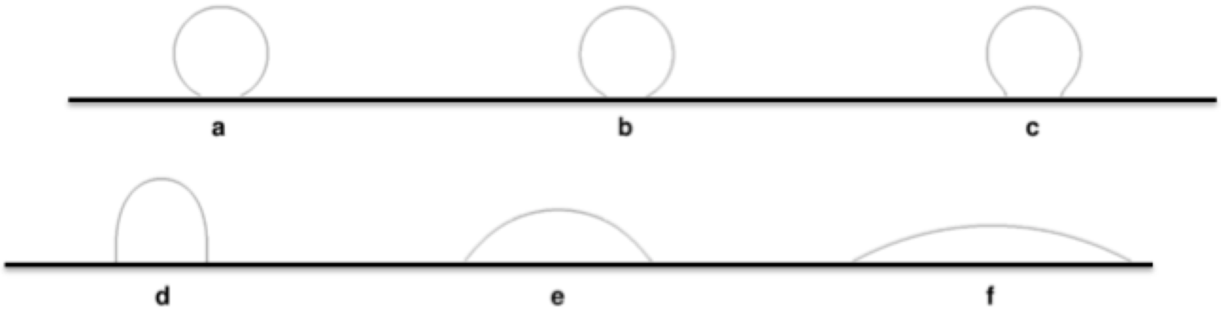

Figure 5.10: Wetting of a liquid drop on a solid surface (0.0s (a), 0.1s (b), 1.0s (c), 5.0s (d), 25s (e), 300s (f)).

The results of the contact angle against the capillary number are shown in figure (5.11). In this case, the wetting speed is equal to the Capillary number as $Ca^* = \frac{2\sqrt{2}\mu u}{3\sigma} = \frac{u}{u_{ref}} = 1$. The simulation is performed with 250 x 128 cells which is similar to the fine grid in Sato's study. The values in the present study show good agreement with previous results.

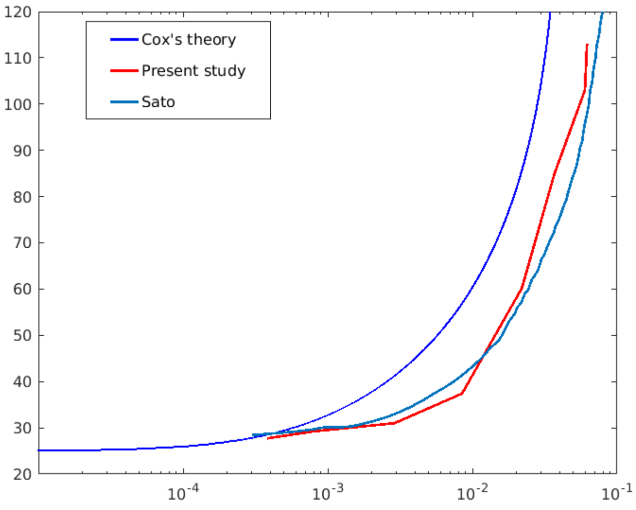

Figure 5.11: The contact angle as a function of the capillary number.

5.4 Mass transfer of a two-dimensional droplet with negligible external resistance

A test case is calculated to validate the mass transfer model implemented in MGLET. A drop is located in the center of a unit domain with slip boundary conditions. The velocity field is set to zero in the whole domain. For a stagnant spherical drop with negligible external mass transfer resistance, the analytical Sherwood number can be derived by Newman's equation (Newman, 1931):

$$Sh_{od} = \frac{2\pi^2}{3}\sum_{n=1}^{\infty} exp(-n^2\pi^2\tau_p) / \sum_{n=1}^{\infty}\frac{1}{n^2} exp(-n^2\pi^2\tau_p), \tag{5.16}$$

where $\tau_p = \frac{Dt}{r^2}$ is the dimensionless time step. Therefore, the steady asymptotic value is:

$$(Sh_{od})_{\tau_p\to\infty} = \frac{2\pi^2}{3} = 6.58. \tag{5.17}$$

The mass transfer coefficient to a single drop dominated by internal resistance can be evaluated by equation (2.23). In the two-dimensional case, $V/S = r/2$. The corresponding Sherwood number is

$$Sh_{od} = k_{od}\frac{2r}{D}. \tag{5.18}$$

Both phases have the same density, kinematic viscosity and mass diffusivity. Additional, the distribution coefficient H_D is set to 1. The concentration field is initialized as:

$$c_1 = 1 \quad \text{at t=0 (continuous phase)} \tag{5.19a}$$

$$c_2 = 0 \quad \text{at t=0 (drop phase).} \tag{5.19b}$$

Figure (5.12) shows the results of three different grid spacings and the analytical solution. As the grid is refined, the predicted Sherwood number converges close to the analytical solution. The relatively error of the grid with 400 x 400 nodes is 5%. This grid spacing is qualitatively sufficient for spatial computational accuracy and applied in the following (see Chapter 7).

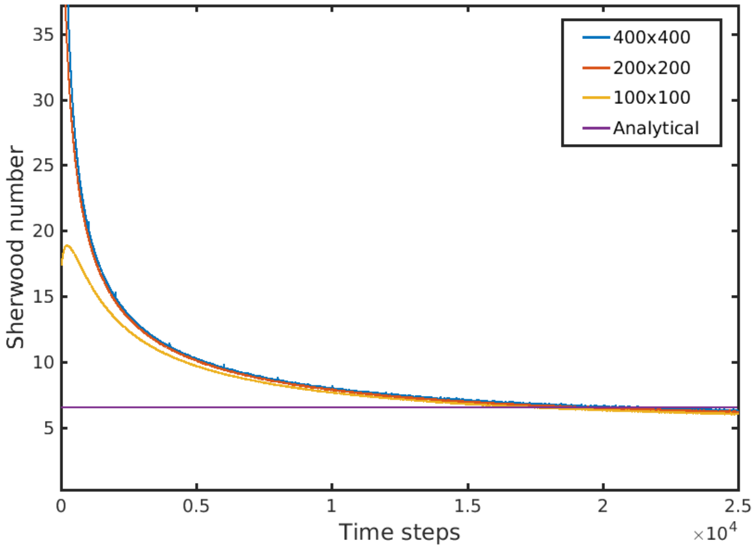

Figure 5.12: The comparison of predicted internal Sherwood number with analytical solution

6 Application 1: Purging of non-aqueous phase liquids from a 2D cavity model

A numerical investigation of the purging of non-aqueous phase liquids from a two-dimensional cavity model is undertaken. Due to NAPLs low solubility, only convective mass transfer will be taken into account. Our numerical results show that the flow conditions, such as Ri, We, density ratio and time scale significantly impact the mass transfer rate and the behavior of the interface.

6.1 Cavity flows

Since NAPLs may stay underground for several decades due to their low solubility in water, a long-term threat to drinking water supplies can be generated. Therefore, the influencing factors and the properties of mass transfer between NAPLs and water in pore-scale are significant. Then the cavity model is the simplified setup of the original setup of a micro-model.

Cavity models are widely used to study complicated phenomena, such as shear layer instability, vortex shedding and flow-induced vibrations. A simple cavity model is the lid-driven cavity flow. A number of studies have been conducted on the driven cavity flow problem using various numerical approaches (e.g. Erturk *et al.* (2005), Abouhamza & Pierre (2003) and Liffman (1996)).

Another important area of the cavity flow is a model that contains a channel with a cavity underneath. This kind of model is widely employed to analyze flow mechanisms (Crook *et al.* (2013), Chen *et al.* (2014) and Allegrini *et al.* (2014)), mass transfer (Kirkpatrick *et al.* (2012), Liu *et al.* (2004) and Occhialini & Higdon (1992)) and heat transfer (Brown & Lai (2005), Khanafer *et al.* (2002) and Leong *et al.* (2005)).

Chang *et al.* (1987) investigated the mass transfer in the cavity due to an external channel flow with various aspect ratios, the Re number and the Sc number. Occhialini & Higdon (1992) studied a numerical simulation of convective mass transfer from rectangular cavities in low Reynolds number flows. Brown & Lai (2005) conducted the combined heat and mass transfer from a horizontal channel with a cavity heated below. Liu *et al.* (2004) used a large eddy simulation to investigate pollutant transport in a street canyon with different aspect ratios. Kirkpatrick *et al.* (2012) examined the shear driven entrainment of a negatively buoyant fluid from trapezoidal cavities caused by a turbulent overflow numerically and experimentally.

However, all of these studies are 'single phase flows', since they do not employ a system of two immiscible fluids, where one is located in the channel and the other in cavity, nor interface tracking methods. As a result, the behavior of the interface and the mass transfer rate influenced by the surface tension force cannot be specified. The objective of the present work is to analyze the mass transfer rate solely due to the convective effect with the interface tracking method with the two immiscible flow system in the cavity model.

Simple cavities are typically described as rectangular, with a particular length l, width w and depth d (see figure (6.1)). The non-dimensional aspect ratio l/d is important, different flow regimes exist depending on this ratio (Charwat *et al.* (1961), Ashcroft & Zhang (2005)).

A cavity is defined as being deep at $l/d \leq 1$ (Sarohia, 1977). A shallow cavity ($l/d > 1$) can be further described as open or closed according to the location of the flow reattachment (see figure (6.2)).

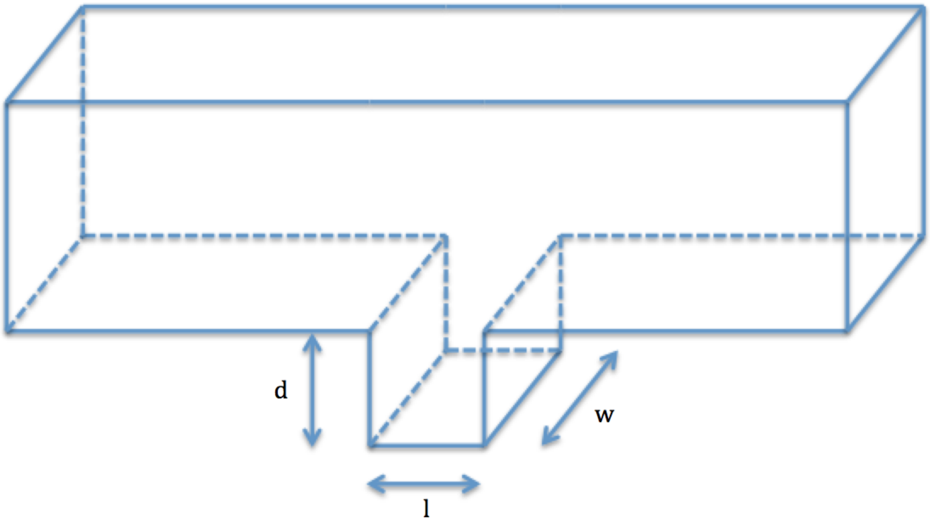

Figure 6.1: Sketch of a simple 3D cavity model

Open-shallow cavity flow: This flow exists for $l/d \leq 6-7$. It is characterized by a shear layer that bridges the entire cavity opening and by a large recirculation zone inside the cavity.

Closed-shallow cavity flow: This flow exists for $l/d \geq 8-9$. The shear layer generated at the leading edge touches the bottom of the cavity, and no large recirculation zone exists in the center of the cavity. Between these two ranges, a transitional regime exists.

6.2 Model set-up

Since a low Reynolds number is applied in the present work, a two-dimensional deep cavity model with aspect ratio 1 is implemented, as shown in figure (6.3). The cavity is filled with

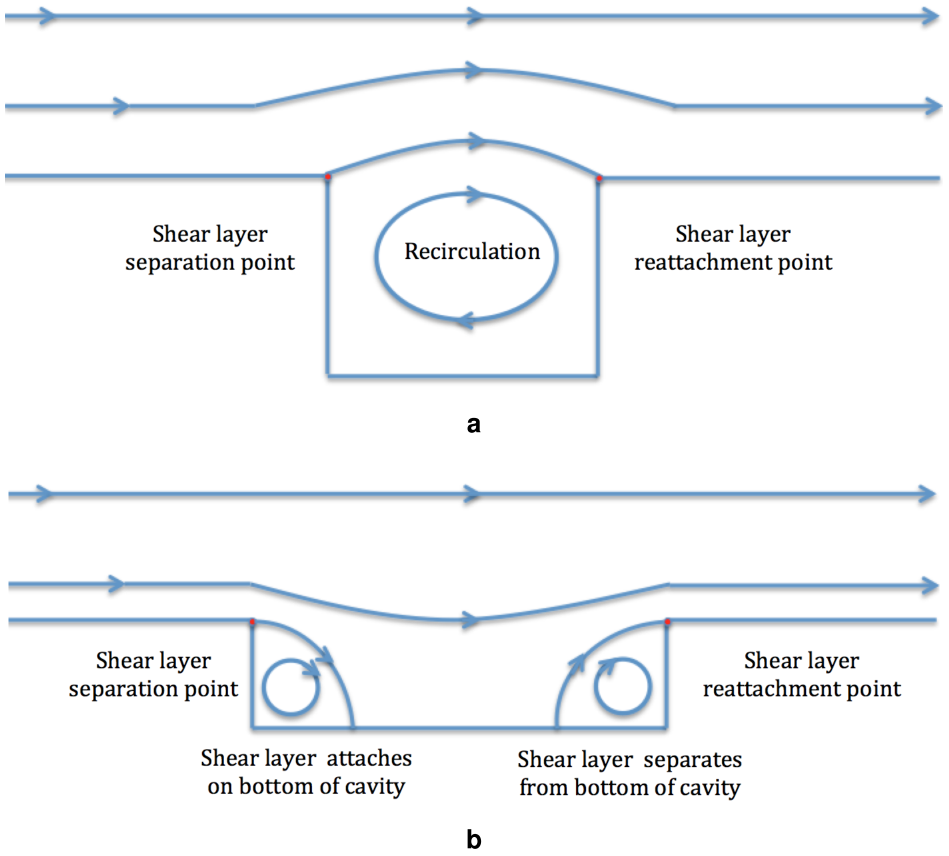

Figure 6.2: Two-dimensional representation of (a) open-type cavity flow and (b) closed-type cavity flow.

a NAPL, which is immiscible with water. We assess the fraction of NAPL flushed from the cavity due to the surface tension and density fraction with and without the influence of gravity. In addition, we examine the effect of flow acceleration, i.e. how fast the steady state velocity is reached. To do this, we enforce an inflow boundary condition on the velocity field using an exponential relaxation to reach the steady state,

$$u = u_0 \left(1 - \mathrm{e}^{-\frac{t}{\tau_0}}\right). \tag{6.1}$$

In this formula, τ_0 is a time scale and u_0 is a constant.

The walls are regarded as no slip surfaces (including the top wall) for velocity fields, and treated as Neumann boundary conditions (without flux) for the scalar field (level set function). Fixed and convective boundary conditions are used at the inflow and outflow, respectively. A connect boundary condition communicates boundary information to neighboring grids. In the following, subscript 1 indicates the fluid in the channel and 2 the fluid in the cavity. The interface initially is located in the cavity as a straight line with $0.9L$ height.

The Weber number (We) and the cavity Reynolds number (Re_{cavity}) are defined using the properties of the fluid in the cavity,

$$We = \frac{\rho_2 u_0^2 L}{\sigma} \tag{6.2}$$

and

$$Re_{cavity} = \frac{\rho_2 u_0 L}{\mu_2}, \tag{6.3}$$

where u_0 is the inflow velocity coefficient and L is the depth of the cavity.

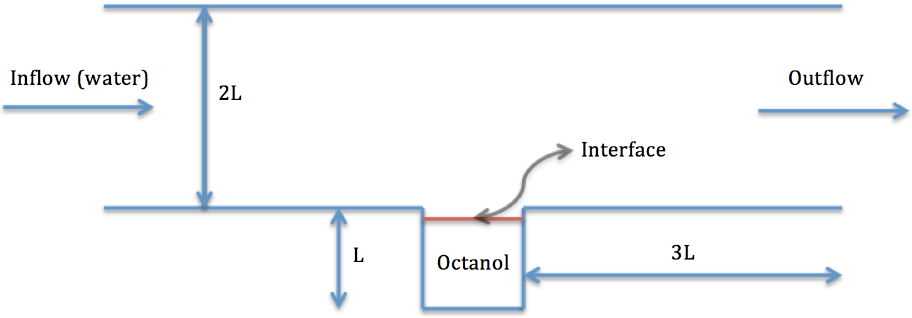

Figure 6.3: Sketch of flow in a channel with a bottom 2D cavity

6.3 Two-dimensional and three dimensional model

The two-dimensional model is employed in this chapter. Since the deep cavity model is applied (i.e., the streamline connects the entire cavity opening), three-dimensional model is not necessarily needed to be conducted. However, in order to investigate if there are several additional effects will happen in the three-dimensional model, rather than the two-dimensional model, results of the two-dimensional and three-dimensional models are compared in this section. The configuration of the three-dimensional model is shown in figure (6.4). The model extends three times in the spanwise direction for the channel part, and the cavity is located in the center of the bottom surface of the channel.

The comparison is shown in figure (6.5). The mass left in the cavity is normalized by the mass at the original state. In the beginning phase, the results of the two-dimensional and three-dimensional models are nearly the same. After approximately one second, the difference between the two cases becomes visually. Then after reaching the steady state, the results converge to 0.89 and 0.92 for two-dimensional and three-dimensional cases, respectively (i.e. the mass left in the three-dimensional case is more than that in the two-dimensional case).

The variance can be explained by the wall effect.

Figure (6.6) shows two slices of the cavity in the streamwise direction, one slice in the spanwise direction and one from the two-dimensional case. (b) is very close to the wall. As no-slip boundary conditions are applied to all surfaces of the cavity (except the top surface), the wall effect, rather than the convective effect from the overflow, has a strong influence on the velocity field and interface. This interface inhibits the mass transfer from the cavity. (a) is the slice in the middle and is similar to the two-dimensional case (d), mainly affected by the convective effect. Due to the inconsistency in the spanwise direction (see (c)), the three-dimensional result is different from that in the two-dimensional case. Thus, in our case where the low Weber number and Reynolds number are applied, except for the wall effect, no other additional effect can impact the mass transfer in the three-dimensional case. In the present work all the simulations are implemented using the two-dimensional model.

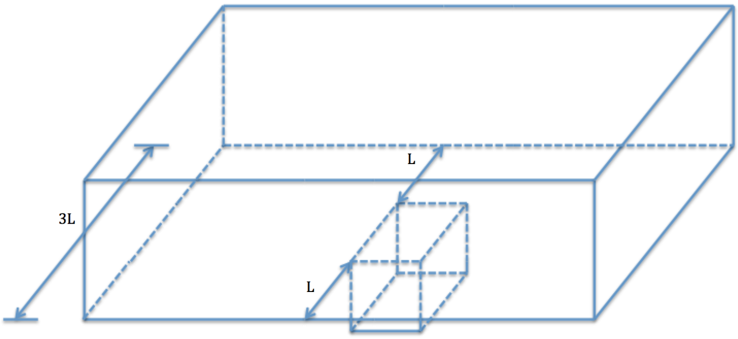

Figure 6.4: Sketch of the three dimensional model

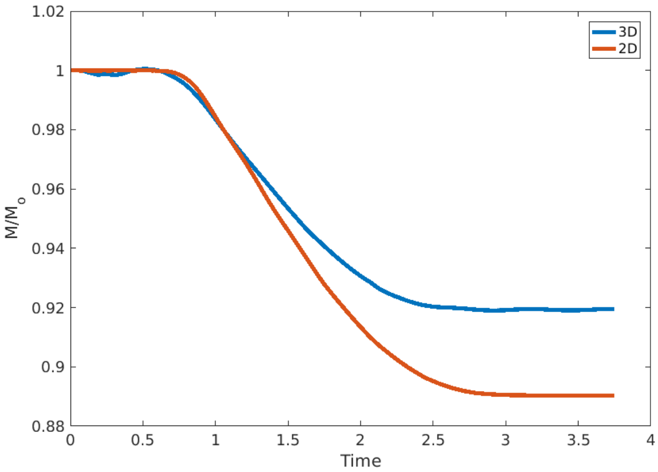

Figure 6.5: Results of the 2D and 3D model with $We = 25$, $Re = 1000$, the density and viscosity ratios are one and the time scale is also one

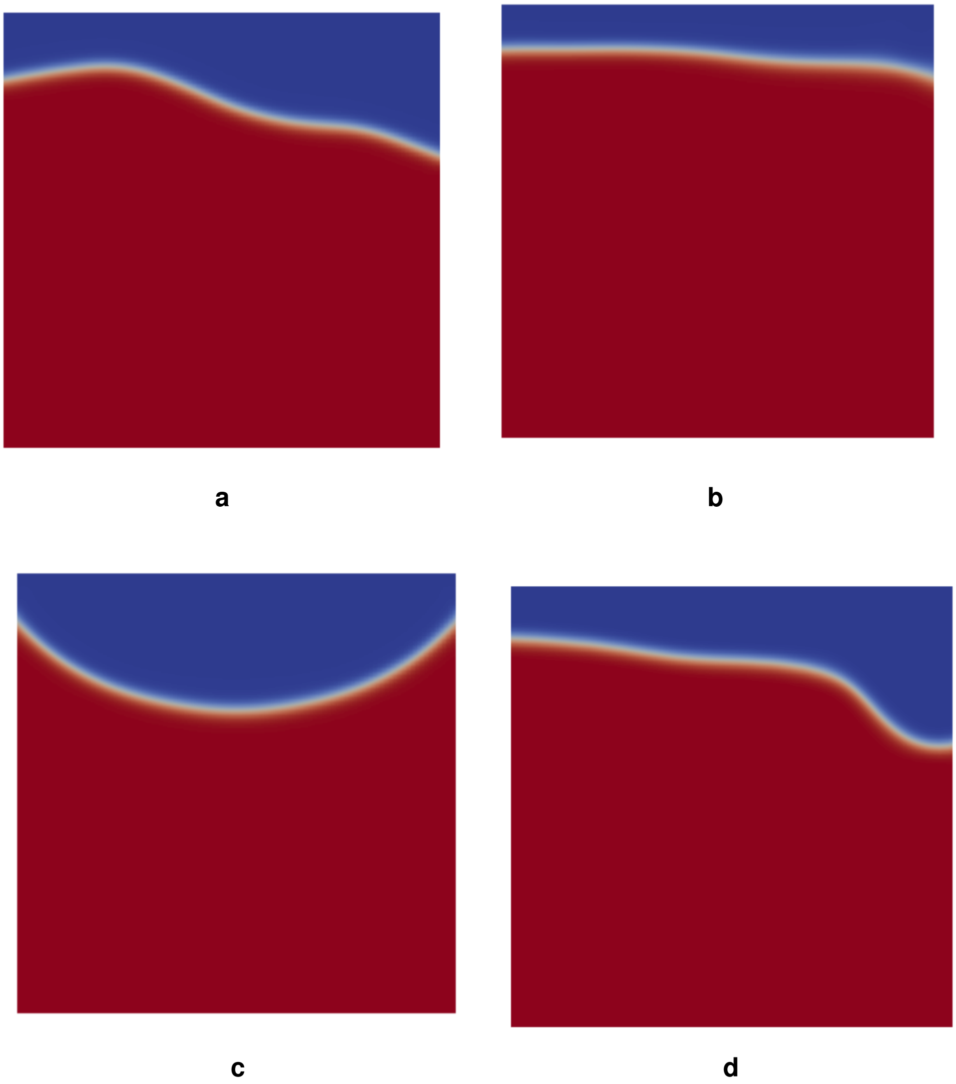

Figure 6.6: Spanwise slices of the cavity in three-dimensional model (a) y=0.500 (b) y=0.005 (c) x=0.95 (d) 2D case result after $4.25s$. The same parameters are set as figure (6.5).

6.4 Flushing the cavity

The motion of the mainstream in the channel has a significant impact on the behavior of the interface, the fluid movement in the cavity and the mass transfer rate. In this section, different numerical simulations with two different Weber numbers (i.e., surface tension coefficient) are analyzed. Both density and viscosity ratios are one in all cases. The cavity Reynolds number is 1000 and the dimensionless time scale ratio $\tau = \tau_0/(L/u_0)$ is set to 1. The gravitational force is neglected in this case.

The first case is conducted with $We = 100$. The time evolution of the interface and of the streamlines in the cavity are depicted in figure (6.7) to figure (6.11).

Figure (6.7) shows the interface and streamlines at $t = 0.4s$ after flow initiation. At this time, no NAPL has been pushed out of the cavity by the overflow, while at the leading corner of the cavity the interface has been pushed down slightly. Additionally, two small vortices are generated near the leading and trailing corners.

In Figure (6.8), mass being pushed out of the cavity at the trailing corner. The vortex close to the leading edge grows, while the one near the trailing edge disappears. Several streamlines from the mainstream can be observed entering and traversing the cavity, then exiting at the trailing corner.

Figure (6.9) indicates that the vortex close to the leading corner of the cavity becomes considerably large, while the process of mass transfer continues. The crest observed in the interface contour is now being rolled up by the vortex. The exiting part of the mass in the channel impacts the distribution of the streamlines.

The results at $t = 4s$ after initiation are represented in figure (6.10). The splash of the NAPL has now completely exited the cavity and is being convected to the boundary by the overflow. The vortex, initially located at the leading corner, has moved across the cavity and is nearly touching the trailing wall. At the same time, the vortex has become considerably large and almost fills the cavity. Furthermore, it starts to separate into two parts. Contrary to results in figure (6.9), no streamlines enter and traverse the cavity, since the mass transfer process is complete.

Two steady state vortices are shown in figure (6.11). The streamlines indicate that one vortex center is located near the trailing wall with a clockwise rotation, while a counter-clockwise-rotating vortex has formed in the lower part of the cavity near the leading corner. At this time all mass in the channel has been transported outside the domain. The interface, initially defined as a horizontal line between the overflow and the NAPL, has now changed into an inclined line in the cavity once steady state is reached, due to the high Weber number. The interface is located between these two vortices.

While the short initiation is uneventful, mass transfer starts and completes relatively quickly. The flow acceleration is inviscid in the initiation phase. This is the phase in which mass is pushed out of the cavity. In this phase, mass transfer mainly depends on the potential flow, rather than the complicated flow mechanisms in the following transient phase. Afterwards, the interface tends to reach the minimum energy state under the effect of the surface tension force. Finally, after reaching steady state, the interface becomes an inclined line in the cavity. The location of the interface is between the two vortices in the cavity. Moreover, the interface is parallel to the streamlines, rather than cross the streamlines which drives the movement of the interface before the steady state.

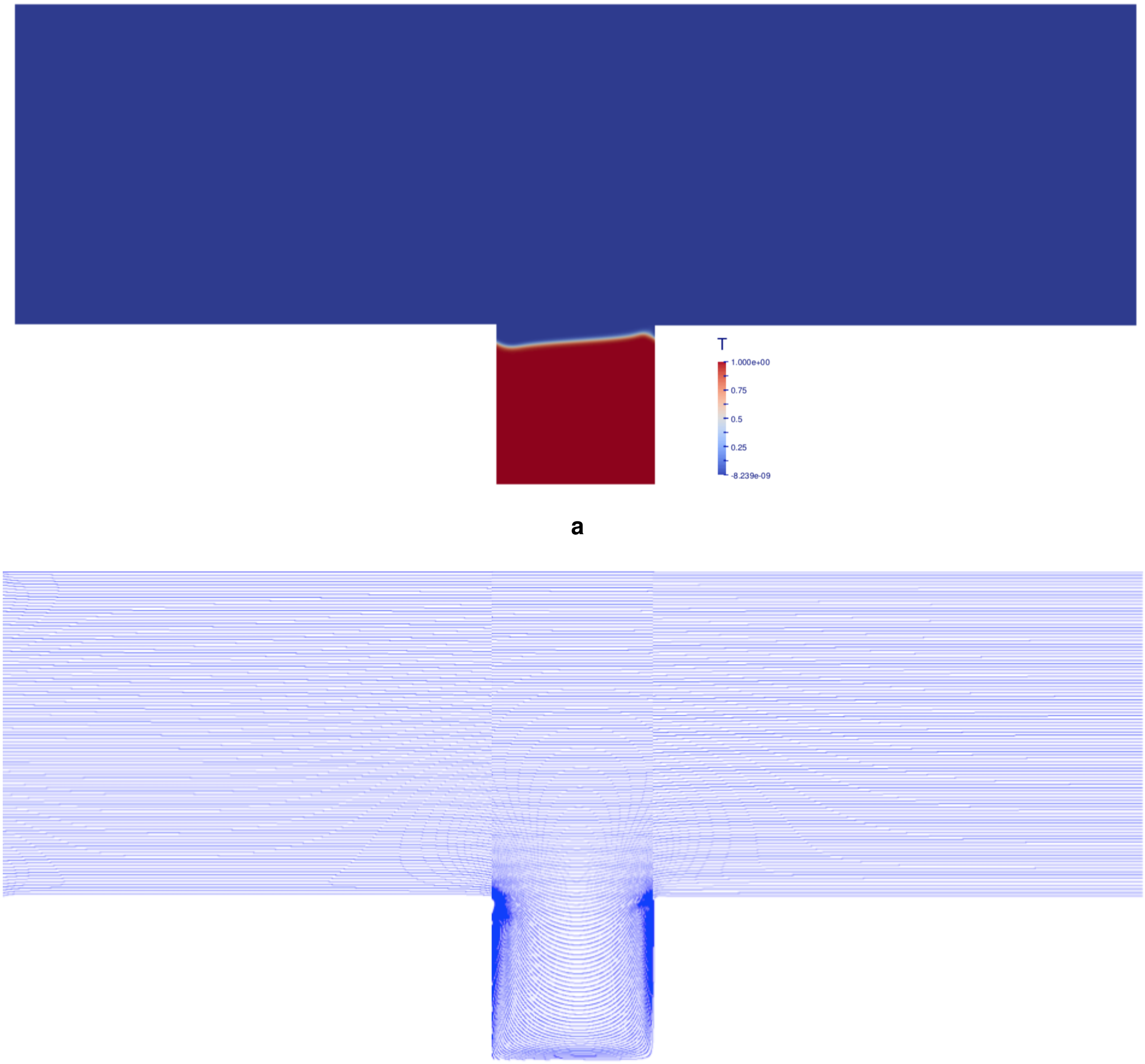

a

b

Figure 6.7: Interfaces (a) and streamlines (b) at time 0.4s

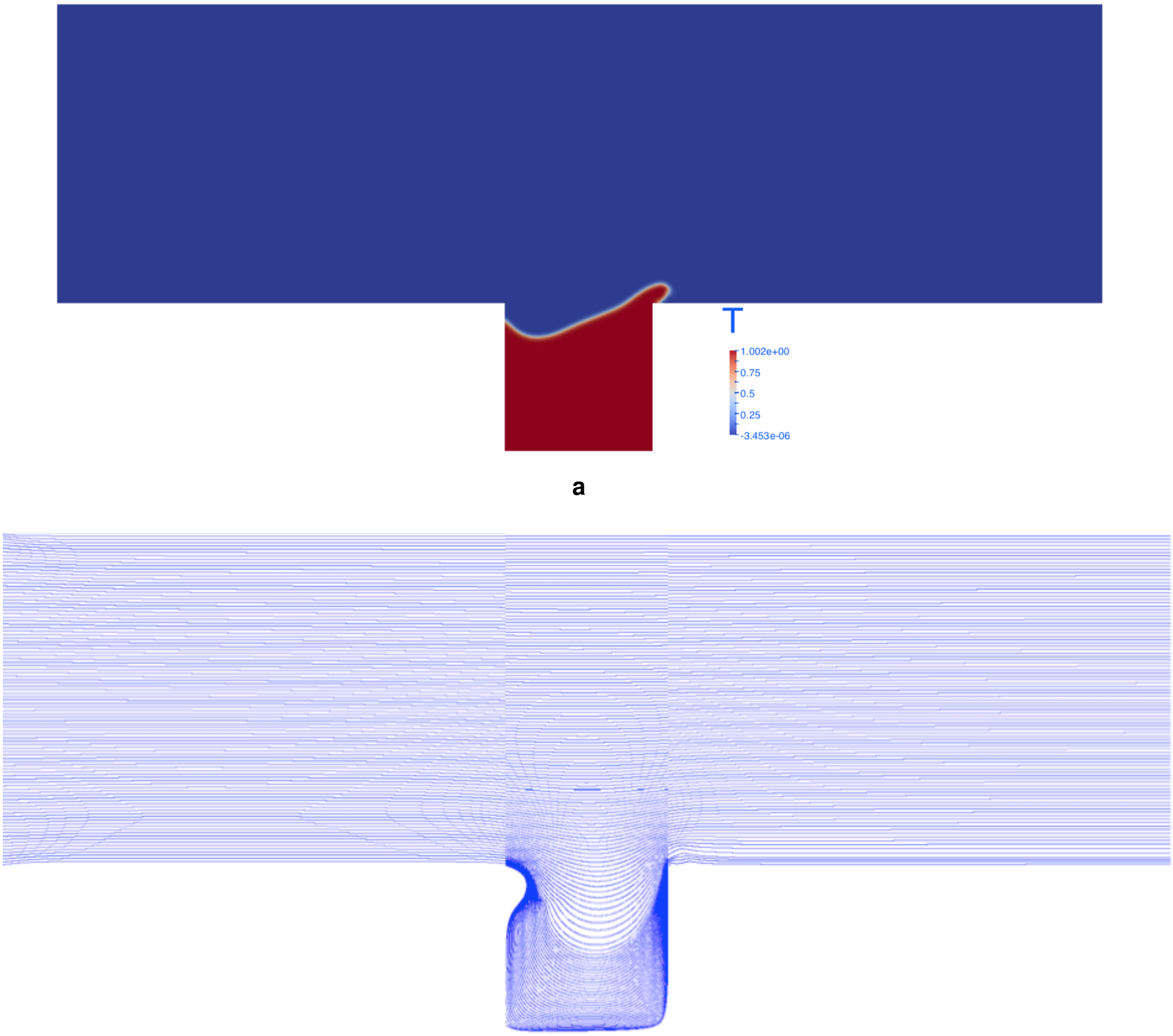

Figure 6.8: Interfaces (a) and streamlines (b) at time 1.0s

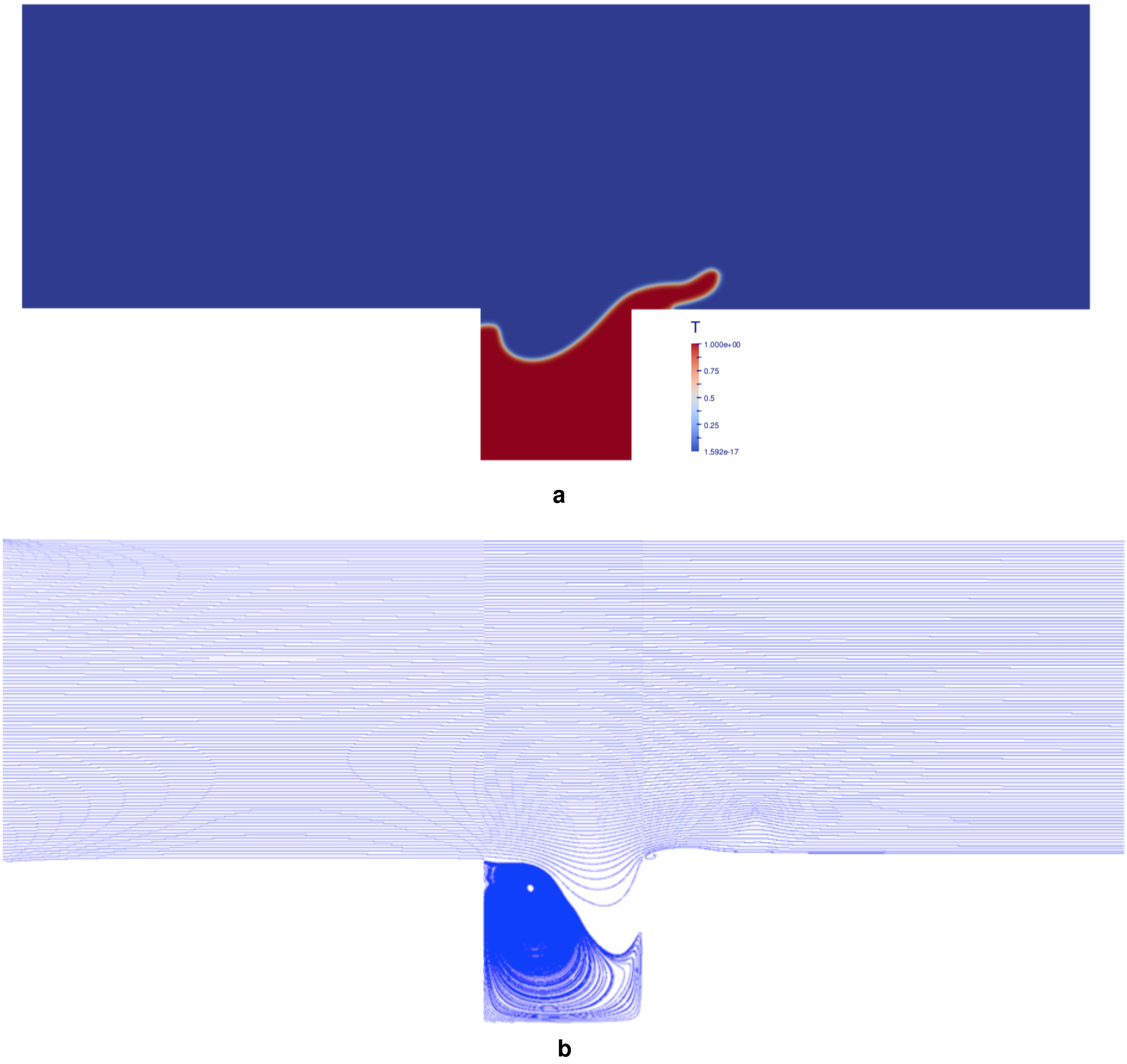

Figure 6.9: Interfaces (a) and streamlines (b) at time 2.0s

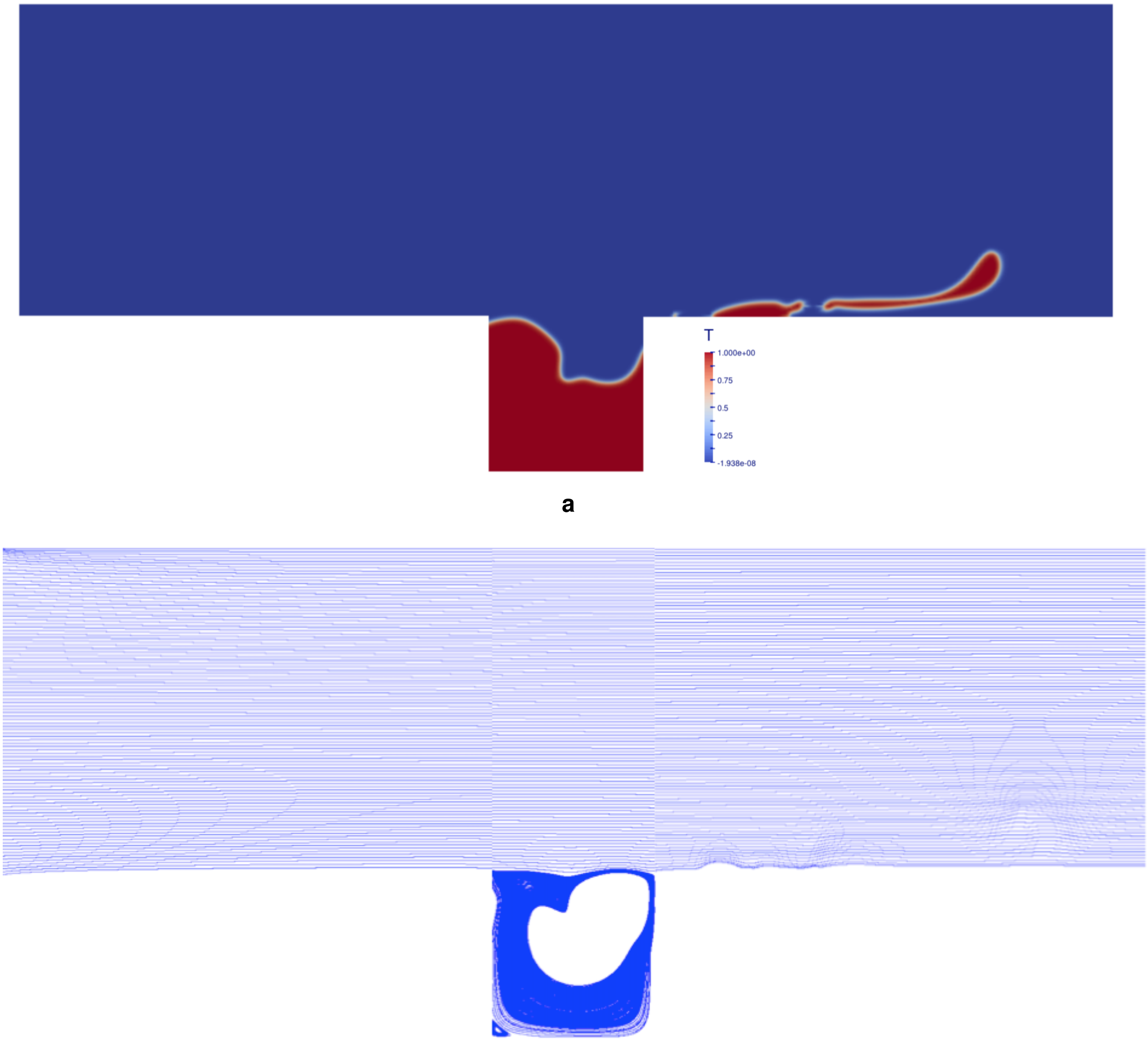

a

b

Figure 6.10: Interfaces 4.0s (a) and streamlines (b) at time 4.0s

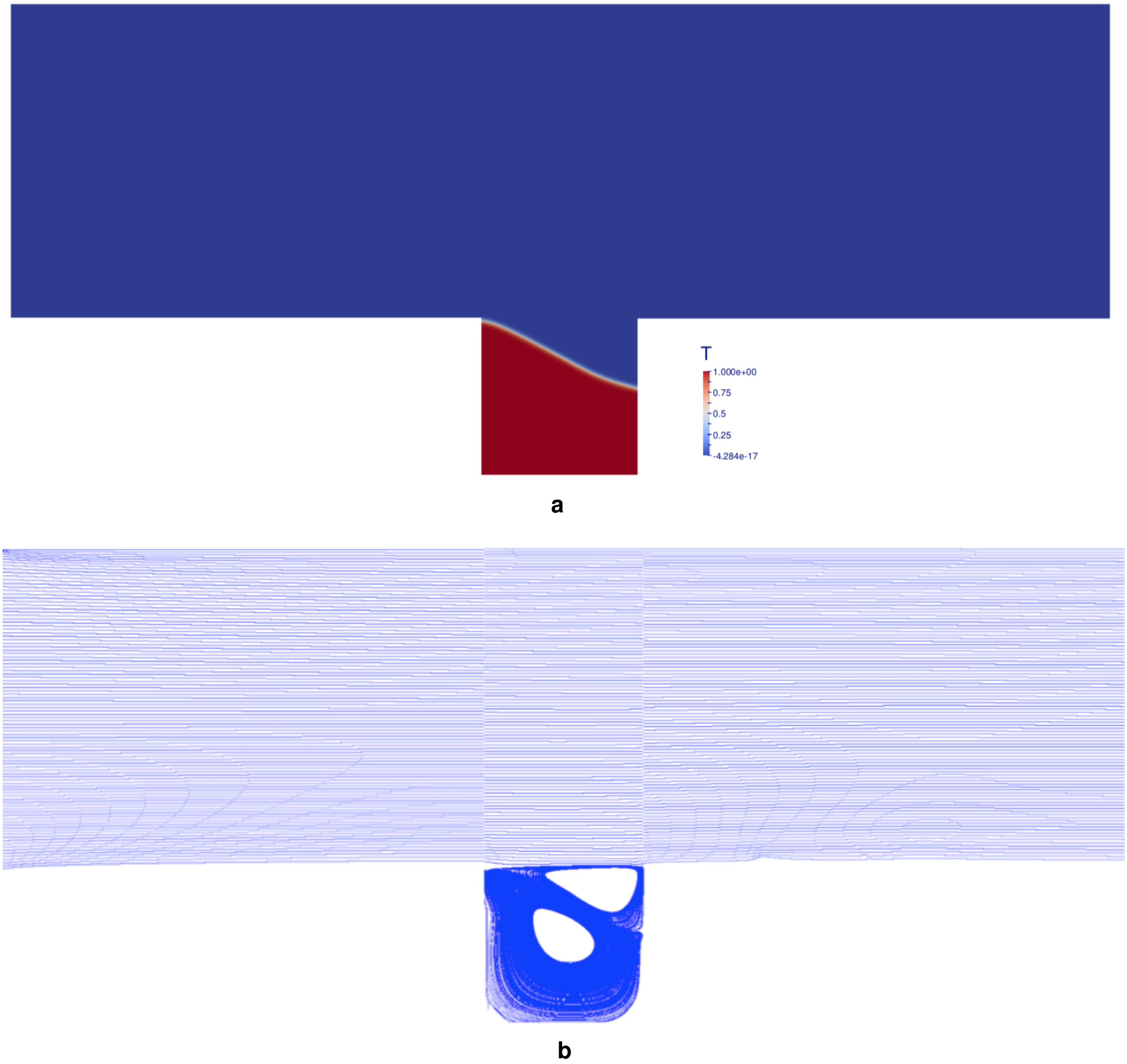

Figure 6.11: Interfaces (a) and streamlines (b) at time 20.0s

Next, the second case with $\sigma = 0.005$ and $We = 200$ will be discussed. Furthermore, the time evolution of the interface and the streamlines in the cavity are shown.

Figure (6.12) shows results similar to the case in which the Weber number is 100 at $t = 0.4s$ after the initiation of the flow. At this time step, no NAPL has been pushed out of the cavity by the overflow, and no obvious difference can be observed neither from the interface orientation nor the streamlines.

In figure (6.13), the results are illustrated after $t = 2s$. The interface indicates that the vortex close to the leading corner of the cavity is stronger than that in figure (6.9), since more fluid splashes further out of the cavity and goes farther in the channel. Mass starts to be pushed out of the cavity at the trailing corner.As can be also seen, several streamlines from the overflow, which produce the splash of fluid, enter and traverse the cavity, then exit at the trailing corner.

The results at $t = 4s$ after initiation are showed in figure (6.14). The process of mass transfer is complete, since no streamlines enter the cavity. The exiting NAPL in the channel has moved farther than that in figure (6.10). The vortex has already touched the trailing wall, but there is no strong tendency to separate into two parts as observed in figure (6.10).

Figure (6.15) shows the vortex moving backwards nearly to the center of the cavity, after reaching the trailing edge, rather than stopping there. This is because of the convective effect from the channel part provides sufficient momentum to the vortex, which contrasts to the case where the Weber number is 100.

Figure (6.16) shows steady state results at $t = 40s$. The inclination of the interface should be larger than that in figure (6.11), since a smaller surface tension coefficient was applied. However, the left side of the interface (see figure (6.11)) has already reached the leading corner when the Weber number is 100. Three vortices have formed in the cavity in order to generate the larger inclination: the first was a clockwise rotation generated near the leading edge and is balanced by the convective effect from the channel; the second vortex is close to the trailing edge; the third vortex that rotates counter-clockwise appears at the bottom of the cavity, due to these two vortices. A part of the overflow enters the cavity resulting in a saddle point, in addition to these three vortices. The small amount of mass remaining outside the cavity can be explained by the strong effect of the first vortex. Therefore, the location of the interface is between these three vortices, producing a large inclination, because the surface tension force is not strong enough to protect the interface from the changing topology.

When the Weber number is 200, mass transfer is similar to the previous case in which the Weber number is 100. However, the behavior of the interface is quite different, due to the smaller surface tension force. Moreover, the three vortices generated in the cavity were not, as expected, within the normal two-phase cavity flow.

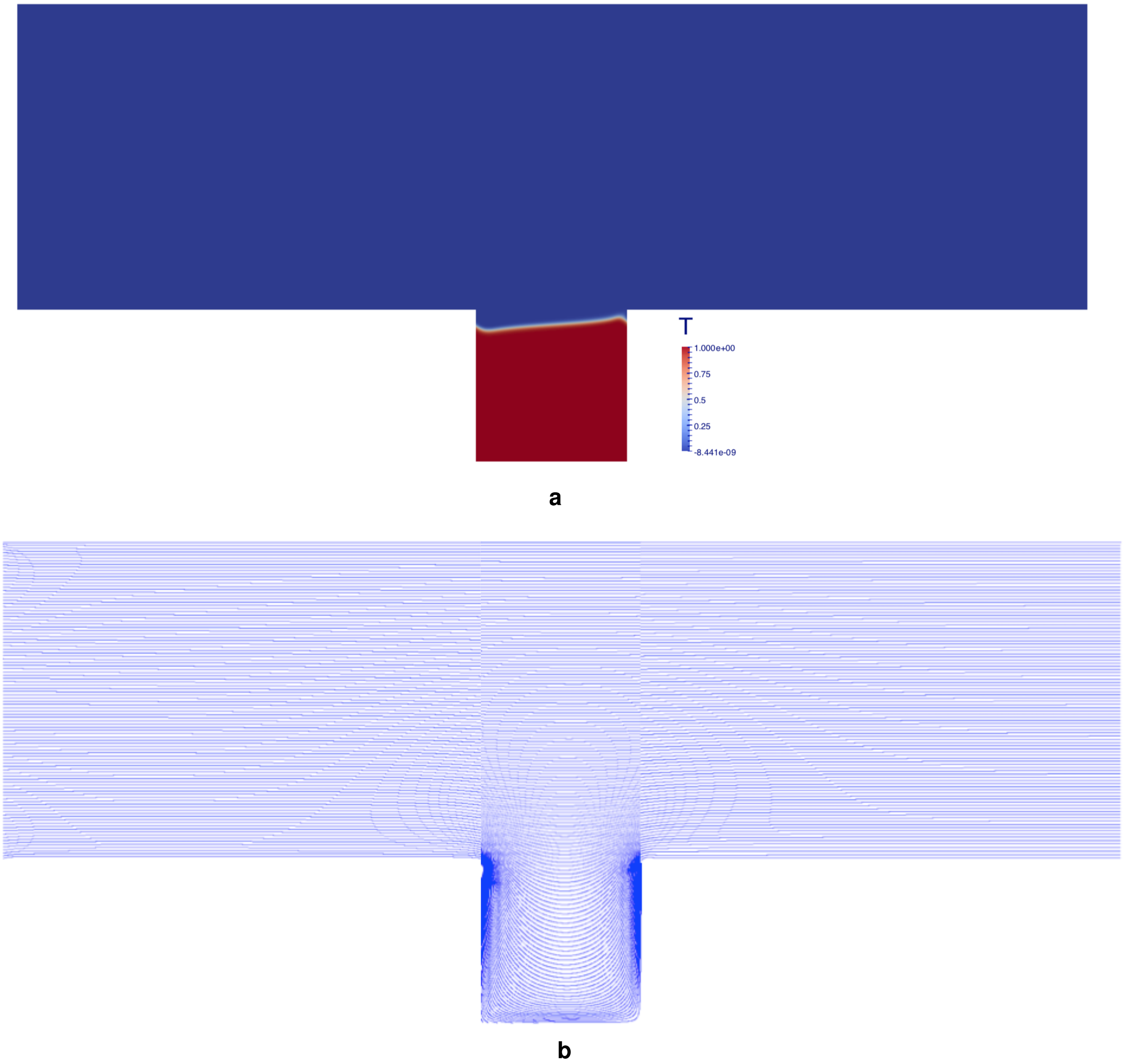

Figure 6.12: Interfaces (a) and streamlines (b) at time 0.4s

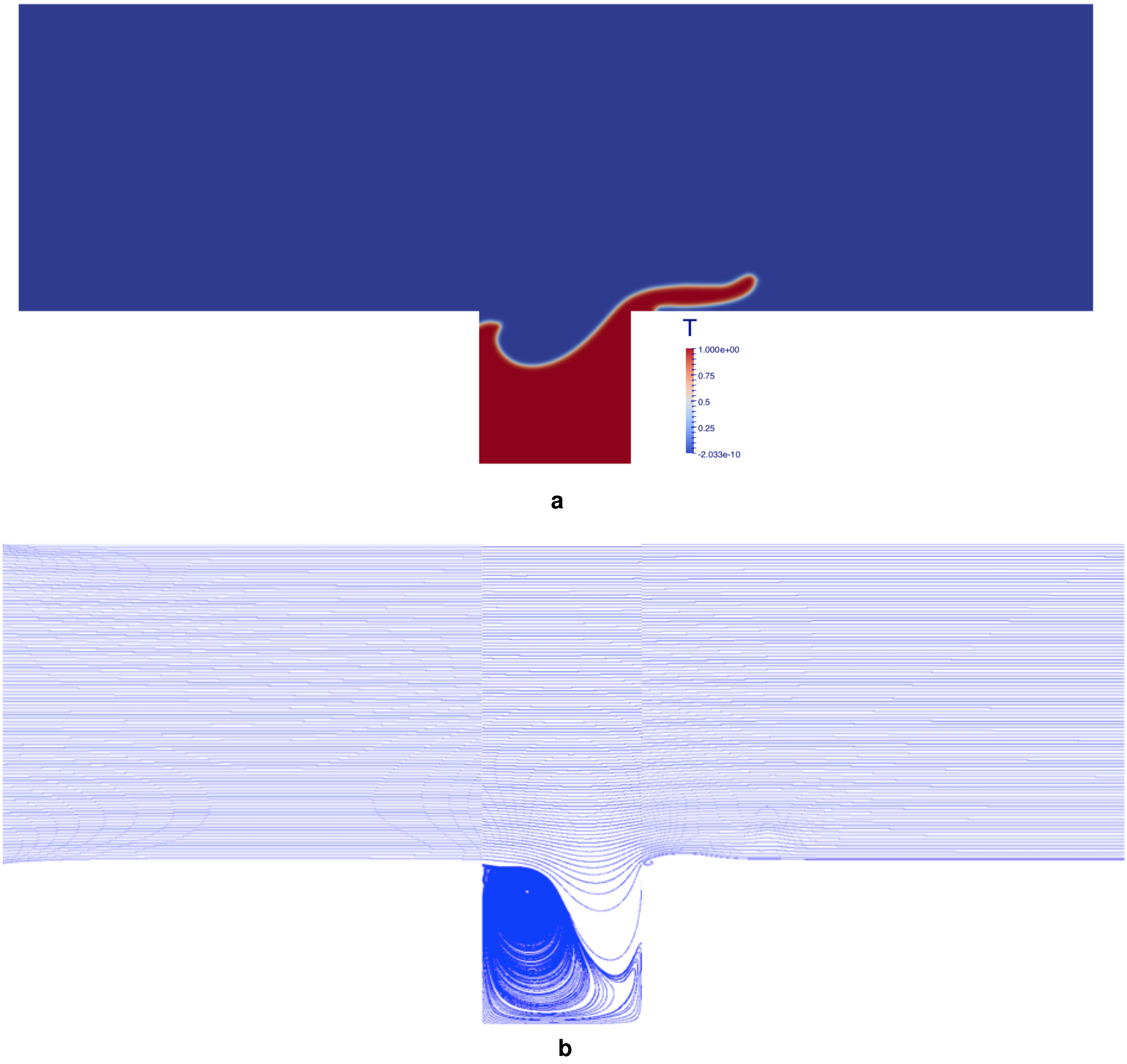

Figure 6.13: Interfaces (a) and streamlines (b) at time 2.0s

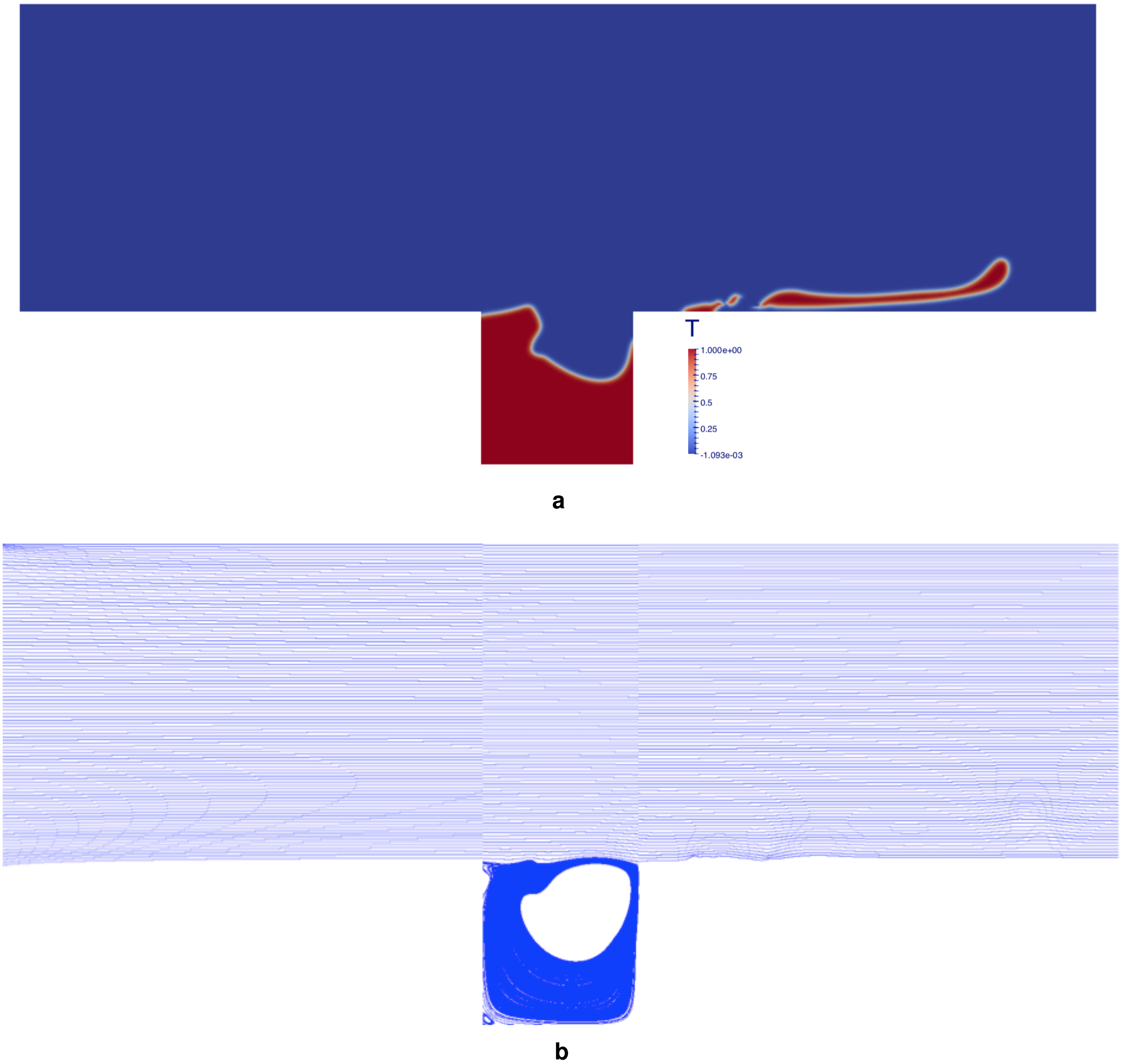

Figure 6.14: Interfaces (a) and streamlines (b) at time 4.0s

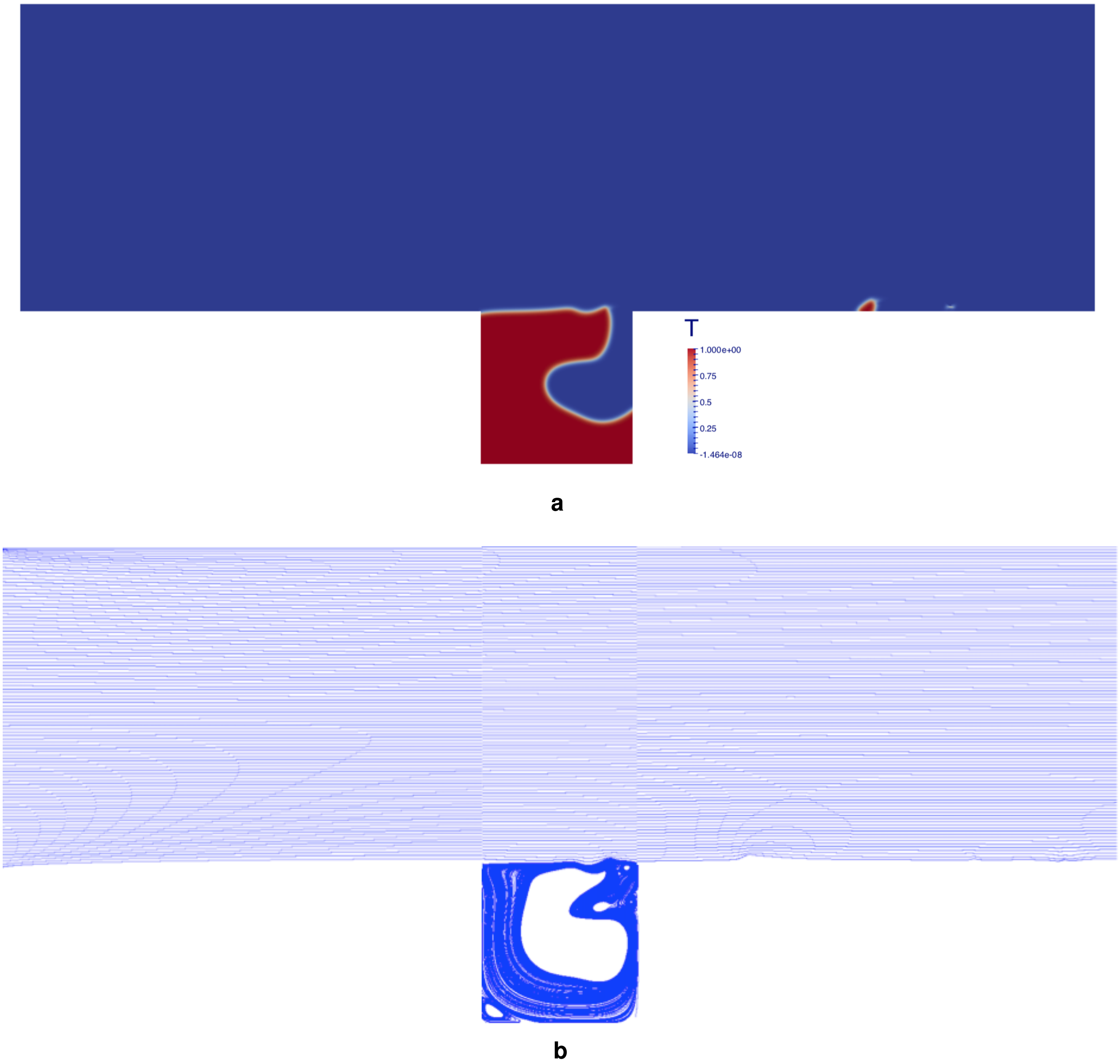

Figure 6.15: Interfaces (a) and streamlines (b) at time 9.0s

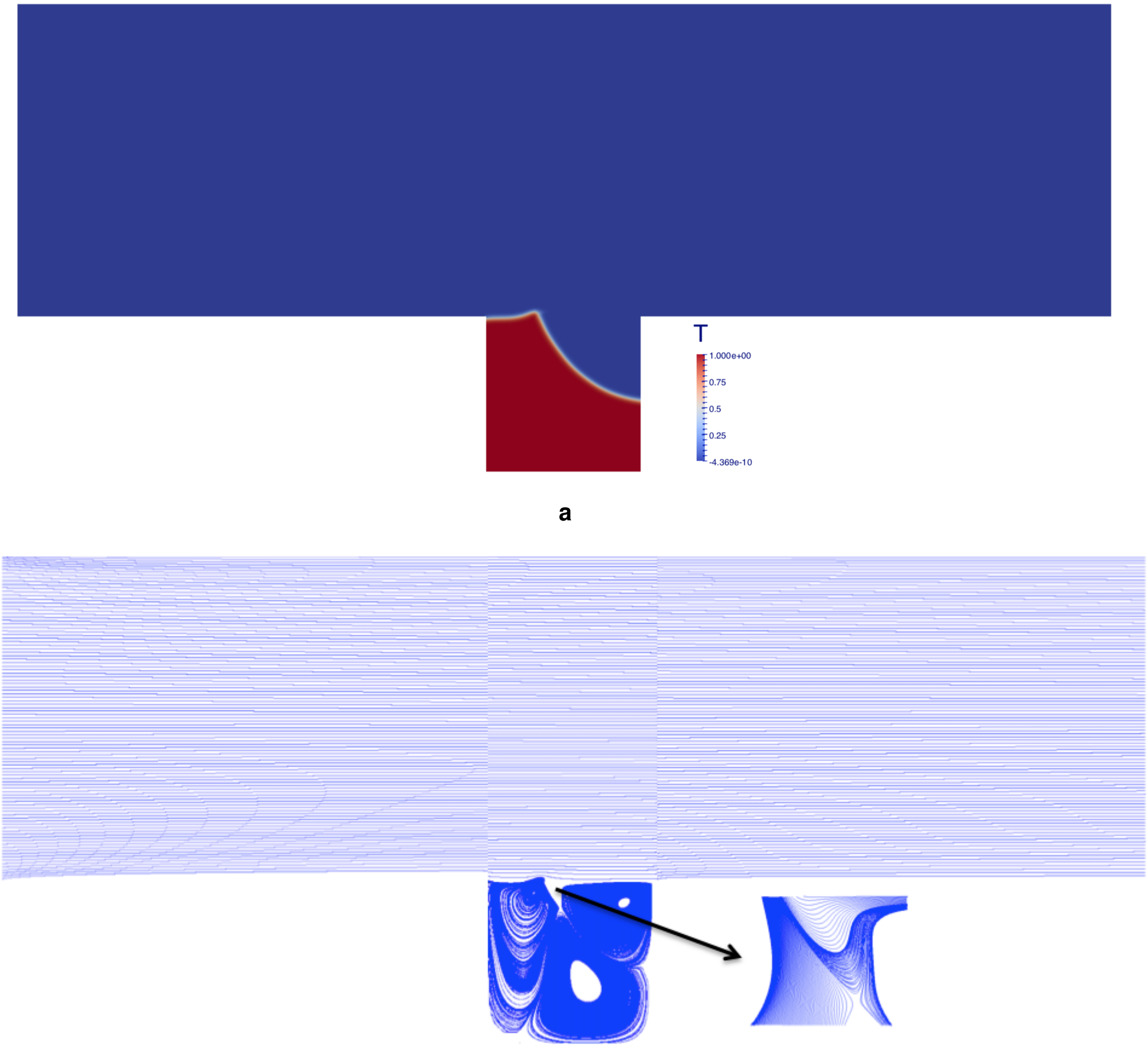

a

b

Figure 6.16: Interfaces (a) and streamlines (b) at time 40.0s

This problem is similar to the 'single phase problem' because the density ratio and the viscosity ratio are equal to one. However, the presence of the interface, influenced by the surface tension force between two immiscible flows, plays an important role in the two-phase model. This presence is the essential difference between the single-phase and multiphase flows. The Weber number can be regarded as the dimensionless form of the surface tension force, which is the ratio of the convective effect to the surface tension force. If the value of the surface tension coefficient is quite small, this indicates that the convective effect is starting to dominate. As a result, the behavior of the interface can be easily influenced by the convective overflow. In contrast, if the surface tension coefficient is relatively large, the interface will be well protected from changing its topology. Therefore, the Weber number can be treated as a force to protect the interface and prevent its shape changing. This conclusion can also be observed in figure (6.17) - figure (6.19).

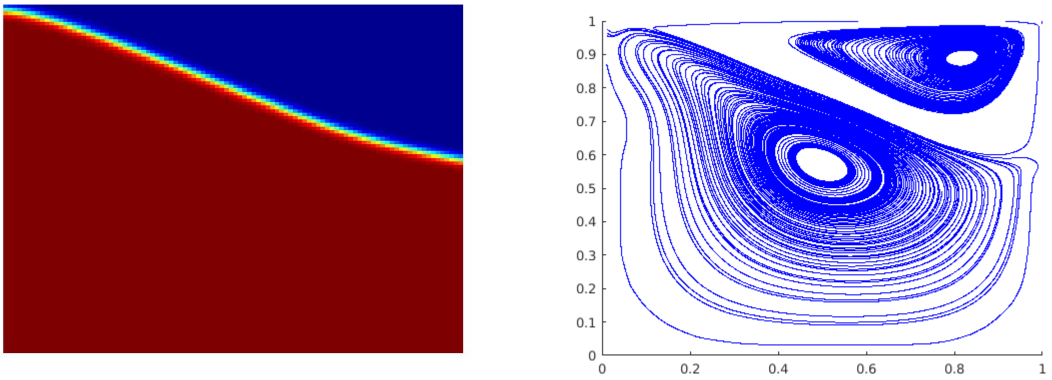

a **b**

Figure 6.17: Interface (a) and streamlines (b) after steady state ($We = 100$)

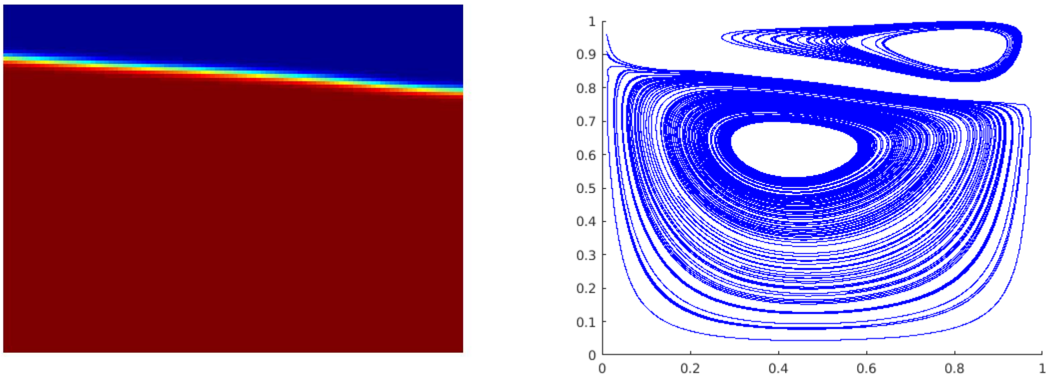

a **b**

Figure 6.18: Interface (a) and streamlines (b) after steady state ($We = 25$)

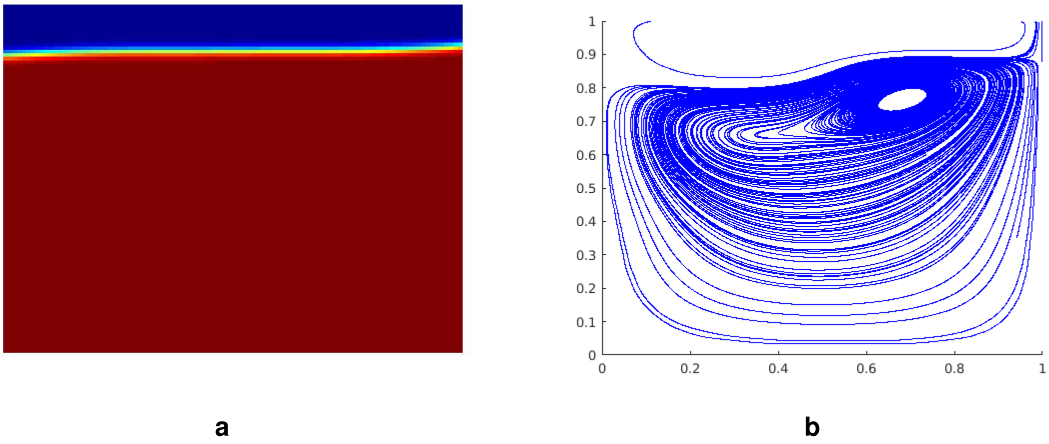

Figure 6.19: Interface (a) and streamlines (b) after steady state ($We = 12.5$)

As introduced above, the original interface is initially defined as a straight line in the cavity. In figures (6.17) and (6.18), after the steady state, the interface becomes an inclined line. However, as the surface tension force increases (We number decreases), the angle of inclination of the interface becomes smaller. For the larger surface tension force shown in figure (6.19), the interface remains straight as can be observed in the original state. The location of the two vortices has also been changed due to the topology of the interface when comparing the streamline figures.

6.5 Influencing factors of mass transfer rate for cavity model

In this section, different flow conditions, such as different We number, density ratio and time scale ratio, are investigated to estimate the mass transfer rate from the cavity.

6.5.1 Effect of the flow acceleration

In this test, the cavity Reynolds number is set to $Re = 1000$ and the Weber number is set to $We = 100$. Both the viscosity ratio and the density ratio are set to one. Figure (6.20) demonstrates the effect of the acceleration rate of the flow, expressed by the dimensionless time scale ratio τ . If τ is large, the flow attains its steady state very slowly and is unable to push the mass out. Apparently, if τ is small enough, a strong shear layer is generated between the overflow and the cavity. The flow obtains a large acceleration and is able to push some mass out of the cavity. Furthermore, due to the different accelerations, the starting time of the mass transfer also varies. In the following part, $\tau = 1$ is used for all simulations.

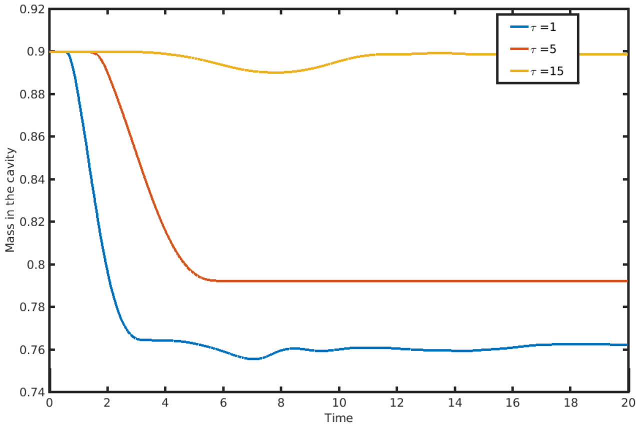

Figure 6.20: Mass transfer with various time scale ratios

6.5.2 Effect of the surface tension

In section (6.4), we can conclude that the surface tension force can influence the behavior of the interface (i.e., different surface tension forces result in different inclinations of the interface). Moreover, we can also conclude that the surface tension force qualitatively impact the mass transfer rate. In this part, the mass transfer rate impacted by the surface tension force will be examined quantitatively.

The surface tension has a strong effect on the flushing of the cavity. As mentioned above, the surface tension effect is quantified by the non-dimensional Weber number. Small surface tension effect σ results in a large Weber number. In this case, we still set the density ratio and viscosity ratio to unity. The cavity Reynolds number is 1000. From figure (6.21), at small surface tension, the mass transfer can be considerably larger than at larger surface tension. A surface tension force can protect the interface and inhibit the mass transfer if the Weber number is small. Moreover, more time is needed to achieve the steady state when the smaller Weber number is employed.

6.5.3 Effect of the Reynolds number

The mass transfer influenced by the Reynolds number is investigated. The density of both fluids is set to $\rho = 1$, and the Weber number is 100. By changing the viscosity μ of both fluids, the cavity Reynolds number can be varied. However, we still keep the viscosity ratio at one. The mass transfer mainly depends on the convective effects. A small Reynolds number leads to the weak convective effect. And, thus the number of mass exits from the cavity is reduced. In figure (6.22), the results are, as expected, that the higher the Reynolds number applied, the more mass that can be pushed out of the cavity.

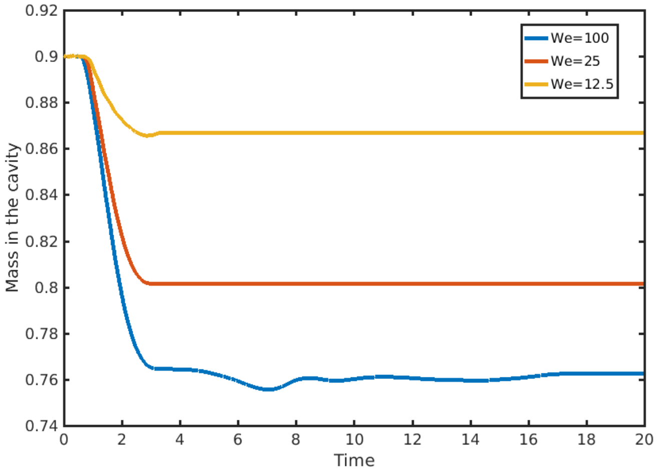

Figure 6.21: Mass transfer with various We numbers

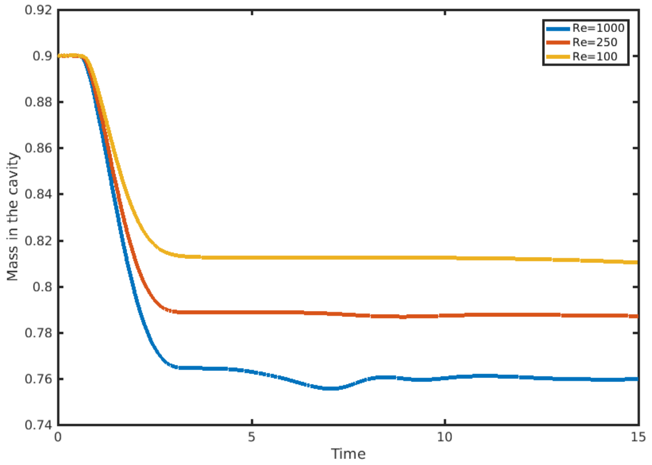

Figure 6.22: Mass transfer with various Re numbers

6.5.4 Effect of the density ratio

The density ratio is indicated as $\frac{\rho_1}{\rho_2}$. The other parameters are set similarly to the previous cases. The strong convective effects caused by the large density can increase the mass transfer rate. If the density ratio is greater than one, the convective effect from the overflow is stronger than that in the cavity, resulting in larger momentum to push the mass out of the cavity, while a smaller density ratio decreases the mass transfer rate (see figure (6.23)).

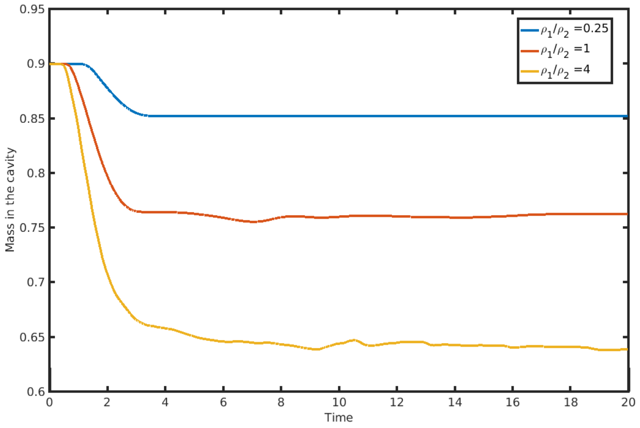

Figure 6.23: Mass transfer with various density ratios

6.5.5 Effect of the viscosity ratio

Next, different viscosity ratios are taken into account with $We = 100$ and $Re = 1000$; the density ratio remains one. The viscosity ratio is expressed as $\frac{\mu_1}{\mu_2}$. Because the diffusive effect has little impact on the mass transportation from the cavity, the results in figure (6.24) do not differ significantly after reaching the steady state, consistent with the theory discussed previously.

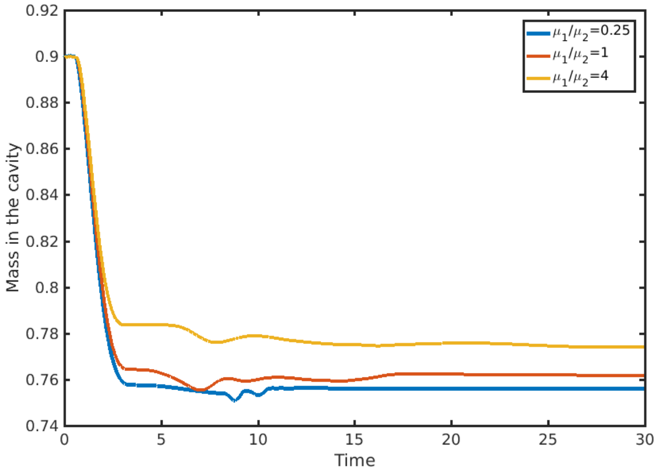

Figure 6.24: Mass transfer with various viscosity ratios

6.5.6 Effect of the gravitational force

The gravitational force is considered in figure (6.25). In this test, the bulk Richardson number is used to characterize the buoyancy effect,

$$Ri = \frac{\rho_2 - \rho_1}{\rho_1} gL^2/u_0^2 \tag{6.4}$$

If the Richardson number is much smaller than unity, buoyancy is not significant in the flow; however if it is greater than unity, buoyancy is dominant. Three simulations with initial Richardson number $Ri = 0.0$, 0.245, and 0.49 are performed. The results indicate that the transport mechanism is very different in the neutrally buoyant case ($Ri = 0.0$) compared to the negatively buoyant ones ($Ri = 0.245$ and $Ri = 0.49$). The neutrally buoyant case is more efficient than the other two.

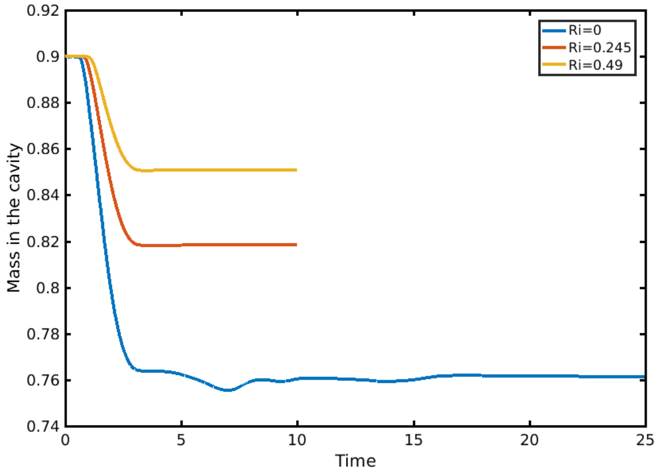

Figure 6.25: Mass transfer with various Ri numbers

6.5.7 Sensitive analysis

The sensitive analysis of mass in the cavity at the steady state with various Weber numbers, Reynolds numbers and time scale ratios are discussed in this section.

In figure (6.26), in terms of strong acceleration, a small increment of the Weber number can result in large mass transportation if the Reynolds number is high enough ($Re = 1000$). However, the improvement in the mass transfer rate is quite small when increasing the Reynolds number and the Weber number with a small value and when the Reynolds number is less than 1000. Continuously increasing the Weber number and the Reynolds number, the number of the mass in the cavity reduces strongly. The mass transfer rate seems to be sensitive to the Weber number and the Reynolds number. At most around 15.3 percentage of the mass can be pushed out of cavity.

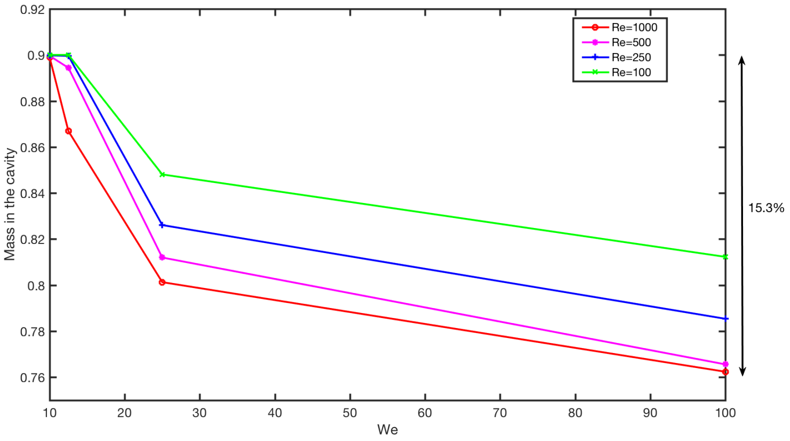

Figure 6.26: $\tau = 1$

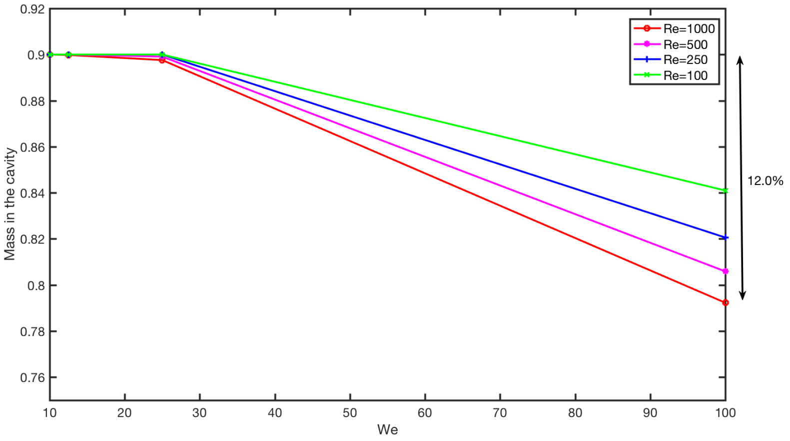

Figure 6.27: $\tau = 5$

Next, the results with time scale ratio $\tau = 5$ are investigated (see in figure (6.27)). Nearly no mass can exit the cavity when the Weber number is less than 25. Meanwhile, increasing the Reynolds number has little affect on the mass transfer. Only when the Reynolds number and the Weber number are sufficiently large, can the mass transported out of cavity be observed. Therefore, the mass transfer rate is not sensitive to the Reynolds number when the Weber number is small. At most 12% of the mass can exit the cavity.

Finally, the results with weak acceleration are shown in figure (6.28). Therefore, the mass in the cavity is almost the same as the original state even after reaching the steady state. The amount of the mass transported out of the cavity is negligible, since at most only 0.42% of the mass can leave the cavity. Thus, the mass transfer rate is not sensitive neither to the Reynolds number nor the Weber number if the time scale ratio is very large. Furthermore, after comparing these three figures, we also conclude that the mass transfer rate is strongly sensitive to the time scale ratio.

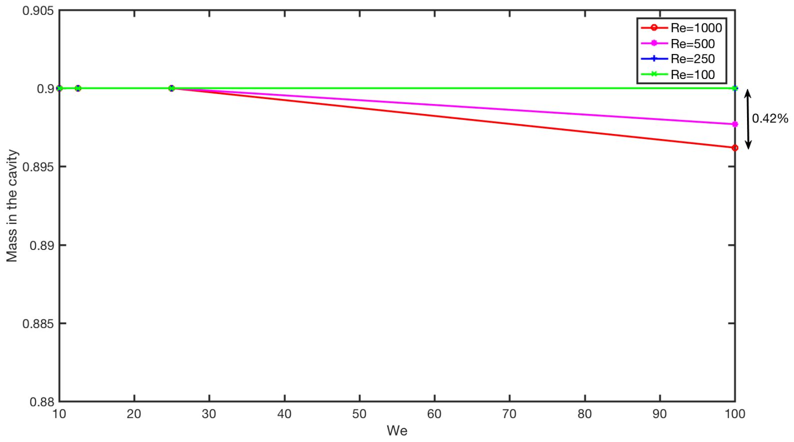

Figure 6.28: $\tau = 15$

In the end, we conclude that the dimensionless time scale ratio τ is the most important parameter concerning the mass transfer rate. If the acceleration is too low, then the interface cannot be deformed. Furthermore, the Weber number is the most significant factor for the behavior of the interface. For different Weber numbers, we can obtain various inclinations of the interface.

7 Application 2: Mass transfer with the Marangoni effect

Mass transfer and velocity fields influenced by the Marangoni effect are investigated in this chapter. The Marangoni effect can be caused by a concentration or a temperature gradient; however, in our simulation we only focus on the concentration gradient. The numerical results indicate that the Marangoni flow creates a shear stress at the interface which results in fluid motion along the interface rather than the parasitic currents occurring in the flow without the Marangoni effect. This behavior enhances the mass transfer rate. Furthermore, the dominance of the Marangoni flow influences the velocity field near the interface until the mass transfer process is completed (i.e. the velocity field converges into the parasitic currents).

7.1 Objectives

Residual NAPLs trapped in the soil are a long-term threat to drinking water supplies. Thus, the mass transfer process of the NAPLs at the pore and pore network scales in multiphase flows has received increasing attention recently. The Marangoni convection may take place, caused by the concentration gradient near the interface, which increases the complexities of the process. Thus, several experiments have been conducted to investigate the Marangoni convection by our academic partner Carina Wismeth. In her experiments, some rolling particles are observed along the interface. Moreover, for a octanol-water system, the velocity field near the interface decays from $1100\mu m/s$ to $0\mu m/s$ due to the fact that the concentration of octanol close to the interface is fully saturated in the water phase, which may last several days. The Marangoni effect is expected to explain this phenomenon. Therefore, the numerical simulation of the Marangoni effect is employed, since it is easier to analyze the results with and without the Marangoni effect numerically. Additionally, many studies have been carried out to investigate mass transfer as impacted by the Marangoni effect (Mao & Chen, 2004) (Wang *et al.*, 2008). However, the mass transfer models of these studies are mainly based on sharp interface methods, rather than continuous interface methods. Therefore, we focus on the new mass transfer model based on the CLS method (see section (4.3)) to investigate the mass transfer process with the Marangoni effect.

7.2 Model set-up

The experimental set up is depicted in figure (7.1). It is difficult to measure the contact angle at the top and bottom walls experimentally and model the stair geometry numerically. Thus, the numerical model is simplified and set up as shown in figure (7.2). The interface is a segment of a circle whose center is located at $(1.85, -0.1)$ with a radius of 1.15. The top and bottom walls are treated as no-slip surfaces, and the left and right are regarded as slip surfaces for the velocity fields. All the surfaces are implemented with the Neumann boundary conditions for the scalar fields (level set function and concentration field). In the following, subscript 1 indicates the fluid on the left side of the interface (e.g. octanol), and 2 the fluid on the right side of the interface (e.g. water). The mass transfer from fluid 1 to fluid 2 is measured without the external mass resistance. Additionally, the concentration is sharply initialized as:

$$c_1 = 1 \quad \text{at t=0 (fluid 1)} \tag{7.1a}$$
$$c_2 = 0 \quad \text{at t=0 (fluid 2).} \tag{7.1b}$$

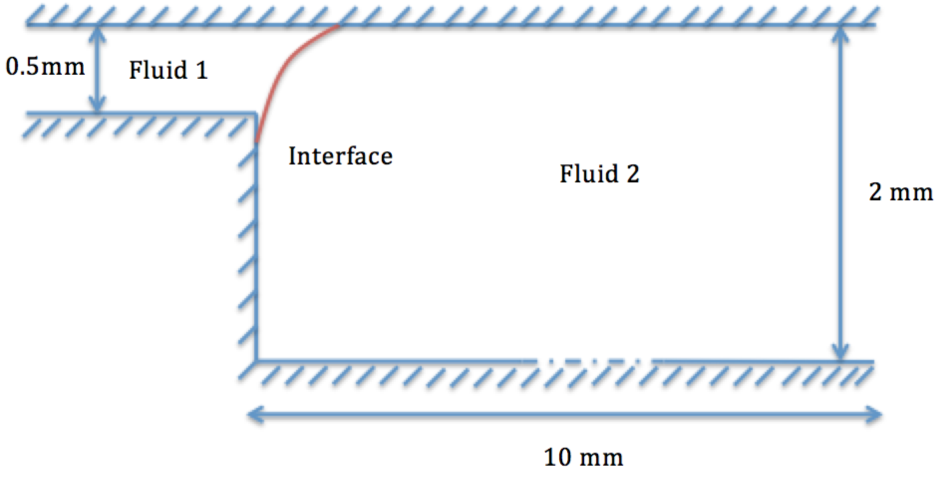

Figure 7.1: The experimental model of mass transfer with the Marangoni effect

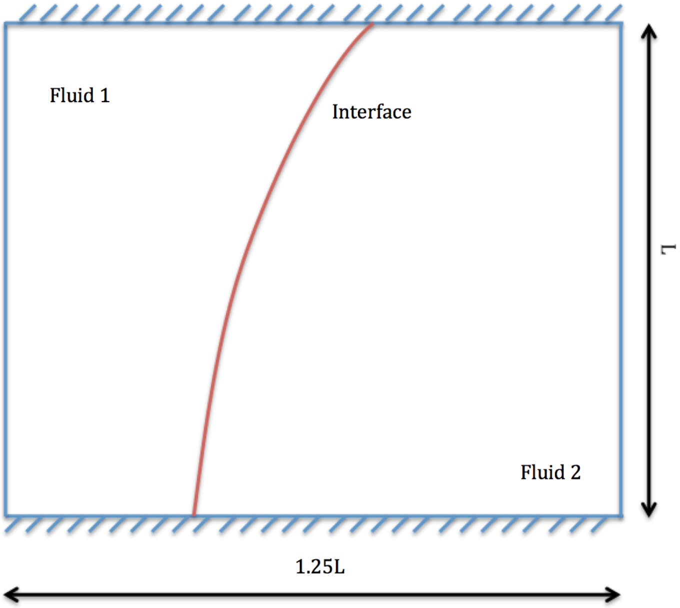

Figure 7.2: The numerical model of mass transfer with the Marangoni effect

The Marangoni number, Schmidt number, and Reynolds number, defined by the properties of the fluid 2, are used to characterize the mass transfer process influenced by the Marangoni effect,

$$Ma = -\frac{L\Delta\sigma}{\mu D}, \tag{7.2}$$

and

$$Sc = \frac{\nu}{D} = \frac{\mu}{\rho D}, \tag{7.3}$$

where $\Delta\sigma = \frac{\partial\sigma}{\partial c}\Delta c = \gamma\sigma_0\Delta c$ (see equation (4.16)), γ can be treated as a coefficient of the surface tension gradient, and Δc is the maximum concentration difference across the interface. In the CLS method, Δc is always equal to one.

Based on this, an equivalent Reynolds number can be derived as:

$$Re = Ma/Sc = \frac{\Delta\sigma L}{\rho\nu^2}. \tag{7.4}$$

The Reynolds number can be regarded as proportional to the tangential stress $\Delta\sigma L$ divided by the viscous stress $\rho\nu^2$, rather than the ratio of inertial forces to viscous forces. Apparently, only two of the three numbers are independent.

The properties of water and octanol are listed in table (7.1). Thus, the Schmidt number in the experiment can be obtained, $Sc = 1282$. However, due to the uncertainty of the coefficient of the surface tension gradient γ, since γ is assumed as a constant rather than a concentration dependent variable in the real situation, it is difficult to measure γ as same as in the experiment. Meanwhile, γ also needs to be set to fulfill the stable conditions of the numerical scheme. Hence, the Marangoni number has to be analyzed qualitatively to investigate the impacts on the flow.

	ρ $[kg/m^3]$	μ $[kg/m/s]$	D $[m^2/s]$	σ $[mN/m]$
$Water$	1000	0.001	–	–
$Octanol$	827	0.00736	$0.78 \mathrm{x} 10^{-9}$	852

Table 7.1: The properties of water and octanol

7.3 Velocity fields

7.3.1 Mechanisms

In order to understand the definition of the Marangoni effect and its influences on the concentration field, the mechanisms of the Marangoni effect, caused by the concentration gradient, are discussed in this section.

In our case, the parameters are set from table (7.1), except γ is -0.2 and the surface tension coefficient is 0.0001. The smaller surface tension coefficient is applied to reduce the impacts of the parasitic currents, which will be discussed in detail later. In such a way, the Schmidt number is set to $Sc = 1282$ and the Marangoni number is also $Ma = 1282$.

Figure (7.3) a) indicates the velocity field without the Marangoni effect. We can only observe the parasitic currents occurring along the interface. The occurrence of parasitic currents is caused by the inaccuracy in curvature estimations and the imbalance of the surface tension and pressure gradient forces (Francois *et al.*, 2006). Figure (7.3) b) shows the expected concentration field without the Marangoni effect. The isolines of the concentration in the water phase should be parallel to the interface, and the thickness between any two isolines should be uniform since the mass transfer is isotropic.

Figure (7.4) a) shows the velocity field influenced by the Marangoni effect. Due to the inverse relationship between the surface tension force and the concentration, the region of higher concentration has the lower surface tension force and the region of lower concentration has the higher surface tension force. Because of the gradient of the surface tension, an unbalanced force distribution is created at the interface, which creates a shear stress that leads to the fluid moving tangentially along the interface. Therefore, within the thickness of the interface, the tangential force dominates the viscous force. Thus, the region of high surface tension at the top wall pulls the region of low surface tension at the bottom wall along the interface. This phenomenon gives rise to the Marangoni convection. Because of the Marangoni effect, the expected concentration field is shown in figure (7.4) b). The flow moves upwards along the interface, such that the concentration accumulated at the top wall is more than that at the bottom wall. Therefore, the distance between two isolines at the top wall is expected to be greater than that at the bottom wall. In the following section, simulations are conducted to verify our expectations (see section (7.4)).

7.3.2 Influencing factors of the velocity field

In this section, different parameters, such as different time periods, areas and the Marangoni numbers, are investigated to estimate the velocity field.

Effect of the time period

In this section, the same parameters are applied as in table (7.1). In order to distinguish the flow with and without the Marangoni effect, and fulfill the stable conditions numerically, γ is set to -0.003. Figures (7.5) a) and b) show the velocity field and the vortex influenced by the Marangoni effect for various time periods. In figure (7.5) a), the flow moves upwards and tangentially to the interface. However, due to the short time period, the scale of the vortex is smaller than that in figure (7.5) b), where the vortex rotates through the whole part of fluid 2. This observation can be explained by the time scale $T \sim L/u$.

Effect of the coefficient of the surface tension gradient γ

The effect of the constant γ is shown in figure (7.6). The same parameters are used as in the last section, except the coefficient γ. We can observe that although various γ are applied, the maximum velocities are not much different with and without the Marangoni effect at the initial time. This is due to the strong surface tension force implemented in the numerical simulation, which results in the maximum velocity (parasitic currents) occurring at the top wall during this period (see figure (7.7) a)). This may be due to the boundary conditions and the pressure gradient at the boundaries. Furthermore, the magnitude of the velocity field is small, so that it is very sensitive to the surface tension force. Afterwards, the location of the maximum velocity transfers to the middle of the domain near the interface (see figure (7.7) b)). If the surface tension coefficient is sufficiently small, the parasitic currents can not dominate the velocity field at the top wall compared to that has a greater surface tension coefficient (see figure (7.7) c)). Additionally, the larger value of γ results in a greater maximum velocity after 25000 time steps. Therefore, the velocity field separates into three lines later on. As the mass transfer process continues, the gradient of the concentration near the interface decreases, which leads to a smaller surface tension gradient tangentially. Hence, the maximum velocity decreases and converges into the parasitic currents.

As outlined above, in order to avoid the maximum velocity field, influenced by the top wall due to the strong surface tension effect, a new set of parameters with a small surface tension

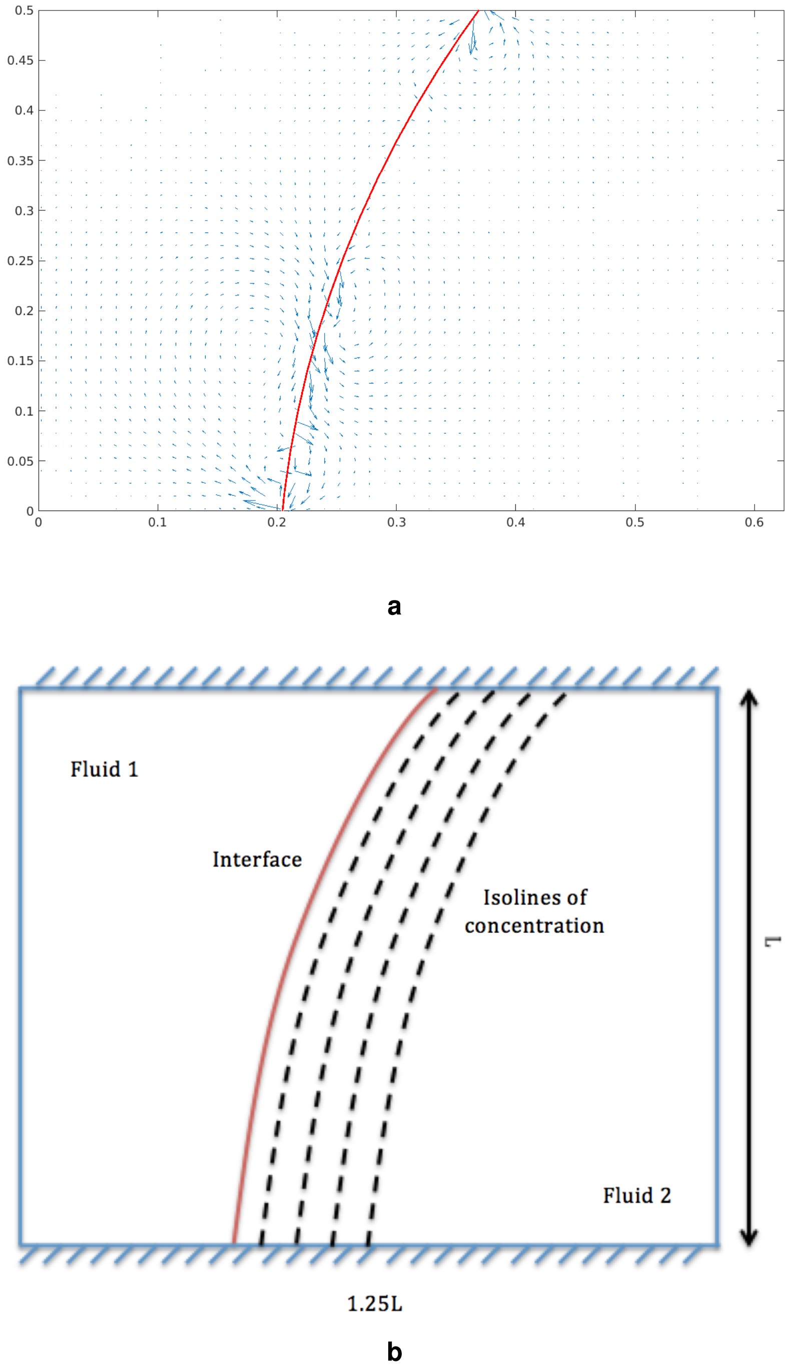

Figure 7.3: (a) Velocity field (max. velocity magnitude $\sim 10^{-5} m/s$) and (b) concentration field without the Marangoni effect at time 0.2s

coefficient is implemented with and without the Marangoni effect. Additionally, for observing the difference of the velocity field clearly, we assume that fluid 1 and fluid 2 have the same properties. In other words, all the ratios of the density field, viscosity field, and mass diffusivity field are set to one. The surface tension coefficient is 0.0001 and γ is 2, such that the Schmidt number is 12.82 and the Marangoni number is 128.2.

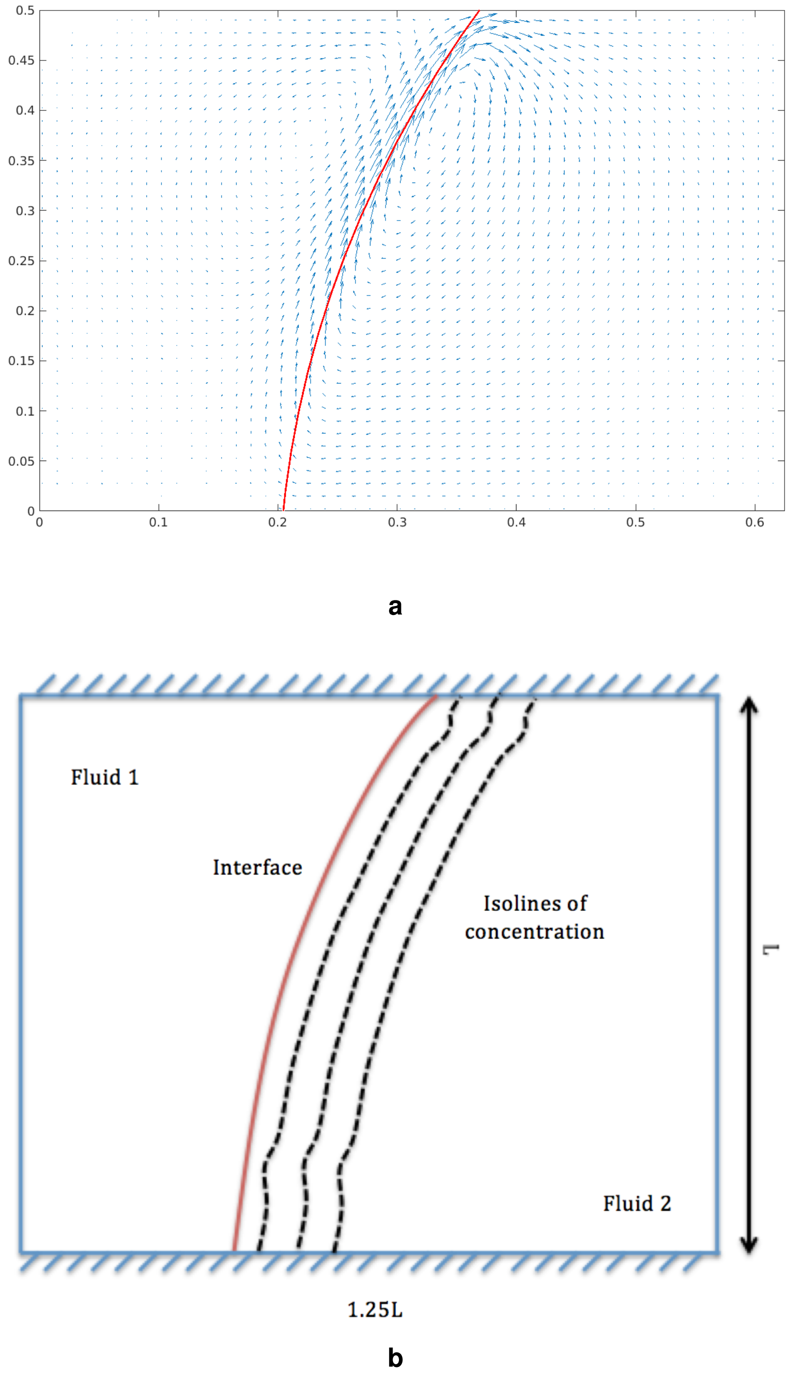

Figure 7.4: (a) Velocity field (max. velocity magnitude $\sim 10^{-4} m/s$) and (b) concentration field with the Marangoni effect at time 0.2s

Figure (7.8) clearly shows that the Marangoni effect increases the maximum velocity compared to the one without the Marangoni effect, since the tangential force dominates the flow field.

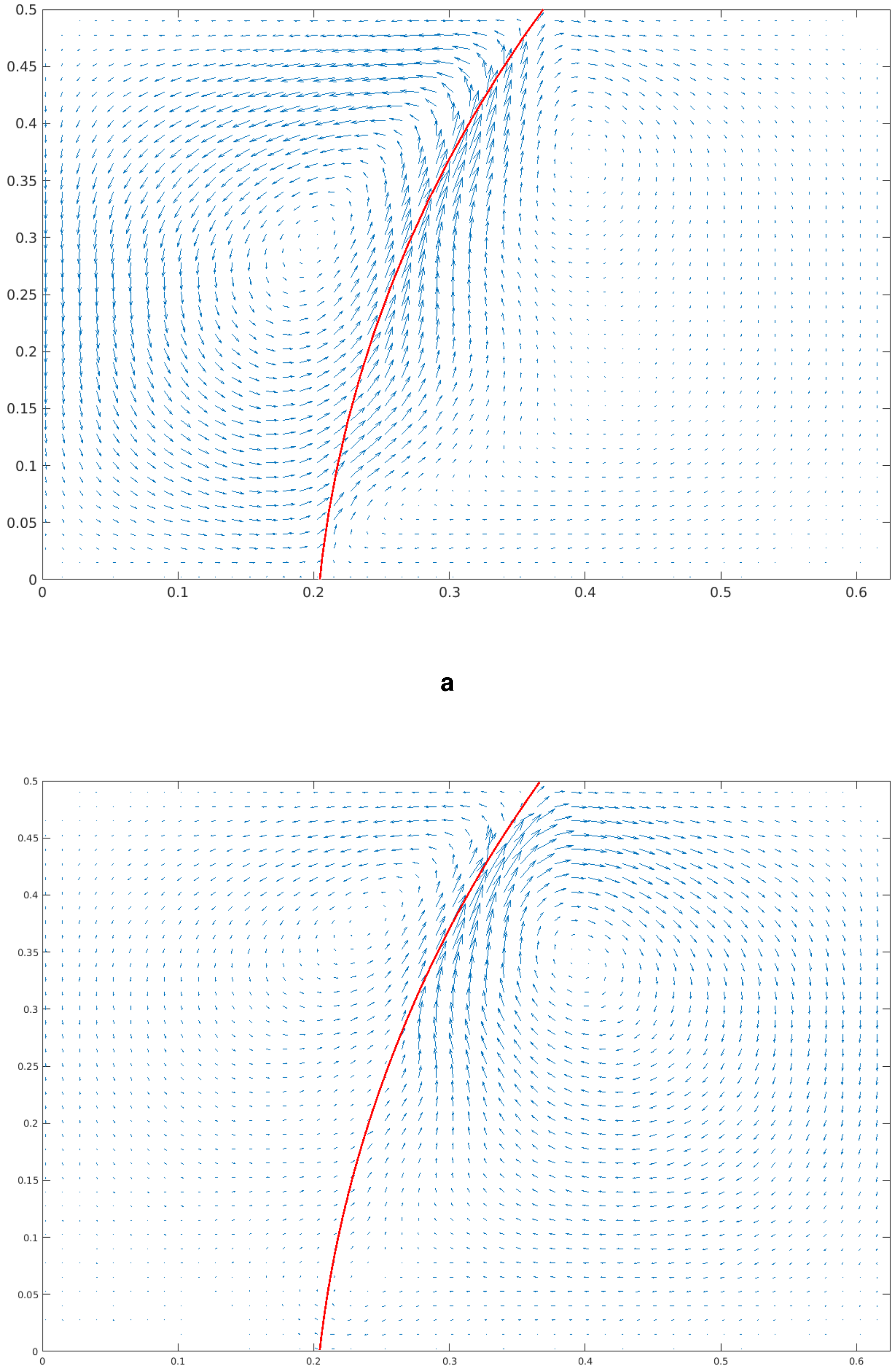

a

b

Figure 7.5: Velocity field with different time periods: (a) 8s (max. velocity magnitude $\sim 10^{-4} m/s$) and (b) 100s (max. velocity magnitude $\sim 10^{-4} m/s$)

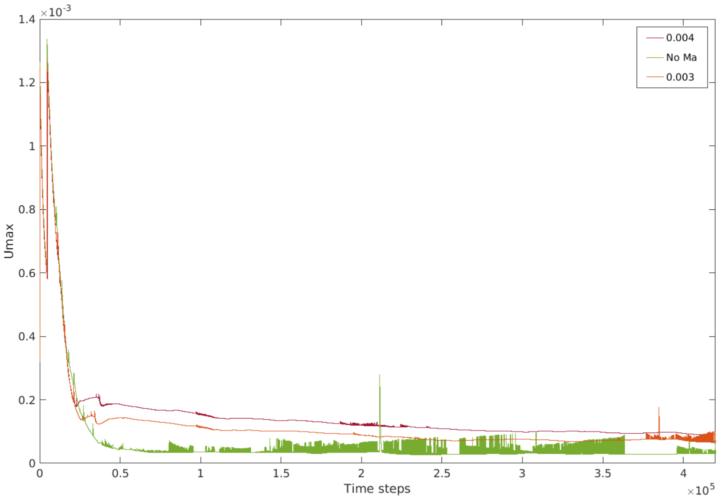

Figure 7.6: The maximum velocity with various γ

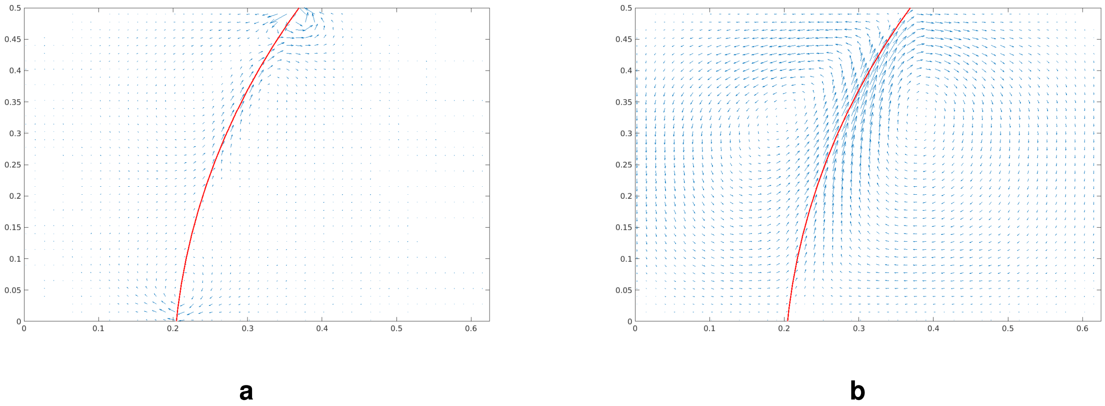

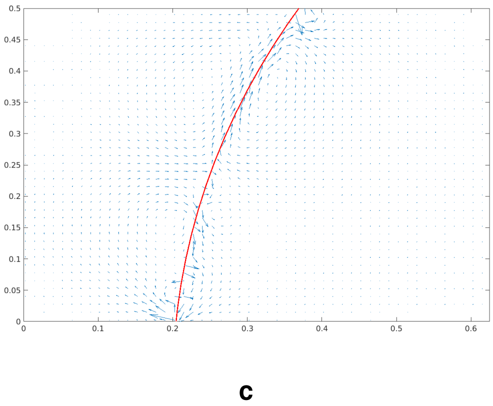

Figure 7.7: Velocity field at (a) 0.2s with $\sigma = 0.00852$ (max. velocity magnitude $\sim 10^{-3} m/s$), (b) 10s with $\sigma = 0.00852$ (max. velocity magnitude $\sim 10^{-4} m/s$) and (c) 0.2s with $\sigma = 0.0001$ (max. velocity magnitude $\sim 10^{-5} m/s$)

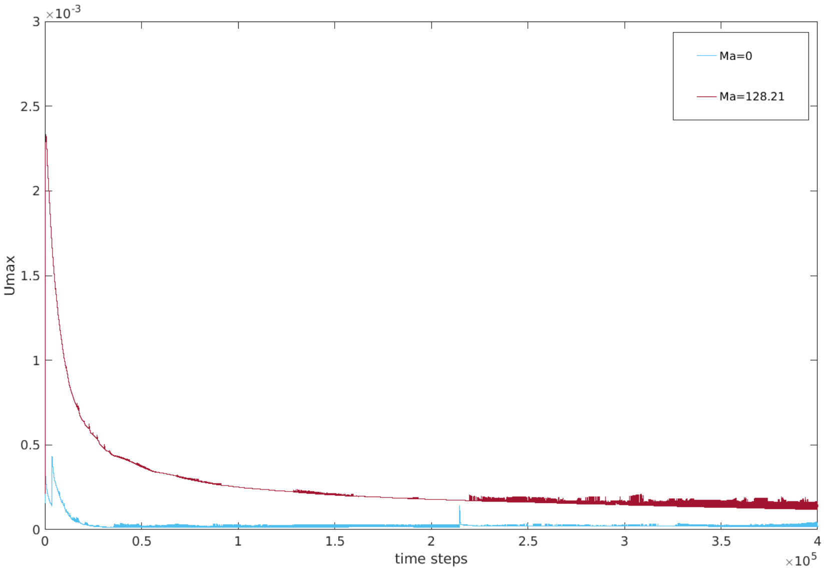

Figure 7.8: The maximum velocity with various γ with new parameters.

Effect of the area

Various areas of the fluid 2, changing by three different lengths in the x-direction, are employed to investigate the impacts on the velocity field in figure (7.9). As introduced above, in order to analyze the decreasing rate of the maximum velocity at the initial time period, the same parameters are applied as in the last section (i.e., the Schmidt number is 12.82 and the Marangoni number is 128.2).

As mentioned above, the longer time period results in a larger scale of the vortex. Therefore, the smaller area inhibits the generation of the vortex on the right side of the interface, but does not impact the magnitude of the maximum velocity. Thus, in figure (7.10), the decreasing rate of the maximum velocity is faster in the smaller area than the larger area. Moreover, the magnitudes of the maximum velocity are nearly the same. We can also observe that, due to the smaller distance between the interface and the boundary condition at the top wall, the area impacts the magnitude of the maximum velocity field when $Xl = 0.8L$. Additionally, these three maximum velocity fields converge into the parasitic currents at the end.

However, the numerical velocity field is different from that obtained from the experiments, even though the same parameters are employed. The relatively small Peclet number, resulting in diffusive dominated flows, may be the reason for the difference. Due to the limitation of the mass transfer model, it would be a challenge to simulate it with the large Peclet number. Therefore, we can only analyze the impacts of the Marangoni effect on the velocity field qualitatively.

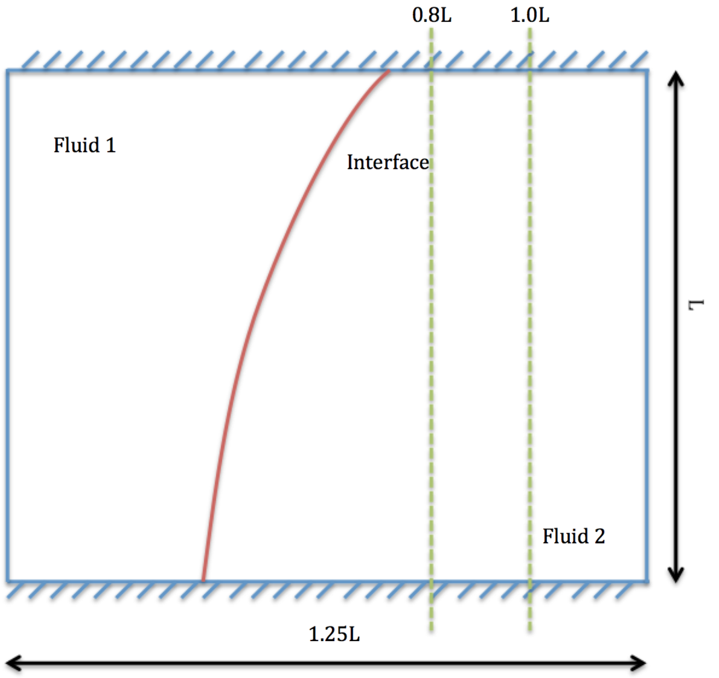

Figure 7.9: The mass transfer model with various lengths in the x-direction: 0.8L, 1.0L, 1.25L.

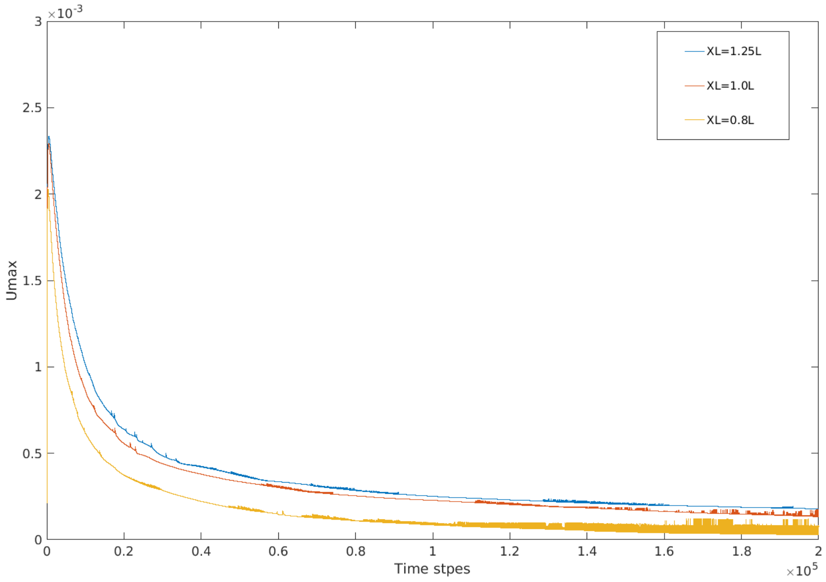

Figure 7.10: The maximum velocity field with various areas.

7.4 Mass transfer

Due to the surface tension gradient along the interface, the flow at the both sides of the interface moves tangentially to the interface, rather than the parasitic currents, which are distributed randomly along the interface. This Marangoni convection promotes the mass transfer across the interface. In this section, the mechanisms of the mass transfer impacted by the Marangoni effect are investigated.

In this case, all the density, viscosity, and mass diffusivity ratios are set to one. Moreover, the surface tension coefficient and γ are 0.05 and -0.4, respectively. The Schmidt number is 5 and the Marangoni number is 10000. Because of the small Schmidt number, the flow has a great diffusivity, so that we can observe the difference of the mass transfer coefficient easily. Figure (7.11) shows that the mass transfer coefficient k_{od} of the case with the Marangoni effect is higher than that of the case without the Marangoni effect, which is in accordance with Wang *et al.* (2008). However, it is difficult to observe the difference in the concentration field, since it only occurs at the initial time period. Therefore, the concentration field with the same parameters as in table (7.1) is shown in figures (7.12) and (7.13).

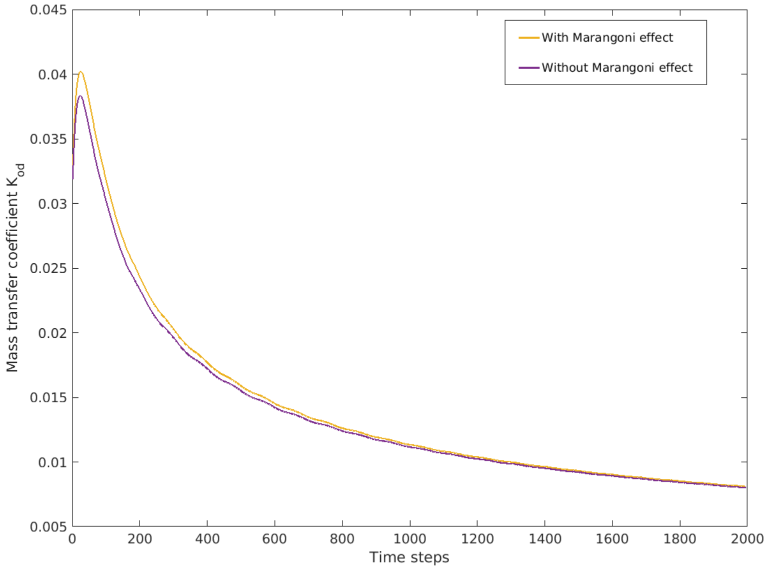

Figure 7.11: Mass transfer coefficient k_{od} with and without the Marangoni effect.

We can observe that the concentration at the top wall of the case with the Marangoni effect is slightly thicker than that of the case without the Marangoni effect. This is because when the flow moves upwards, the concentration field driven by the flow also moves along the interface and accumulates at the top wall. In such a way, the mass transfer is promoted by the Marangoni effect, especially at the top wall. Furthermore, it is important to note that, although the mass transfer depends on the convection, the interfacial mass transfer is still a purely diffusive phenomenon. However, because of the numerical limitation, the coefficient of the surface tension σ and the coefficient of the surface tension gradient γ cannot be set to large values; hence, the concentration difference is not as obvious as expected.

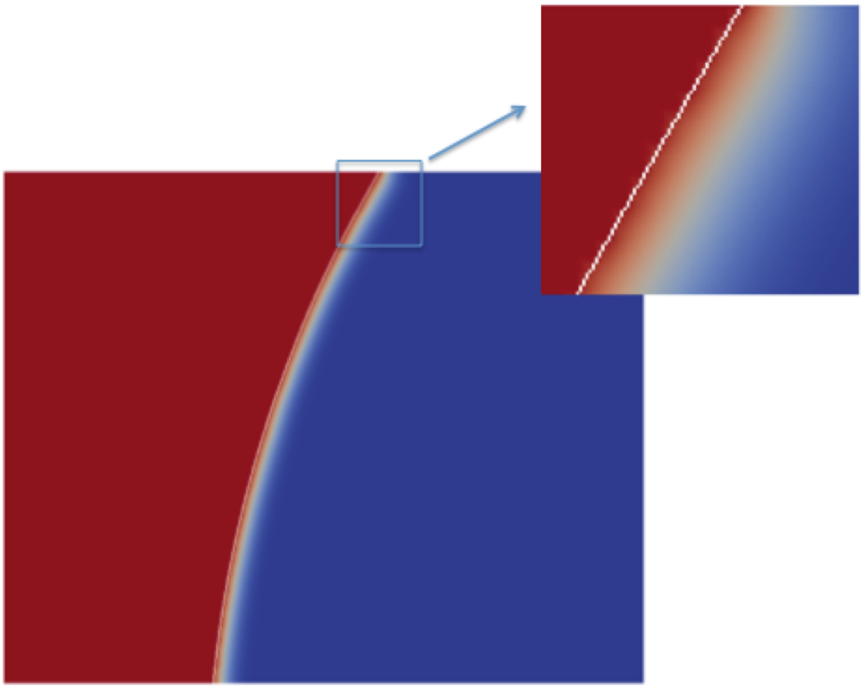

a

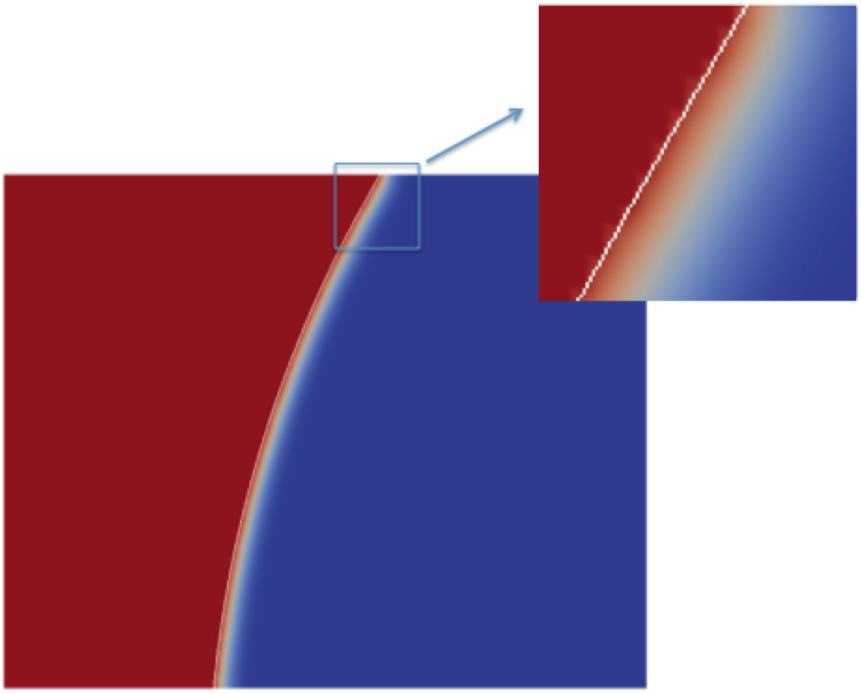

b

Figure 7.12: Concentration field with (a) and without (b) the Marangoni effect at time 100s

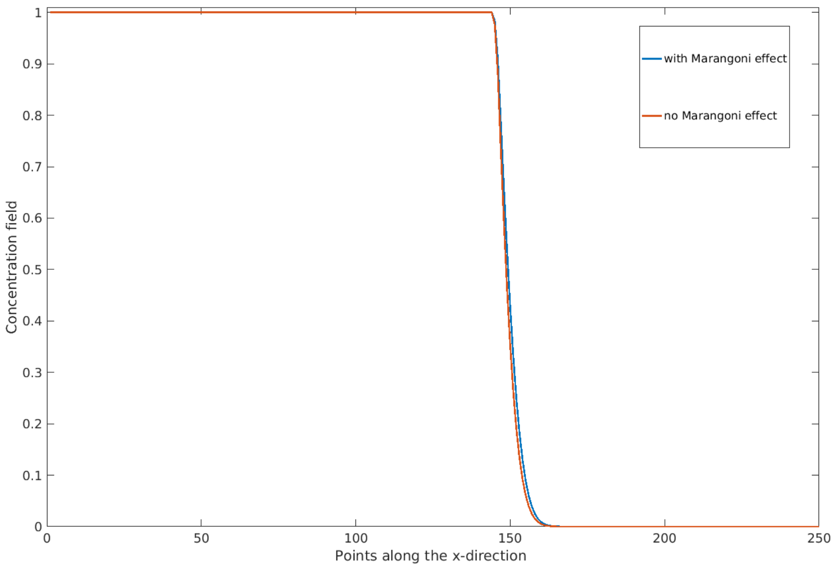

Figure 7.13: Concentration along the x-direction at $y = 0.9L$ with and without the Marangoni effect.

8 Conclusions

Multiphase mass transport on a pore-scale, including the effects of surface tension forces and Marangoni forces, has been investigated in this work. In order to simulate this phenomenon, several numerical models are implemented. The conservative level set method is employed to track the interface for multiphase flows. Due to the presence of the interface, the surface tension force needs to be simulated using the sharp surface tension force method. These two models have already been completed in a master work (Andre, 2012). Additionally, in order to quantify the wettability of a solid surface by a liquid numerically, a contact angle model based on the conservative level set method (Sato & Ničeno, 2012) is used to measure the contact angle between the surface of the liquid and the outline of the contact surface. Due to the complexity of the mass transport on the pore-scale, the Marangoni effect may arise from the concentration gradient. The Marangoni effect impacts the mass transfer process and the velocity field. Hence, the continuum surface force model is applied to model the Marangoni effect induced by the concentration gradient tangentially to the interface. Finally, a new mass transfer model based on the conservative level set method and the finite volume method, adding a source term in the scalar transportation equations, is employed to investigate the mass transport. To the best of the author's knowledge, this is a new mass transfer model based on the continuous interface method and the finite volume method. All the above numerical methods have been validated qualitatively and quantitatively.

With the help of these numerical models, two applications are conducted to analyze the mass transfer process.

A two-dimensional cavity model, neglecting the Marangoni effect, is conducted for the first application. Due to the low solubility of the Non-aqueous phase liquid, we only consider the convective mass transfer. Various flow conditions are employed to examine the mass transfer and the behavior of the interface. The results show that the Weber number is the most significant factor affecting the behavior of the interface. Thus, the Weber number can be treated as a force which protects the interface and prevents its shape changing. Moreover, since different Weber numbers are implemented for the cavity flow, various inclinations of the interface occur, resulting in different velocity manners in the cavity. The results also indicate that the time scale ratio strongly impacts the mass transfer rate. The small dimensionless time scale ratio leads to the large acceleration. Therefore, the flow obtains a strong shear layer and is able to push more mass out of the cavity. Furthermore, we found out that the starting time of the mass transfer varies because of the different accelerations.

In the second application, a two-dimensional model is applied with the Marangoni effect to investigate the mass transfer process. The external mass transfer resistance is neglected. The results show that, due to the Marangoni effect, a circulation occurs tangentially to the interface, rather than the parasitic currents in the case without the Marangoni effect. This pattern of the velocity field enhances the mixture process, such that the mass transfer rate is larger for the Marangoni effect than without considering the Marangoni effect. The concentration field also verifies this conclusion, that the concentration at the top wall is more than that of the case without the Marangoni effect. Furthermore, the maximum velocity field influenced by various conditions is presented as well.

A number of extensions to this dissertation are addressed in the following directions: the simulation of the conservative level set method in complex geometries would be an interesting extension to this work. This requires the combination of the immersed boundary method and the conservative level set method. Another extension would be the simulation with a large Peclet number. So far, only diffusive dominated flows have been simulated in the second application based on the new mass transfer model. This may be a reason that the maximum velocity field differs from the experimental results. Moreover, the time step limitation, which is due to the numerical stable conditions, prevents simulating with longer time. Therefore, the numerical model needs to be further refined and improved. The three-dimensional simulation would also be a possible extension. As the Marangoni effect and the contact angle are three-dimensional phenomena in nature, it would be interesting to extend these models to three dimensions.

Bibliography

Abouhamza, A. & Pierre, R. 2003 A neutral stability curve for incompressible flows in a rectangular driven cavity. *Mathematical and Computer Modelling* **38** (141-157).

Aboulhasanzadeh, B., Thomas, S., Taeibi-Rahni, M. & Tryggvason, G. 2012 Multiscale computations of mass transfer from buoyant bubbles. *Chemical Engineering Science* **75** (456-467).

Afkhami, S. & Bussmann, M. 2009 Height functions for applying contact angles to 3d vof simulations. *Int. J. Numer. Methods Fluids* **61** (827-847).

Allegrini, Jonas, Dorera, Viktor & Carmeliet, Jan 2014 Buoyant flows in street canyons: Validation of cfd simulations with wind tunnel measurements. *Building and Environment* **72** (63-74).

Andre, M. 2012 Conservative level set method for direct numerical simulation of two-phase flows. Master's thesis, Technische Universität München.

Ashcroft, G. & Zhang, X. 2005 Vortical structures over rectangular cavities at low speed. *Phys. Fluids* **17** (015104).

Augustijn, D. C. M., Jessup, R. E., Rao, P. S. C. & Wood, A. L. 1994 Remediation of contaminated soils by solvent flushing. *J. Environ. Eng.* **120** (42-57).

Badalassi, V. E., Ceniceros, H. D. & Banerjee, S. 2003 Computation of multiphase systems with phase field models. *J. Comput. Phys.* **190** (371-397).

Bahloul, A., Delahaye, R., Vasseur, P. & Robillard, L. 2003 Effect of surface tension on convection in a binary fluid layer under a zero gravity environment. *Int J Heat Mass Transfer* **46(10)** (1759-1771).

Bassano, E. 2003 Numerical simulation of thermo-solutal-capillary migration of a dissolving drop in a cavity. *Int J Num Meth Fluids* **41(7)** (765-788).

Bergeron, A., Henry, D. & Benhadid, H. 1994 Marangoni-bénard instability in microgravity conditions with soret effect. *Int J Heat Mass Transfer* **37(11)** (1545-1562).

Bergeron, A., Henry, D., Benhadid, H. & Tuckerman, L. S. 1998 Marangoni convection in binary mixture with soret effect. *J Fluid Mech.* **375** (143-177).

Borghi, R. & Anselmet, F. 2014 *Turbulent multiphase flows with heat and mass transfer.*. WILEY press.

Brackbill, J. U., Kothe, D. B. & Zemach, C. 1992 A continuum method for modeling surface tension. *J. Comput. Phys.* **100** (335-354).

BRANDES, D. & FARLEY, K. J. 1993 Importance of phase-behavior on the removal of residual dnapls from porous media by alcohol flooding. *Water Environ. Res.* **65** (869-878).

BROWN, N.M. & LAI, F.C. 2005 Correlations for combined heat and mass transfer from an open cavity in a horizontal channel. *International Communications in Heat and Mass Transfer* **32** (1000-1008).

BUSSMANN, M., CHANDRA, S. & MOSTAGHIMI, J. 2000 Modeling the splash of a droplet impacting a solid surface. *Phys. Fluids* **12** (3121-3132).

BUSSMANN, M., MOSTAGHIMI, J. & CHANDRA, S. 1999 On a three-dimensional volume tracking model of droplet impact. *Phys. Fluids* **11** (1406-1417).

CASSIE, A. B. D. & BAXTER, S. 1944 Wettability of porous surfaces. *Trans. Faraday Soc.* **40** (546-551).

CHANG, H. N., RYU, H. W., PARK, D.H ., YONG, S. P. & PARK, J. K. 1987 Effect of external laminar channel flow on mass transfer in a cavity. *Int. J. Heat Mass Transfer* **30 (10)** (2137-2149).

CHANG, Y. C., HOU, T. Y., MERRIMAN, B. & OSHER, S. 1996 A level set formulation of eulerian interface capturing methods for incompressible fluid flows. *J. Comput. Phys.* **124** (449-464).

CHARWAT, A. F., FOOS, J. N., DEWEY, F. C. & HITZ, J. A. 1961 An investigation of separated flows. part 1. the pressure field. *J. Aero. Sci.* **28(6)** (457-70).

CHEN, H., ZHONG, Q., WANG, X. K. & LI, D. X. 2014 Reynolds number dependence of flow past a shallow open cavity. *SCIENCE CHINA: Technological Sciences* **57 (11)** (2161-2171).

CHENG, P., BESTEHORN, M. & FIROOZABADI, A. 2012 Effect of permeability anisotropy on buoyancy-driven flow for co2 sequestration in saline aquifers. *Water Resourc. Res.* **48** (W09539).

CHIBOWSKI, E. & TERPILOWSKI, K. 2008 Surface free energy of sulfur-revisited i. yellow and orange samples solidified against glass surface. *Journal of Colloid and Interface Science* **319(2)** (505-513).

CLIFT, R., GRACE, J. R. & WEBER, M. E. 1978 *Bubbles, drops, and particles.*. Academic press.

COLELLA, P., GRAVES, D.T., MODIANO, D., PUCKETT, E.G. & SASSMAN, M. 1999 An embedded boundary/volume of fluid method for free surface flows in irregular geometries. In *Proceedings of the 3rd ASME/JSME Joint Fluids Engineering Conference, number FEDSM99-7108, San Francisco, CA.*

COX, R.G. 1986 The dynamics of the spreading of liquids on a solid surface. *Part 1, J. Fluid Mech.* **168** (169-194).

CROOK, S. D., LAU, T. C. W. & KELS, R. M. 2013 Three-dimensional flow within shallow, narrow cavities. *J. Fluid Mech.* **735** (587-612).

CUMMINS, S.J., FRANCOIS, M.M. & KOTHE, D.B. 2005 Estimating curvature from volume fractions. *J. Comput. Struct.* **83 (6-7)** (425-434).

DARHUBER, A. A. & TROIAN, S. M. 2005 Principles of microfluidic actuation by modulation of surface stresses. *Annu. Rev. Fluid Mech.* **37** (425-455).

DAVIDSON, M. R. & RUDMAN, M. 2002 Volume-of-fluid calculation of heat or mass transfer across deforming interfaces in two-fluid flow. *Numer. Heat Transfer, Part B: Fundam.* **41** (291-308).

DAVIS, S.H. 1987 Thermo-capillary instabilities. *Annu. Rev. Fluid Mech.* **19** (403-435).

DESJARDINS, O., MOUREAU, V. & PITSCH, H. 2008 An accurate conservative level set/ghost fluid method for simulating turbulent atomization. *J. Comput. Phys.* **227** (8395-8416).

EBERHARDT, C. & GRATHWOHL, P. 2002 Time scales of organic contaminant dissolution from complex source zones: coal tar pools vs. blobs. *J. Cont. Hydrol* **59** (45-66).

ERTURK, E., CORKE, T. C. & GOKCOL, C. 2005 Numerical solutions of 2-d steady incompressible driven cavity flow at high reynolds numbers. *International Journal for Numerical Methods in Fluids* **48** (747-774).

FEDKIW, RONALD P., ASLAM, TARIQ, MERRIMAN, BARRY & OSHER, STANLEY 1999 A non-oscillatory eulerian approach to interfaces in multimaterial flows (the ghost fluid method). *J. Comput. Phys.* **152** (457-492).

FETTER, C.W. 1993 *Contaminant Hydrogeology*. Macmillan, New York, NY (458).

FRANCOIS, M.M., CUMMINS, S.J., DENDY, E.D., KOTHE, D.B., SICILIAN, J.M. & WILLIAMS, M.W. 2006 A balanced-force algorithm for continuous and sharp interfacial surface tension models within a volume tracking framework. *J. Comput. Phys.* **213** (141-173).

GALAZKA, Z. & WILKE, H. 2000 Influence of marangoni convection on the flow pattern in the melt during growth of $y_3al_5o_12$ single crystals by the czochralski method. *J Crystal Growth* **216(1-4)** (389-398).

GANGULI, A. A. & KENIG, E. Y. 2011a A cfd-based approach to the interfacial mass transfer at free gas-liquid interfaces. *Chem. Eng. Sci.* **66** (3301-3308).

GANGULI, A. A. & KENIG, E. Y. 2011b Prediction of interfacial mass transfer in liquid-liquid systems with moving interfaces. *Chem. Eng. Trans.* **24** (1357-1362).

GAO, D., MORLEY, N. B. & DHIR, V. 2003 Numerical simulation of wavy falling film flow using vof method. *J. Comput. Phys.* **192** (624-642).

GUEYFFIER, D., LI, JIE, NADIM, ALI, SCARDOVELLI, R. & ZALESKI, S. 1999 Volume-of-fluid interface tracking with smoothed surface stress methods for three-dimensional flows. *J. Comput. Phys.* **152** (423-456).

GUPTA, R., FLETCHER, D. F. & HAYNES, B. S. 2010 Cfd modelling of flow and heat transfer in the taylor flow regime. *Chem. Eng. Sci.* **65** (2094-2107).

Hayashi, K. & Tomiyama, A. 2011 Interface tracking simulation of mass transfer from a dissolving bubble. *J. Comput. Multiphase Flows* **3** (247-262).

Herrmann, M. 2008 A balanced force refined level set grid method for two-phase flows on unstructured flow solver grids. *J. Comput. Phys.* **227** (2674-2706).

Himeno, T. & Watanabe, T. 2005 Numerical analysis for propellant management in rocket tanks. *J. Propulsion Power* **21** (76-86).

Hirt, C. W. & Nichols, B. D. 1981 Volume of fluid (vof) method for the dynamics of free boundaries. *J. Comput. Phys.* **39** (201-225).

Hoffman, R.L. 1975 A study of the advancing interface. *J. Colloid Interface Sci.* **50** (228-241).

Juric, D. & Tryggvason, G. 1998 Computations of boiling flows. *Int. J. Multiphase Flow* **24** (387-410).

Kang, M., Fedkiw, R. P. & Liu, Xudong 2000 A boundary condition capturing method for multiphase incompressible flow. *J. Scientific Computing* **15** (323-360).

Kawaji, M., Gamache, O., Hwang, D. H., Ichikawa, N., Viola, J. P. & Sygusch, J. 2003 Investigation of marangoni and natural convection during protein crystal growth. *J Crystal Growth* **258(3-4)** (420-430).

Khanafer, Khalil, Vafai, Kambiz & Lightstone, Marilyn 2002 Mixed convection heat transfer in two-dimensional open-ended enclosures. *International Journal of Heat and Mass Transfer* **45** (5171-5190).

Khosravi, M., Bahramian, A., Emadi, M., Rostami, B. & Roayaie, E. 2014 Effect of marangoni flow on recovery of bypassed oil during co2 injection. *J. Petrol. Sci. Eng.* **114** (91-98).

Kim, Junseok 2005 A continuous surface tension force formulation for diffuse-interface models. *J. Comput. Phys.* **204** (784-804).

Kim, J., Choi, C. K. & Kang, Y. T. 2004 Instability analysis of marangoni convection for absorption process accompanied by heat transfer. *Int J Heat Mass Transfer* **47(10-11)** (2395-2402).

Kirkpatrick, M. P., Armfield, S. W. & Williamson, N. 2012 Shear driven purging of negatively buoyant fluid from trapezoidal depressions and cavities. *Physics of Fluids* **24** (161-164).

Kobayashi, M., Tsukuda, T. & Hozawa, M. 1997 Effect of internal radiative heat transfer on the convection in cz oxide melt. *J Crystal Growth* **180(1)** (157-166).

Landau, L. D. & Lifshitz, E. M. 1987 *Fluid Mechanics, 2nd, vol. 6*. Pergamon press, Oxford.

Leong, J.C., Brown, N.M. & Lai, F.C. 2005 Mixed convection from an open cavity in a horizontal channel. *International Communications in Heat and Mass Transfer* **32** (583-592).

Levich, V. G. & Krylov, V. S. 1969 Surface-tension-driven phenomena. *Annu. Rev. Fluid Mech.* **1** (293-316).

Liffman, K. 1996 Comments on a collocation spectral solver for the helmholtz equation. *Journal of Computational Physics.* **128** (254-258).

Liu, C. H., Barth, M. C. & Leung, D. Y. C. 2004 Large-eddy simulation of flow and pollutant transport in street canyons of different building-height-to-street-width ratios. *Journal of Applied Meteorology* **43** (1410-1424).

Liu, W., Yuan, L. & Shu, C. W. 2011 A conservative modification to the ghost fluid method for compressible multiphase flows. *Communications in Computational Physics* **10(4)** (785-806).

Liu, X.-D., Fedkiw, R.P. & Kang, M. 2000 A boundary condition capturing method for poisson's equation on irregular domains. *J. Comput. Phys.* **160** (151-178).

Mackay, D. M. & Cherry, J. A. 1989 Groundwater contamination: pump-and-treat remediation. *Environ. Sci. Technol.* **23** (630-636).

Mammoli, A. A. & Brebbia, C. A. 2005 *Computational Methods In Multiphase Flow III.*. WIT press.

Manhart, M. 2004 A zonal grid algorithm for dns of turbulent boundary layer. *Comput. Fluids* **33(3)** (435-461).

Manhart, M. & Friedrich, R. 2002 Dns of a turbulent boundary layer with separation. *Int. J. Heat Fluid Flow* **23(5)** (572-581).

Mao, Z. S. & Chen, J. Y. 2004 Numerical simulation of the marangoni effect on mass transfer to single slowly moving drops in the liquid-liquid system. *Chem Eng Sci* **59(8-9)** (1815-1828).

Mao, Z. S., Li, T. & Chen, J. 2001 Numerical simulation of steady and transient mass transfer to a single drop dominated by external resistance. *Int. J. Heat Mass Transfer* **44** (1235-1247).

Marchandise, E., Geuzaine, P., Chevaugeon, N. & Remacle, J.-F. 2007 A stabilizing finite element method using a discontinuous level set approach for the computation of bubble dynamics. *J. Comput. Phys.* **225** (949-974).

Marmur, A. 2009 Solid-surface characterization by wetting. *Annual Review of Materials Research* **39** (473-489).

Newman, A. B. 1931 The drying of porous solids: diffusion and surface emission equations. *Transactions AlChE* **27** (203-220).

Occhialini, J. M. & Higdon, J. J. L. 1992 Convective mass transport from rectangular cavities in viscous flow. *J. Electronchem. Soc.* **139 (10)** (2845).

Okano, Y., Fukuda, T., Hirata, A., Takano, N., Tsukuda, T., Hozawa, M. & Imaishi, N. 1991 Numerical study on czochralski growth of oxide single crystals. *J Crystal Growth* **109(1-4)** (94-98).

Olsson, E. & Kreiss, G. 2005 A conservative level set method for two phase flow. *J. Comput. Phys.* **210** (225-246).

Olsson, E., Kreiss, G. & Zahedi, S. 2007 A conservative level set method for two phase flow ii. *J. Comput. Phys.* **225** (785-807).

Ortiz, E., Kraatz, M. & Luthy, R. G. 1999 Organic phase resistance to dissolution of poly-cyclic aromatic hydrocarbon compounds. *Environ. Sci. Technol.* **33** (235-242).

Osher, S. & Fedkiw, R. 2002 Level set methods and dynamic implicit surfaces. *Applied Mathematical Sciences* **153**, springer-Verlag, New York.

Osher, S. & Sethian, J. A. 1988 Fronts propagating with curvature-dependent speed: Algorithms based on hamilton-jacobi formulations. *J. Comput. Phys.* **79** (12?49).

Pennell, K. D., Abriola, L. M. & Weber, W. J. Jr. 1993 Surfactant-enhanced solubilization of residual dodecane in soil columns: 1. experimental investigation. *Environ. Sci. Technol.* **27** (2332-2340).

Petera, J. & Weatherley, L. R. 2001 Modelling of mass transfer from falling drops. *Chemical Engineering Science* **56** (4929-4947).

Popinet, S. & Zaleski, S. 1999 A front-tracking algorithm for accurate representation of surface tension. *Int. J. Numer. Meth. Fluids* **30 (6)** (775-793).

Prosperetti, A. 1981 Motion of two superposed viscous fluids. *Phys. Fluids* **24(7)** (1217-1223).

Ramachandran, P. A. 2018 *Mass transfer processes: modeling, computations, and design.* Prentice Hall.

Renardy, Y. & Renardy, M. 2002 Prost: A parabolic reconstruction of surface tension for the volume-of-fluid method. *J. Comput. Phys.* **183** (400-421).

Rider, W. J. & Kothe, D. B. 1998 Reconstructing volume tracking. *J. Comput. Phys.* **141** (112-152).

Sarohia, V. 1977 Experimental investigation of oscillations in flows over shallow cavities. *AIAA J* **15** (984-991).

Sato, Y. & Ničeno, B. 2012 A new contact line treatment for a conservative level set method. *J. Comput. Phys.* **231** (3887-3895).

Schwertfirm, F., Mathew, J. & Manhart, M. 2008 Improving spatial resolution characteristics of finite difference and finite volume schemes by approximate deconvolution preprocessing. *Comput. Fluids* **37 (9)** (1092-1102).

Sethian, J. A. 1999 *Level Set Methods and Fast Marching Methods, second ed.*. Cambridge University Press, Cambridge, UK.

Shaikha, J., Bhardwaj, R & Sharma, A. 2015 A ghost fluid method based sharp interface level set method for evaporating droplet. *Procedia IUTAM* **15** (124-131).

SIRIGNANO, W.A. 1999 *Fluid dynamics and transport of droplets and sprays.*. Cambridge University press.

SUSSMAN, M. 2001 An adaptive mesh algorithm for free surface flows in general geometries. In *Adaptive Method of Lines, Chapman and Hall/CRC* (ed. A. Vande Wouwer, Ph. Saucez & W.E. Schiesser).

SUSSMAN, M. 2005 A parallelized adaptive algorithm for multiphase flows in general geometries. *Computers and Structures* **83** (435-444).

SUSSMAN, M. & FATEMI, E. 1999 An efficient, interface-preserving level set redistancing algorithm and its application to interfacial incompressible fluid flow. *SIAM J. Sci. Comput.* **20 (4)** (1165-1191).

SUSSMAN, M., FATEMI, E., SMEREKA, P. & OSHER, S. 1998 An improved level set method for incompressible two-phase flows. *Comput. Fluids* **27 (5-6)** (663-680).

SUSSMAN, M., SMEREKA, P. & OSHER, S. 1994 A level set approach for computing solutions to incompressible two-phase flow. *J. Comput. Phys.* **114** (146-159).

TADMOR, R. 2004 Line energy and the relation between advancing, receding, and young contact angles. *Langmuir* **20(18)** (7659-7664).

TANG, HAO, WROBEL, L. C. & FAN, Z. 2004 Tracking of immiscible interfaces in multiple-material mixing processes. *Comp. Mater. Sci.* **29** (103-118).

TANGUY, S., ME?NARD, T & BERLEMONT, A. 2007 A level set method for vaporizing two-phase flows. *Journal of Computational Physics* **221** (837-853).

TOMAR, G., BISWAS, G., SHARMA, A. & AGRAWAL, A. 2005 Numerical simulation of bubble growth in film boiling using a coupled level-set and volume-of-fluid method. *Phys. Fluid* **14** (112103).

TORNBERG, A.-K. & ENGQUIST, B. 2000 A finite element based level set method for multiphase flow applications. *Comput. Visualiz. Sci.* **3** (93-101).

TRYGGVASON, G., SCARDOVELLI, R. & ZALESKI, S. 2011 *Direct Numerical Simulations of Gas-Liquid Multiphase Flows.*. Cambridge University Press, Cambridge, UK.

UNVERDI, O. S. & TRYGGVASON, G. 1992*a* A front-tracking method for viscous, incompressible, multi-fluid flows. *Journal of Computational Physics* **100** (25-37).

UNVERDI, S. O. & TRYGGVASON, G. 1992*b* A front-tracking method for viscous, incompressible, multi-fluid flows. *J. Comput. Phys.* **100** (25-37).

WANG, JIANFENG, YANG, CHAO & MAO, ZAISHA 2008 Numerical simulation of marangoni effects of single drops induced by interphase mass transfer in liquid-liquid extraction systems by the level set method. *Science in China Series B: Chemistry* **51** (684-694).

WEHRER, M., RENNERT, T., MANSFELDT, T. & TOTSCHE, K. U. 2011 Contaminants at former manufactured gas plants: sources, properties, and processes. *Crit. Rev. Environ. Sci. Technol.* **41** (1883-1969).

Welch, S. & Wilson, J. 2000 A volume of fluid based method for fluid flows with phase change. *J. Comput. Phys.* **160** (662).

Wenzel, R. N. 1936 Resistance of solid surfaces to wetting by water. *Ind. Eng. Chem.* **28(8)** (988-994).

White, H.E. 1948 *Modern College Physics.*. van Nostrand.

Yang, J. & Stern, F. 2009 Sharp interface immersed-boundary/level-set method for wave-body interactions. *J. Comput. Phys.* **228** (6590-6616).

Yokoi, K. 2011 Numerical studies of droplet splashing on a dry surface: triggering a splash with the dynamic contact angle. *Soft Matter* **7** (5120-5123).

Zahedi, S., Gustavsson, K. & Kreiss, G. 2009 A conservative level set method for contact line dynamics. *J. Comput. Phys.* **228** (6361-6375).